Polymorphism of sulfur: Structural and Dynamical Aspects

Laura Crapanzano

Thèse

présentée par

Laura Crapanzano

Pour obtenir le titre de

Docteur de l'Université Joseph Fourier - Grenoble I

Polymorphism of Sulfur: Structural and Dynamical Aspects

Date de Soutenance: 20 Juin 2005

Composition du jury:

Dr. Joel Chevrier	President du jury
Dr. Paul Loubeyre	Rapporteur
Prof. Ralf Steudel	Rapporteur
Prof. Daniele Fioretto	Examinateur
Prof. Alfredo Segura	Examinateur
Prof. Robert Bellissent	Directeur de thèse
Dr. Giulio Monaco	Co-Directeur de thèse

Co-Directeurs de thèse:	Dr. Wilson Crichton
	Dr. Mohamed Mezouar

Thèse préparée au sein du laboratoire

European Synchrotron Radiation Facility

BP 220 - 38043 Grenoble Cedex - France

Dedicated to my parents

Abstract

This thesis deals with an investigation of polymorphism in both solid and liquid state of sulphur. Emphasis has been put on the polymer transition of liquid sulphur.

From a short introduction to polymorphism, sulphur appears as a convenient system for these studies. The state of the art of the P T diagram of sulphur is discussed. Then the manuscript describes the high pressures devices and introduces the ESRF used techniques in order to get either structural or dynamical *in situ* information; namely X ray scattering, Raman scattering and inelastic X ray scattering.

The following part is devoted to the structural results obtained on several sulphur allotropes. Owing to the possibility of in situ measurements with high flux and by using together X-ray and Raman scattering, the structure of equilibrium phases has been determined. Then a new p,T phase diagram of sulphur has been obtained.

The last part concerns the dynamical results obtained in the temperature range of the polymerization transition. Above the transition sulphur behaves as a conventional molecular liquid made of S8 units. At higher temperature it still exhibits S_8 molecular motion. However a lower frequency mode shows up. It corresponds to the dynamics of cross linked chain fragments.

Résumé

Cette thèse est une contribution à l'étude du polymorphisme du soufre à l'état solide et à l'état liquide avec, en particulier un examen des transitions liquide-liquide.

Une introduction sur le polymorphisme dans les matériaux simples conduit à faire le choix d'étudier le soufre et on présente l'état des connaissances actuelles sur le diagramme P T du soufre. Puis on décrit les dispositifs haute pression; enclume diamant et presse à grand volume, mis en place à l'ESRF pour réaliser des études structurales ou dynamiques in situ, ainsi que les techniques d'étude de la structure et de la dynamique ; diffraction X, diffusion Raman, diffusion X inélastique utilisés pour ce travail.

La partie suivante expose les résultats obtenus sur la structure des différents allotropes du soufre. Grce à la possibilité de mesures in situ avec un flux intense et à l'utilisation conjointe de la diffraction X et de la diffusion Raman il a été possible de caractériser la structure de phases à l'équilibre et de construire d'un nouveau diagramme de phases du soufre en pression et température.

La dernière partie concerne les résultats obtenus sur la dynamique du soufre liquide autour de la transition de polymérisation. On caractérise ainsi, aux basses températures, un liquide moléculaire classique dont la dynamique est celle des molécules S_8. Aux plus hautes températures une solution de polymères présente encore le mode à haute fréquence correspondant aux molécules S8 mais aussi un autre, à basse fréquence, qui correspond à des fragments de chaînes interconnectes.

List of abbreviations

ADX	Angle Dispersive X-Ray
BM	Bending Magnet
CCD	Charge Coupled Device
CN	Coordination Number
DAC	Diamond Anvil Cell
DHO	Damped Harmonic Oscillator
DTA	Differential Thermal Analysis
EDX	Energy Dispersive X-Ray
EoS	Equation of State
ESRF	European Synchrotron Radiation Facility
FWHM	Full Width at Half Maximum
FP-LMTO	Full Potential Linear Muffin-Tin Orbital
HP	High-Pressure
HT	High-Temperature
ID	Insertion Device
IXS	Inelastic X-Ray Scattering
LINAC	Linear Accelerator
LVP	Large Volume Press
MCC	Multi Channel Collimator
NIST	National Institute of Standards and Technology
P-E	Paris-Edinburgh
PMMA	Poly-Methyl-MethAcrylate
PXRD	Powder X-Ray Diffraction
RT	Room Temperature
SD	Sintered Diamonds
SLWD	Super Long Working Distance
XRD	X-Ray Diffraction

Contents

Introduction

Polymorphism, the existence of different structural forms of the same substance has been and still is the subject of numerous studies. This is principally due to the fact that each polymorphic form can have characteristic physical properties. For that reason the study and the application of polymorphism have become fundamental in several industrial sectors, such as the pharmaceutic industry.

Other than its practical applications, the study of polymorphism is important also from a theoretical point of view. In solid systems, the study of polymorphic forms is a key to understanding structure-property relationships. In many cases, simple elemental systems have revealed rich structural behavior upon compression. In particular, similarity is often seen when comparing high pressure structural sequences of elements in the same group of the periodic table. However, the formulation of a general theory requires a complete set of information on the phase diagrams of simple systems and often this information is not available. For that reason, extensive and systematic *in situ* studies of phase diagrams are required.

In the liquid state, the idea of different structural forms is supported by several experimental observations, but the theory is still under construction. On one side, in fact, the concept of solid polymorphism is well-defined: different polymorphs have different crystalline structures, which can be clearly seen by their diffraction patterns. On the other side, the lack of periodicity in the liquid state makes it more difficult to introduce the concepts of *liquid form* or *liquid phase*.

An important result in the physics of simple liquids is represented by the recent observation of a first order phase transition in liquid phosphorus by Katayama *et al.* [1]. At 1000^oC and 1 GPa, a significant change in the diffraction pattern of liquid phosphorus is observed over a pressure interval of less than 0.02 GPa. This work has been the driving force for many theoretical and experimental studies. At present, the true nature of this transition in phosphorus is not fully understood [2], because of the lack of data in the phase diagram of phosphorus. However, the search for new examples of liquid-liquid transitions in elemental systems has continued.

The structure of a liquid can be described as a distribution of preferred local arrangements whose proportions and nature change with varying external thermodynamic conditions. These also determine changes in the physical properties of the liquid. Structural studies of covalent and molecular systems have revealed a similarity between the local liquid structure and the short range order and coordination environment of the solid phases. Similar changes of the physical properties are also often observed in the solid and the liquid state upon compression, this is the case for example of many elements metallization. These results suggest that in many cases the polymorphism of the liquid can be correlated to that of the solid.

The growing interest surrounding study of the liquid domain and the possibility of correlation between solid and liquid polymorphism has stimulated this thesis. Sulfur has been chosen because it links the apparent simplicity of an elemental system to a very complex behavior both in the liquid and the solid phase. Naturally, sulfur normally occurs as yellow orthorhombic crystals; however, a large number of allotropic forms are known (the largest number of all the elements). These structures are based principally on cyclic molecules or polymeric chains. Most of the known allotropes are metastable forms that have been synthesized chemically. The phase diagram contains information on the thermodynamically stable forms, but, in the case of sulfur the available literature data are confusing. The reason for this are manifold, with structural information often coming from quench recovery products and the high reactivity of sulfur with metals (normally used as confinement materials) limiting the thermodynamic range of investigation. Consequently, the reported phase diagrams of sulfur do, in most cases, refer to metastable phases and some stability domains, that have been individuated through variation of a specific physical property, do not necessarily correspond to a true structural phase transition. For that reasons a complete *in situ* structural investigation of the phase diagram of sulfur has been considered indispensable.

Besides the study of the solid phases, sulfur has been considered a good candidate for observing transitions in the liquid state. The existence of molecular and polymeric forms in the liquid is known and also provides a structural link with liquid phosphorus. Particular changes in the physical properties of the liquid have been observed at definite thermodynamic conditions. The most studied of these changes, taking place at room pressure, has been associated to a structural transition in the liquid, known as λ-transition. This transition is related to the formation of a fraction of polymeric chains in the liquid and represents a first link between the polymorphism of sulfur in the solid and the liquid state. In addition to the λ-transition, several electrical anomalies have been detected in the liquid at high pressure [3–5].

The basic aims of this thesis have been to define the solid phase diagram of sulfur (in a pressure range below 15 GPa) and to study the liquid domain over a pressure range as wide as possible. The possibility of exploring a large pressure-temperature domain with the different high pressure devices available at the beamline ID30 (now ID27) has allowed us to perform numerous *in situ* X-ray diffraction experiments. Additional high pressure Raman experiments have been also performed at the Université Joseph Fourier. Measurements at beamline ID16 have allowed us to study the dynamical properties of the liquid at room pressure using inelastic X-ray scattering. Different techniques have been used in order to cross-link different information and draw as complete as possible a picture on the behavior of molecules and polymeric chains. This is particularly important in the case of the liquid, for which the information that we have from diffraction studies is less precise due to the lack of long range order. Diffraction data on liquids allow us to follow local structural evolution and give indications on the length-scale that these changes are taking place. However, detailed information on local liquid structure requires the synthesis of diffraction data with results of other techniques. That will allow us to explore the dynamical, molecular and macroscopic properties of the liquid. In each step of this study, we have also appreciated the importance of correlating our results to previous literature: in more than one case, this comparison has demonstrated to be fundamental.

The principal objectives of this thesis work are:

The clarification of the differences among literature results: Diffraction and Raman results give a different picture of the high pressure solid phases of sulfur. The relation between the structures observed by Raman spectroscopy and the results of recent diffraction experiments at high pressure has to be established. We have to explain why these structures are observed by the two techniques but in different thermodynamic conditions. In addition to that, we have to explain why the molecular S_6, solid observed by Raman at room temperature, has not been observed by diffraction: is S_6 photoinduced? The clarification of these issues will be provide a link between the structural sequences obtained by Raman spectroscopy and by diffraction.

The reconstruction of the phase diagram of solid sulfur: The stable phases of sulfur can be individuated by *in situ* diffraction measurements. Reconstruction of the phase diagram includes measurement of the melting curve, the characterization of the stable phases and their stability regimes. The stability of each phase can be evaluated through the reversibility of its formation and the coexistence at a transition

line. A detailed mapping gives an idea on the stability regimes of each phase and on the eventual presence of kinetic barriers.

The structural study of the liquid under pressure: Diffraction can be used to follow the structural changes induced in the liquid through application of pressure and temperature. Again, a parallel diffraction-Raman study has been used to test the hypothesis that pressure influences the equilibrium polymerization of the liquid. The Raman data on the solid can be used as starting point for the recognition of the molecular and polymeric species in the liquid.

The study of the dynamics of liquid sulfur around the λ-transition: The viscosity jump of liquid sulfur associated to the λ-transition could be correlated to new dynamical processes that involve both molecules and chains. The physical origin of these motions can be studied by investigating the relaxation processes present in the liquid before and after the λ-transition. With this purpose, high frequency data, collected using inelastic X-ray scattering, can be compared to low frequency literature data, in order to shed light on the nature of the dynamical processes active in the liquid on different timescales.

The body of the manuscript is subdivided in three main sections, with a conclusion in. Each section is composed of two chapters:

General background: The first chapter gives a general introduction to the concept of polymorphism in the solid and the liquid state and its thermodynamical and physical basis. The second chapter gives a brief presentation of the sulfur allotropes that have a role in the construction of our phase diagram and a brief review on the literature on liquid sulfur.

Experimental methods: In the third chapter we describe the pressure devices used for the pressure-temperature generation and their calibration methods. The fourth chapter is an introduction to the synchrotron radiation, the beamlines and the principles of the techniques used for this experimental work.

Results: Chapters 5 and 6 contain our experimental results. In chapter 5, we introduce progressively the results obtained by diffraction in our mapping of the phase diagram. The literature data are compared to our Raman and diffraction data on the solid. Diffraction and Raman spectroscopy data on the liquid are also presented to establish the role of pressure in the polymerization process. The phase diagram of sulfur is

presented as a synthesis of the structural study.

Chapter 6 contains the dynamical study conducted on liquid sulfur around the λ-transition using inelastic X-ray scattering. A dynamical model is proposed and discussed.

Part I

General background

Résumé du chapitre 1

Le polymorphisme suscite un intérêt tout particulier pour ses applications industrielles, en particulier dans le domaine pharmaceutique. Ceci s'explique par le fait que des formes structurales distinctes de la même substance présentent des propriétés physiques totalement différentes. La possibilité d'élucider la relation entre la structure et les propriétés est à l'origine de nombreuses études sur les systèmes simples présentant une variété allotropique en vue de développer une théorie générale des diagrammes de phases. Un résultat général de ces études est que la symétrie structurale augmente avec la pression appliquée.

Un débat récent sur l'existence du polymorphisme á l'état liquide vient d'ouvrir un nouveau domaine de recherche et de nombreux travaux ont cherché á montrer l'existence d'une transition du premier ordre liquide-liquide. L'observation d'un changement important dans le diagramme de diffraction du phosphore liquide par Katayama semblait en fournir un exemple. Cependant un examen approfondi du diagramme de phase du phosphore montre une absence de données suffisamment précise pour trancher de manière définitive sur la nature de cette transition fluide-liquide. Le soufre parat être un des meilleurs candidats pour étudier le polymorphisme et réaliser également une étude approfondie de la transition liquide-liquide.

Chapter 1

Polymorphism

...every compound has different polymorphic forms and the number of known forms is proportional to the time and money spent in research on that compound (all the common compounds show polymorphism)

McCrone (1965)

This first chapter introduces the concept of polymorphism and the motivations that lead to the large number of studies performed on this subject.

After a general introduction, we will focus on the thermodynamic aspects of phase transitions, and the various problems related to assessment of thermodynamic and kinetic stability will be underlined. The effect of pressure and temperature on the structure of crystalline solids is discussed.

In the last section the attention will be focused on the correlation between solid and liquid polymorphism.

1.1 Definition of polymorphism

The term polymorphism derives from the Greek word *poly* that means "many" and *morphs* that means "forms", it specifies the diversity of nature and it is used in many disciplines. In physics, polymorphism is a common property: most of the elements and compounds present different structural forms. A polymorph or an allotrope (in the case of a *pure* element) is defined as a solid phase which differs in its crystal structure, and consequently, in its diffraction pattern, from the other polymorphs of that substance. This definition can be extended to liquids and amorphous phases that may be characterized either by their diffraction patterns or by suitable spectroscopic methods.

Polymorphism is one of the possible responses of a system to an external perturbation. Different structures of the same substance can be obtained in different ways: a particular crystallization method, a chemical reaction, a change of the external thermodynamic conditions, *etc.* The structural changes result from the tendency of the system to minimize its Gibbs energy [1].

In this thesis, we are involved with structural changes induced by pressure and/or temperature variations. The only way to conduct a study on phases that are in their stable thermodynamic regime is to allow the system to reach the equilibrium conditions. Obviously, the kinetic rate of transformation could represent a constraint in this sense: a slow rate could prevent such transformations in the short times of our experiment and metastable forms could be formed instead. The criteria we will consider in checking the thermodynamic validity of a transition line are: the coexistence of two phases in equilibrium at a transition point, and the reversibility of that transition. For that reason, our experiments have been necessarily conducted *in situ*. The study of the stability regimes combined with the study of the crystal structures can also provide information on the factors governing the mutual stability between two polymorphs.

A good knowledge on polymorphism has not only important theoretical consequences but also economic. In recent years, the scientific literature production on polymorphs is increasing exponentially, and in parallel with it, the number of related industrial applications. The systematic characterization of polymorphic forms and the ability to synthesize a desired form are, in fact, additional elements in the design strategy of new materials.

1.2 Thermodynamics of phase diagrams

The systematic study of the polymorphism of a substance, is built from knowledge of its phase diagram. Several kinds of calculations can be conducted to generate phase diagrams of simple systems. They can be, for example, generated by the analysis of the basic thermodynamic properties of a system or by using ab-initio calculations [6–9]. Despite the important progresses in the development of new theoretical models, it is clear that the fulfilment of a general theory on polymorphism requires comparison with experimental data. In figure 1.1 for example, we report the phase diagram resulting from

[1] *Note that, despite that the system has the tendency to minimize its free energy, the transition to a thermodynamically stable polymorph strictly depends on the nature of the perturbation and on the presence of kinetic barriers.*

a calculation (using the FP-LMTO[2] method) on titanium [10]. The calculated transition lines (straight line and stars) agrees qualitatively well with the few experimental points (crossed circles and triangles), but the number of experimental points is insufficient to refine and to check the reliability of the model.

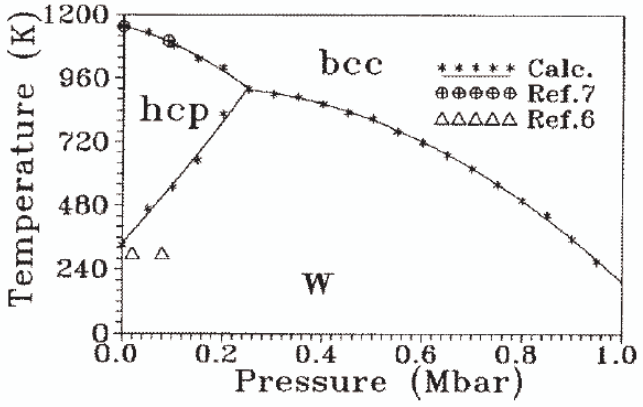

Figure 1.1: Calculated phase diagram of Ti from ref. [10].

If, on one side, we require models for the design of new materials; on the other side, theory requires experimental data to validate the consistency of its models. For that reason it is necessary to establish phase diagrams for elements and simple compounds as a function of p and T, including not only solid-solid transitions but also transitions between fluids.

Unfortunately, for several elements and simple compounds, the recorded phase diagrams are in need of revision. In fact, many of the "established" phase diagrams have been constructed following "quench recovery" experiments, with the consequent possible presence of metastable phases. The quench recovery method is based on the assumption that a thermodynamically unstable structure can exist when its conversion to some other structure proceeds at a negligible rate. Following this, a polymorph can be studied in a thermodynamic regime that is different from its own thermodynamic stability regime. Obviously this assumption is not universally true and it neglects that an abrupt perturbation, like a quench, can induce further metastable transformation. We will present an example of these problems in the following chapter.

The construction of reliable phase diagrams is most readily done through the identification of the phases (by X-ray diffraction, combined with spectroscopic methods)

[2]Full Potential Linear Muffin-Tin Orbital

during *in situ* experiments at variable p and T. Generally, the combination of *in situ* crystallographic and spectroscopic studies can lead to a detailed understanding of the structural basis of the phase diagram and the mechanism of the phase transitions.

What is the thermodynamic basis of a phase diagram?

When the free energy of reaction, ΔG, for the transformation of a structure to any other structure is negative, then this structure is *thermodynamically stable*. Since ΔG depends on the transition enthalpy ΔH and the transition entropy ΔS and ΔH and ΔS in turn depend on the pressure and/or temperature, a structure can be stable only within a certain range of pressures and temperatures. According to the thermodynamic relations:

$$\Delta G = \Delta H - T\Delta S \tag{1.1}$$

$$\Delta H = \Delta U + p\,\Delta V \tag{1.2}$$

where ΔU is the transition internal energy and ΔV is the volume variation, the following rules can be given for the temperature and pressure dependence of thermodynamically stable structures:

1. *With increasing temperature, T, the structures with a lower degree of order will be favored. Their formation involves a positive transition entropy ΔS, and the value of ΔG depends on the term $T\Delta S$ (eq. 1.1).*

2. *Higher pressures, p, favor structures that occupy a lower volume, i.e. that have a higher density. As their formation involves decrease of the volume (negative ΔV), ΔH will be smaller as the high pressure structure is denser (eq. 1.2).*

When the rate of a structural transition is negligible, the system persists in a state that is defined *metastable, inert* or *kinetically stable*. Since the rate constant k depends on the activation energy E_a and the temperature T, according to the Arrhenius equation:

$$k = k_0\, e^{-E_a/RT} \tag{1.3}$$

where k_o is a constant and R is the Boltzman constant, we have a kinetic stability whenever a negligibly low k results from a large ratio E_a/RT. As a consequence, at sufficiently low temperatures, a structure can be stabilized kinetically. Nonetheless, kinetic stability is not a well-defined term because the limit below which a conversion rate can be considered negligible is arbitrary.

A phase diagram represents graphically the information on a system in thermodynamic equilibrium. With the system in thermodynamic equilibrium, no information

about transformation rates, and neither physical nor chemical properties can be found in the phase diagram. Both the determination of the stable phases and the equilibrium between them are empirical, though the relationship with thermodynamics is fundamental. With that regard, there are two important notions that must be introduced: Gibb's phase rule and the condition for phase equilibrium.

A system in which C components are distributed in P phases is described by $PC+2$ variables, including pressure and temperature. These variables will be described by a set of equations: in a system of P phases, there will be P equations. The composition at the equilibrium is defined by $P-1$ terms for each component (for all the components, C, it is necessary to have $C(P-1)$ concentration terms). Thus, the number of degrees of freedom in the system are:

$$f \;=\; PC + 2 - P - C(P-1) \;=\; C - P + 2. \tag{1.4}$$

For pure elements (one component, $C = 1$), the number of degrees of freedom becomes $f = 3 - P$. When three phases are simultaneously in equilibrium with each other, e.g. vapor, liquid, and solid, then $f = 0$; there is no degrees of freedom, and the three phases coexist only at a singular pressure and temperature point, the triple point. A coexistence line is allowed for two phases in equilibrium ($f = 1$).

For a one-component system, δG can be written as:

$$\delta G \;=\; V\delta p - S\delta T \tag{1.5}$$

if two phases are in thermodynamical equilibrium, the free energy of the two phases is the same and then:

$$\frac{\delta p}{\delta T} = \frac{\Delta S}{\Delta V} \tag{1.6}$$

this is the Clapeyron's equation that defines phase equilibria. Another form of this equation, derived through combining eq. 1.1 and eq. 1.6 with ΔG=0, is:

$$\frac{\delta p}{\delta T} = \frac{\Delta H}{T\Delta V} \tag{1.7}$$

The Clapeyron equations define the slope of transition lines in one-component phase diagrams, and are valid for all phase equilibria.

1.3 Effect of p and T on crystalline structures

Crystalline solids exhibit a wide variety of structural responses to increasing pressure. Upon compression, deformation will occur, i.e. changes of the bond lengths take place

in the crystal lattice, up to transformations in which the system of chemical bonds is altered and the electron structure undergoes deeper rearrangements: valence electrons can be forced into the preceding shell, or "squeezed out" into the inter-atomic space; thus, transforming a dielectric into a metallic conductor. This sequence is typical for many substances, although the transition pressure varies widely.

In general, elements that have open packed crystalline structures transform toward dense-packed structures through successive pressure-induced phase transitions: the coordination number, CN, can increase at the transition. For example, silicon transforms from a diamond-like structure (CN=4), to a cubic structure (CN=12), going through several intermediate structures with increasing packing and CN [11–16].

The effect of temperature combined with pressure on crystalline structures is not easy to predict. On one side, it is perhaps logical to assume that temperature has the inverse effect of pressure on volume, so a temperature increase is associated to a dilatation that contrasts the pressure compression. On the other side, temperature comports a simultaneous increase of the atom's thermal motion that can lead to the formation of new phases and states (liquid or gas) at sufficiently high T.

New structures often exist only in high pressure-high temperature regimes. They can have the same basic structure and a different crystalline packing from the low-T counterpart (this is the case of orthorhombic and monoclinic sulfur presented in the following chapter) or a completely different base structure and crystalline packing (this is again retrieved in sulfur comparing the molecular and polymeric phases).

Unfortunately, high pressure studies and their further combination with high temperature, present many difficulties and only the recent development of new families of high pressure techniques (like the combined use of diamond anvil cells and synchrotron radiation) has opened the way to a new class of experiment. For this reason the study of matter under extreme conditions is still a new and promising field. Through performing high pressure and high temperature studies, we not only have the possibility of observing new solid phases and synthesizing new materials but we can also explore the physics of the liquid state.

1.4 Solid and liquid polymorphism

In the solid state, the occurrence of polymorphism is related to structural differences between well-defined crystalline structures. In the liquid state (or in amorphous substances) the occurrence of polymorphism is related to changes in the short or medium

range order, induced by pressure or temperature changes. This kind of polymorphism is defined *polyamorphism*, because it deals with amorphous phases [17].

The structural response to an increase in pressure, in the liquid state, like in the solid state, depends on the anisotropy in bonding. It is expected that liquids with open-packed local structures will evolve into dense-packed local structures under high pressure. In effect, measurements on several liquids show, by increasing pressure, an increase of the coordination number [18, 19], or, in other cases the evolution towards denser polymeric structures [1, 19].

The structural changes in the liquid and in the solid state have different characteristics. The liquid state is characterized by rapid motions of atoms, the lack of long-range order, and a broad distribution of the local atomic arrangements. This broad distribution smooths the structural change that would correspond to an abrupt phase transition: local structures (perhaps related to the short/medium range order of crystalline phases) are probably mixed in the liquid state (or are evident at different length scales). This smoothing, however, does not mean that the structural changes in the liquid are necessarily monotonic. For example, a good indication for the presence of pressure-induced changes in the liquid is the occurrence of a maximum in the melting curve [20]. If there is an unique solid phase below the maximum of the melting curve: a) in the region where the melting curve has a positive slope, the molar volume of the liquid is greater than in the solid; b) in the region where the melting curve has a negative slope, the molar volume of the liquid is less than in the solid. In this case, the occurrence of a maximum may indicate an anomalous change in volume in the liquid state.

Although the melting curves of most elements increase monotonically with increasing pressure, the melting curves of some elements such as Cs, Se, Ge, Bi, P (figure 1.2) and Te have a maximum.

A two species model has been formulated by Rapoport [20] to explain the density changes in the liquid around a melting curve maximum. According to Rapoport's model, some liquids are assumed to consist of two species with a transition to the denser species taking place continuously with increasing pressure. Around the melting curve maximum a rapid change of concentration of the two species may induce a transition.

This model also explains the correlation between the polymorphism in the solid and in the liquid states. It is noted, in fact, that in the known cases where maxima in the melting curves are present, the crystalline solid also exhibits a solid-solid phase transition at some higher pressure, accompanied by a large volume change [20], and usually a change in coordination. The crystalline structure of the two solid phases

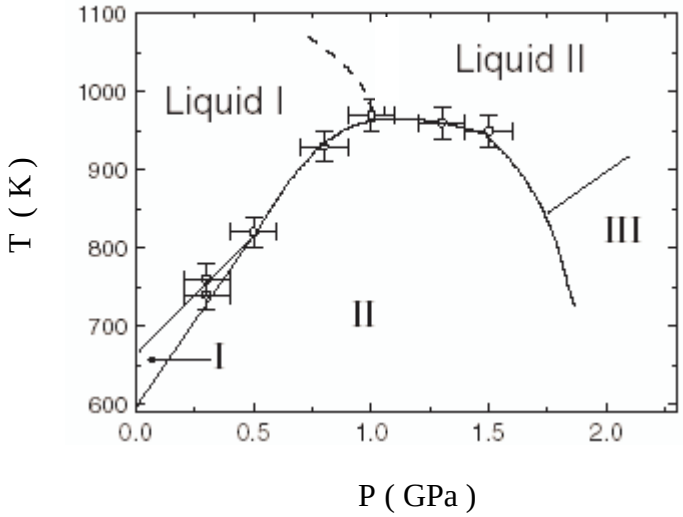

Figure 1.2: The pressure-temperature phase diagram of phosphorus from ref. [1].

can be correlated with the local structures in the liquid: the local structure of the low density species is close to the local structure of the low density solid, while the local structure of the high density species is close to the local structure of the high density solid.

In recent years, studies of polymorphism in the liquid state have been strongly encouraged by the debate centered around the possible existence of liquid-liquid (L-L) phase transitions. In particular, the debate is open on simple, single component systems. The coexistence between chemically distinct liquid phases is, in fact, commonly observed in multicomponent systems. Many binary liquids display a "*miscibility gap*", where below a certain temperature the melt separates into two liquid phases: one liquid phase rich in component A and another liquid phase rich in component B. The unmixing of the liquids occurs because favorable atomic interactions win out over entropy at lower temperatures.

In single component systems, such compositional variable cannot exist. In these systems the transition is driven by density or entropy rather than fluctuations in chemical composition. Although no thermodynamic principles are violated by a L-L transition in a single component system, the experimental evidence of such transformations is sparse, and reports of such liquid behavior have sparked much controversy.

In figure 1.3 we have reported the phase diagram of phosphorus. Phosphorus is a good candidate for a L-L phase transition: an open structure of the liquid at ambient pressure, a maximum in the melting curve associated with a higher pressure solid-solid

transition. Effectively, phosphorus exhibits an abrupt structural change between two stable disordered states above the melting temperature when the pressure is slightly changed at p around 1 GPa and 1000 ^{o}C (figure 1.3) [1, 2]. The transformation is characterized by a sharp increase in density of about 40% and, for this reason, it has been interpreted as a first order L-L phase transition [1]. The low-pressure local structure in the liquid has been associated with tetrahedral P_4 molecules, which characterize the molecular structure of solid white phosphorus. The high-pressure local structure has been suggested to be polymeric and it has been associated with amorphous red phosphorus [1].

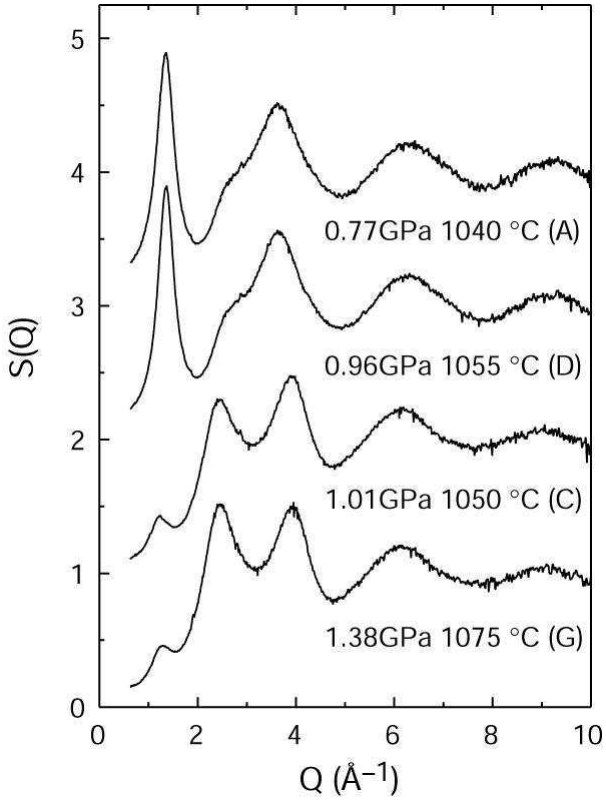

Figure 1.3: Structure factor, S(Q), for liquid P at several pressures. Picture from ref. [1].

Another good example is sulfur. Sulfur exhibits the so-called λ-transition at 1 atm and 159^{o}C, [21] and references therein. This transition is accompanied by a drastic change in viscosity with increasing temperature [22]. As for phosphorus, this change is due to the formation of long polymer chains starting from molecular species (mainly S_8 ring molecules). Unlike phosphorus however, in the case of sulfur, the initial polymer concentration is very low, and increases with the temperature increase. Actually, a molecular-polymeric structure transition has been observed in the solid at high p and

T [23].

The observation of liquid-liquid transitions remains an experimental challenge; liquid-liquid transitions may be located at high temperatures and high pressures for atomic liquids or may be hidden by crystallization, which maybe is the case of water [24]. The development of high pressure devices (such as the Paris-Edinburgh press and the diamond anvil cell described in the third chapter), combined to the synchrotron and neutron radiation, have allowed for the development of *in situ* techniques that have widely reduced these experimental limits. For example, it is relatively easy to carry out diffraction experiments on p,T induced polymorphic transitions: indeed, the natural tool for the study of polymorphism is diffraction. This is because the information we obtain from a diffraction pattern is directly related to the structure. However, diffraction patterns obtained from crystalline and non-crystalline matter are very different due to the lack of long range order in the latter case. In the liquid state, the atoms are in rapid motion around preferred local structures. Therefore, the measured structure factor of a liquid corresponds to a snapshot of a dynamic system.

The local order, characteristic of the liquid state, makes the structure factor of a liquid relatively simple. The broad distribution of the atoms around an average position smooths out the diffraction peaks. These effects complicate the interpretation of the data and the description of the atomic arrangements. An appreciable change in the structure factor of a liquid requires a relevant change of the local structure or a relevant density change. Most of the transitions observed in the liquid state, are instead characterized by continuous changes with pressure and temperature [18, 19, 25] and references therein.

Unfortunately, in order to extract detailed information on the local structure of a liquid, reliable density data are required. Despite several experimental methods having been developed to measure the density of a liquid at high p,T conditions [26, 27], in most of the cases the exact density is unknown. As an alternative, the nature of a transition can be more easily understood through comparing with theoretical models or by the complementary use of spectroscopic techniques. For example, in the case of sulfur, Raman spectroscopy has been proven to be as an excellent complementary technique (see chapter 4).

Résumé du chapitre 2

Parmi tous les éléments le soufre est celui qui présente le plus grand nombre d'allotropes. Pour la plupart d'entre eux, ils ont été synthétisés par voie chimique ou obtenus hors d'équilibre. De nombreuses mesures en vue de l'élaboration du diagramme de phase ont été réalisées sur des échantillons trempés. Les formes orthorhombique et monoclinique du soufre sont des allotropes stables á la pression atmosphérique, construits á base de molécules S_8. Le soufre orthorhombique est la forme stable de la température ambiante á 98°C puis il devient monoclinique jusqu'á la fusion á 119°C. Le soufre rhomboédrique est un allotrope obtenu par voie chimique ; sa structure est á base de molécules S_6. Il a été observé par spectroscopie Raman mais pas par diffraction. Le soufre trigonal est la première forme stable á haute pression et haute température qui ait été observée in situ. Sa structure est caractérisée par de chaînes hélicodales á projection en triangle. Le soufre tétragonal est le plus récent allotrope du soufre observé et caractérisé á haute pression. Il possède une structure polymérique avec des chaînes se projetant sur des carrés. Le soufre fibreux est une autre forme polymérique obtenue par relaxation lente de la pression.

Le soufre liquide a fait l'objet de nombreux travaux de recherche essentiellement motivés par l'existence d'une transition brutale de viscosité et chaleur spécifique, (transition). Les résultats essentiels montrent qu'á basse température le soufre liquide est formé en majorité d'anneaux S_8. Puis, á 159°C s'amorce une polymérisation en très longues chaînes, en équilibre avec les anneaux : la proportion d'atomes de soufre dans les chaînes augmente alors avec la température tandis que leur taille passe par un maximum vers 187°C puis diminue.

Chapter 2

Allotropes of sulfur

Sulfur research, like the population explosion, is increasing without limit.

D.Barnes - The Sulphur Institute - 1965

Among the elements, sulfur has the largest number of observed allotropes . This chapter traces the history of the phase diagram of sulfur, looking at the origin of its complexity.

There are several books and reviews that summarize and describe the different allotropes of sulfur that can be obtained by chemical synthesis or through changing the external pressure and temperature. In the next part of this chapter, we describe only the structures of the allotropes of sulfur that are necessary background for the understanding of chapters 5 and 6, where we will present our reconstruction of the phase diagram of sulfur.

In the second part of the chapter the attention will be focused on the behavior of sulfur in the liquid state, in particular, by looking at the information we have on the well-known λ-transition.

2.1 Sulfur: The state of the art

Sulfur has been and is one of the most studied elements, because of its structural variety. Historically, orthorhombic sulfur (i.e. the stable form at ambient conditions) was one of the first crystalline structures to be characterized by X-ray methods [28], and continues to be subject of much fundamental crystallographic study [29]. Since then, more than

50 sulfur allotropes have been described), offering crystallographers a rich panorama of different structures to study.

Despite this rich literature, our knowledge on the phase diagram of sulfur is still confused. For example, several different melting curves [30–35] have been proposed in the literature.

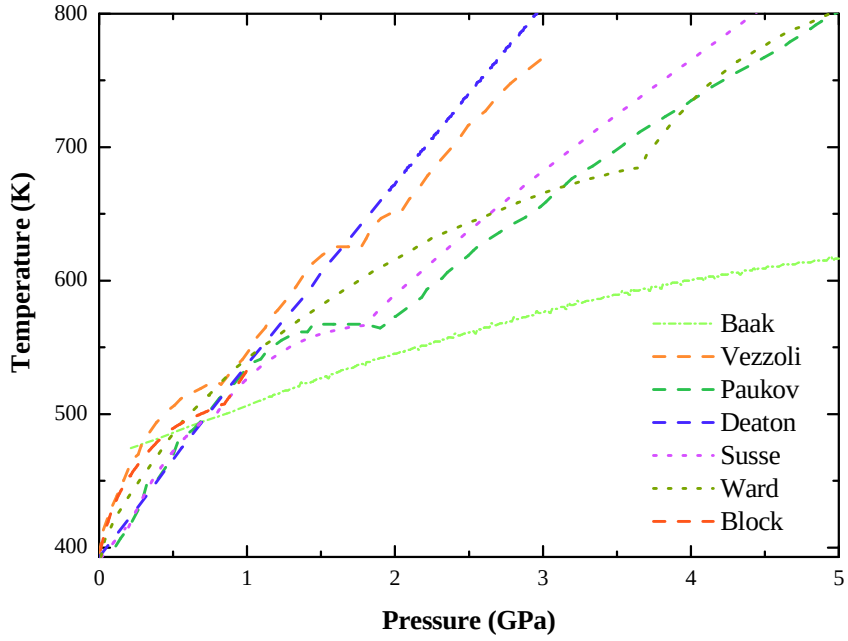

Figure 2.1: Reported melting curves of sulfur. (**violet, dot**) Susse, Epain and Vodar [31]; (**green, dash-dot**) Baak [32]; (**blue, dash**) Deaton and Blum [33]; (**dark green, dash**) Paukov, Tonkov and Mirinski [30]; (**dark green, dot**) Ward and Deaton [34]; (**orange, dash**) Vezzoli, Dachille and Roy [35]; (**red, dash**) Block and Piermarini [36].

In figure 2.1, seven melting curves of sulfur reported in literature have been plotted. They have been measured using differential thermal analysis (DTA) [30,31,33,34], quenching [32,35] techniques and by visual microscopic examination [36]. Considering the available data below 5 GPa, not only are there major differences in the general slope of these curves, but also in the number of triple points, so that: one set of investigators found evidence of three polymorphic transitions [35], three sets found evidence for one transition [30,31,36], and three sets, no evidence for any transition [32–34].

A one serious difficulty in the construction of the melting lines is represented by the calibration of pressure and temperature. In figure 2.2 the two melting curves proposed by Paukov *et al.* [30] and Susse and Epain [31] are reported for a direct comparison.

The melting curve of Paukov *et al.*, obtained by thermal analysis, is extended up to 10 GPa suggesting the presence of two triple points around 2 GPa, 565 K and 9 GPa, 920 K. The presence of two maxima is also reported, one at around 1.6 GPa, 583 K and the other near 8.5 GPa, 940 K. Comparing this curve with the one of Susse and Epain, a good agreement persists up to the first triple point, however, in the data of Susse and Epain, the second triple point is observed at 7.8 GPa, and 950 K and the second maximum at 7.3 and 965 K. It is likely that the disagreement is not qualitative but perhaps comes from estimations of the pressure-temperature conditions.

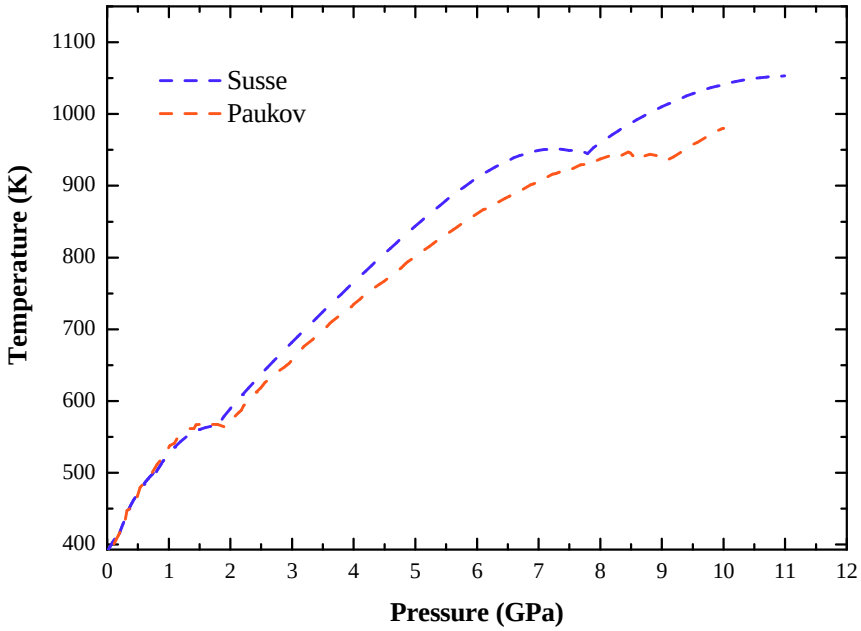

Figure 2.2: Comparison between the two melting curves measured by Susse *et al.* [31] (*red*) and by Paukov and Tonkov [30](*blue*).

Vezzoli el al. [35] have discussed the factors responsible of the divergence among these literature's results: "*These factors would include the nature of the starting material, types of pressure systems used, details of technique and sample configuration*". Other than the different experimental sources of error, it has to be noted that, almost all of these melting curves have been obtained by *ex situ* p,T calibration. The only *in situ* p-T calibration are those of the measurements of Block and Piermarini [36]. Their data have been collected by using a diamond anvil cell (DAC), measuring the temperature with a thermocouple and an optical system that utilizes the ruby fluorescence for pressure calibration (see next chapter). Block and Piermarini have visually evidenced

the simultaneous presence of four different phases, hypothesizing that the system was in "non-equilibrium" conditions. In any case, the structure of these phases have not been characterised *in situ*.

In order to clarify the discrepancies between the various results on sulfur, Vezzoli *et al.* [37] have performed a detailed mapping of its phase diagram. This phase diagram contains twelve crystalline fields below 5 GPa. Their results deal with X-ray measurements on samples quenched to -20^{o}C from melts at various pressures and temperatures, together with transitions detected by volumetric, optical, and electrical resistance variations. The proposed crystalline phases have been characterized *ex situ*. The resulting phase diagram is shown in figure 2.3. Phase I, II, and XII were identified as α-orthorhombic, β-monoclinic, and fibrous sulfur respectively; phases V, VIII, and IX were said to revert completely to orthorhombic sulfur despite the rapid quenching. The remaining six phases were considered different from any other form of sulfur. No phase transitions were observed at room temperature by X-ray diffraction up to 5 GPa [38] and by specific volume measurements up to 10 GPa [39].

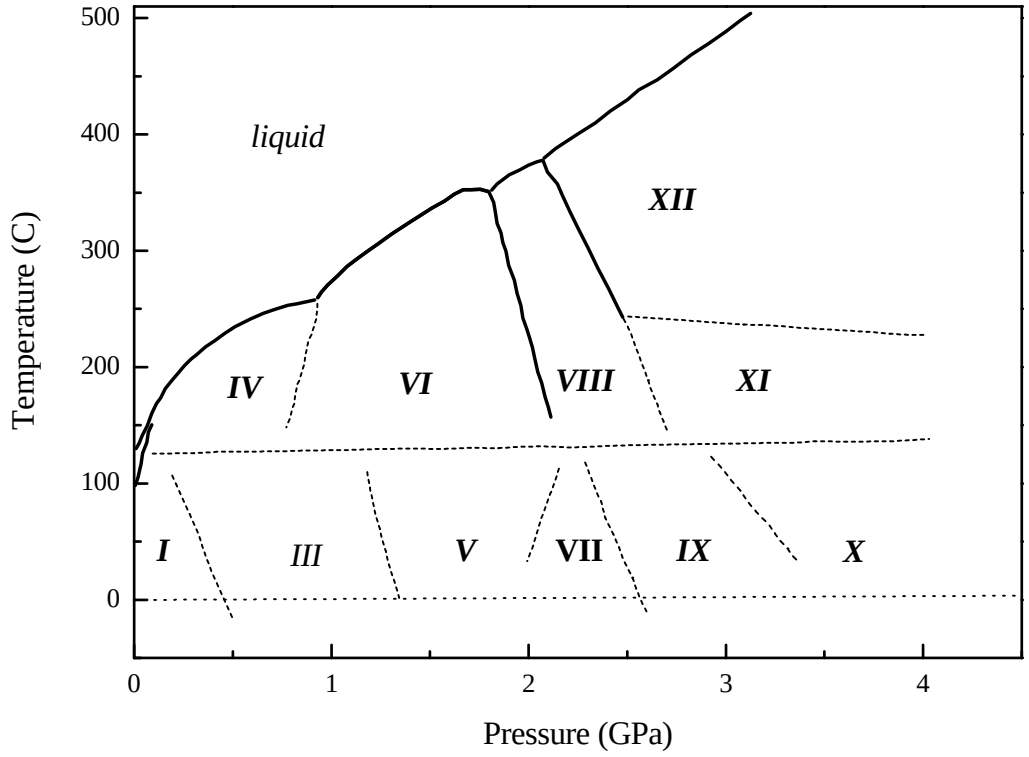

Figure 2.3: Phase diagram of sulfur from ref. [37].

Another phase diagram for sulfur has been proposed by Ward *et al.* [34]. This phase

diagram, determined by DTA , consists of: a) the melting curve from ambient pressure to 6 GPa; b) an horizontal solid-solid transition at about 405^{o}C at pressures above 4 GPa. The melting curve of Ward *et al.* is reported in figure 2.4. The solid-solid phase transition is irreversible, it is referred to an orthorhombic-fibrous sulfur phase transition. This transition has aspects of both, the XI-XII transition and the VIII-XII transition reported in the phase diagram of Vezzoli (figure 2.3). The first one because of its slope and the second because of the position of the triple point.

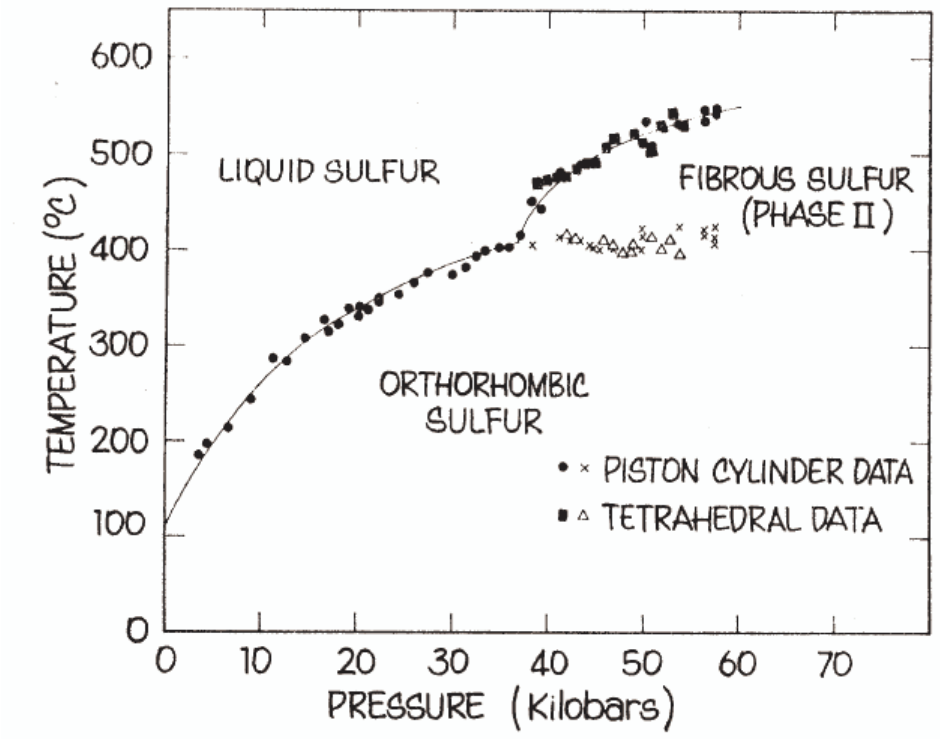

Figure 2.4: Phase diagram of sulfur from ref. [34].

The twelve crystalline fields proposed in the phase diagram of Vezzoli follows numerous previous papers on the observation of several high pressure phases of sulfur [40–43]. Further comparisons (see [44] for a review) demonstrate that most of these phases, obtained by different thermodynamic paths and observed *ex situ*, give diffraction patterns and/or Raman spectra that correspond to fibrous sulfur.

If we consider the pressure range limited to few GPa, the progress on the elucidation of the phase diagram of sulfur are recent. From the X-ray diffraction study performed *in situ* by Crichton *et al.* [23], the presence and the structure of a new high pressure polymeric phase is revealed around 400^{o}C and 3 GPa: the trigonal sulfur. This sulfur

form reverts to mix of S_8 and fibrous sulfur close to room conditions. Considering that the large number of high pressure phases further identified as fibrous sulfur [44], have been studied at ambient conditions, we suggest that fibrous sulfur represents a back-transformation product of high pressure phases.

At room temperature orthorhombic sulfur is the most stable form in a wide pressure range. Recently, a new tetragonal polymeric structure has been observed and refined at 55 GPa by Fujihisa *et al.* [45]. In another recent work, Degtyareva *et al.* [46] have proposed a scheme of high pressure phase relations in which this phase has been observed up to 83 GPa and moderate temperatures.

Other structural transitions have been observed at higher pressures [47–50] and low temperature [51], but they do not concern directly the present dissertation. However, we briefly report the sequence of structural transitions of sulfur by increasing pressure at room temperature:

$$Orthorhombic\, Fddd \rightarrow Tetragonal$$

$$Tetragonal \rightarrow body-centered\, Orthorhombic$$

$$body-centered\, Orthorhombic \rightarrow \beta - Po\, Structure.$$

These transitions are observed respectively at 36 GPa [45,46], 83 GPa [46] and between 129 and 135 GPa [50]. Measuring the pressure dependence of reflectivity, Luo *et al.* [52] suggest that at 95 GPa sulfur undergoes a pressure-induced metallization. This metallization could correspond to the tetragonal→body-centered-orthorhombic transition observed by diffraction at 83 GPa.

2.1.1 Orthorhombic and monoclinic S_8

The stable form of sulfur at room pressure and temperature is the orthorhombic structure. Orthorhombic sulfur is also called rhombic sulfur, Muthmann's sulfur I, and α-sulfur (the latter is more commonly used in the literature). At about 98^{o}C a powered sample[1] of α-S_8 transforms to monoclinic sulfur which is stable up to the melting temperature of about 119^{o}C [54]. The transformation is reversible. The monoclinic allotrope obtained by heating a powder of orthorhombic sulfur at 98^{o}C or formed by crystallization from the melt at atmospheric pressure is normally called β-monoclinic sulfur or, more simply, β-sulfur [54].

[1]The transformation of single crystals of α-S_8 to β-S_8 is kinetically hindered [53].

Both the α-orthorhombic and β-monoclinic sulfur are based on S_8 molecular units [44]. The geometry of the molecule in the two structures is almost the same, although the bond lengths, bond angles and torsion angles are influenced by the different packing environments (the structural parameters relative to the correspondent molecules are reported in Table 2.1). The S_8 molecule has a crown shaped, puckered conformation; the dihedral angles alternate in sign so that a zig-zag ring with point symmetry D_{4d} is obtained [53].

Point Symmetry $\overline{8}2m - D_{4d}$		
Allotrope	$\alpha - S_8$	$\beta - S_8$
Bond lengths(Å)	2.046(3)	2.05(2)
Range	2.038-2.049	2.009-2.077
Bond angles(^{o})	108.2(6)	107.7(7)
Range	107.4-109.0	106.2-108.9
Torsion angles(^{o})	98.5(19)	99.1(1.7)
Range	96.9-100.8	95.9-101.5
Temperature (K)	298	218
Reference	[29]	[55]

Table 2.1: Molecular parameters of the S_8 molecule in the α-orthorhombic and β-monoclinic structures from ref. [53]

In the orthorhombic allotrope the rings are arranged in two layers each perpendicular to the crystal c axis forming a so called "crankshaft structure". The primitive cell contains four molecules on sites of C_2 symmetry.

The structure of monoclinic sulfur consists of S_8 rings in two kind of positions. Two thirds of the rings form the ordered skeleton of the crystal while the other molecules are on pseudo-centric sites. The disorder is two-fold, the alternate position is obtained by a rotation of 45^o around the principal axis of the molecule [53]. The orthorhombic and monoclinic structures are reported in figure 2.5 and 2.6 respectively.

The densities of the two allotropes are respectively 2.066 g/cm^3 for α [29] and 2.008 g/cm^3 for β sulfur [55]. The color of orthorhombic sulfur is light yellow, while monoclinic is yellow-orange.

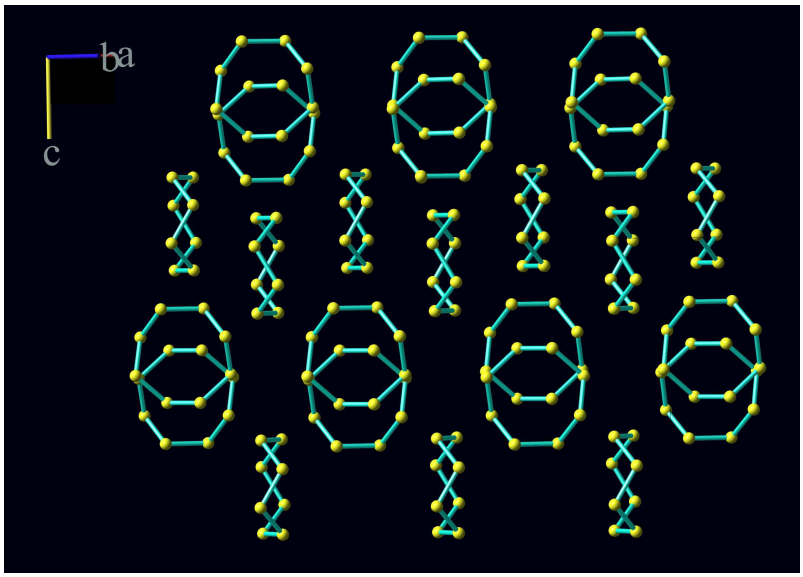

Figure 2.5: The crankshaft structure of S_8 molecule in orthorhombic sulfur.

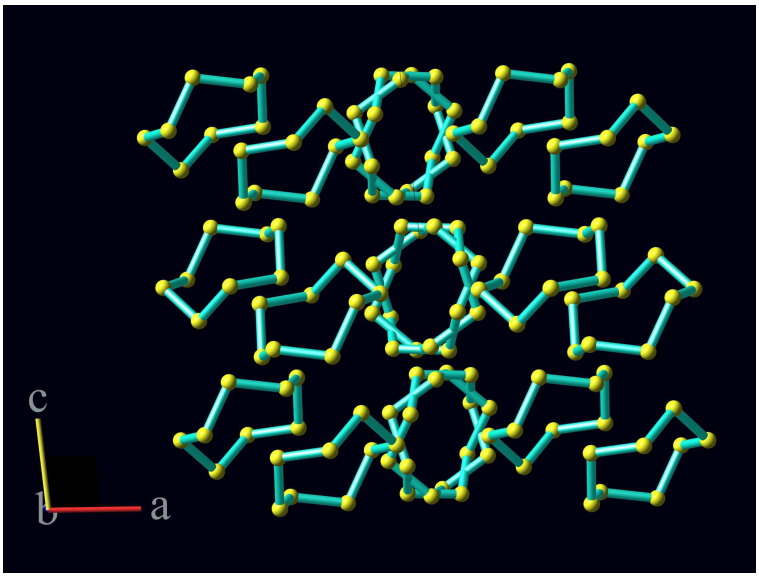

Figure 2.6: The structure of monoclinic sulfur projected along the crystal b-axis. The two possible orientations of one third of the molecules are reported by the two alternate position in the central rings. They transform one to the other by rotation around the C_4 axis of 45^o.

2.1.2 Rhombohedral S_6

The S_6 cyclic molecule of sulfur was firstly synthesized chemically by Engel in 1891 at room pressure [56, 57].

The structure of S_6 has been determined by Steidel *et al.* [58] at 183 K. Their structural refinement shows that three S_6 rings in the chair conformation fill the $R\bar{3}$ unit cell; the correspondent cell parameters are a=10.766(4) Å and c=4.225(1)Å. The S_6 molecule has a S-S bond length of 2.068(2) Å and a torsion angle of $73.8(1)^o$.

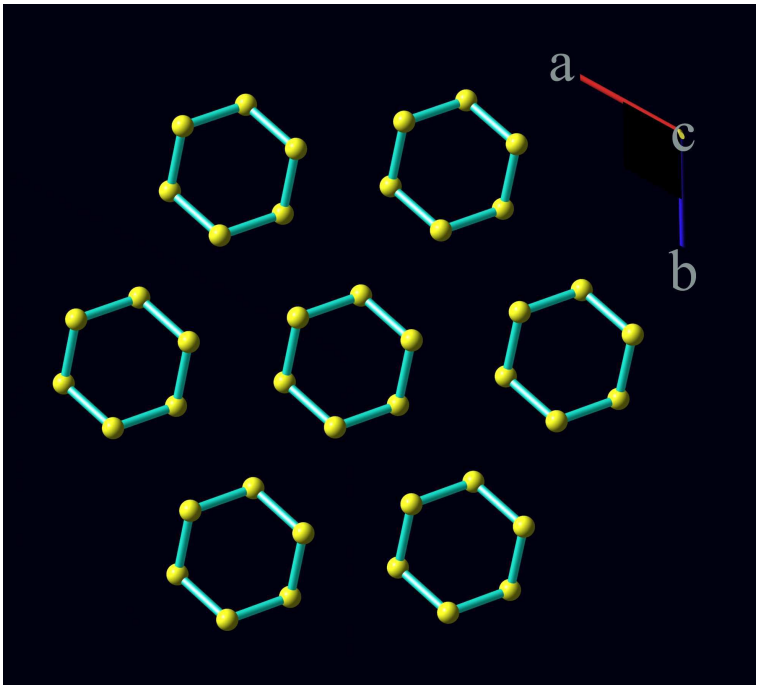

Figure 2.7: The structure of rhombohedral sulfur projected along the crystal c-axis. The direction of the c-axis corresponds with that of molecular z-axis.

The density of rhombohedral cyclohexasulfur is 2.26 g/cm^3 [58], the highest density of any sulfur forms at room pressure and temperature [44]. The density reflects the efficient packing of the molecules which, themselves, contain their atoms in a tighter packing than cyclooctasulfur, even though the S-S bond length is slightly longer.

2.1.3 Trigonal polymeric sulfur

As we introduced in the first paragraph, trigonal, like tetragonal sulfur phases are stable polymeric phases that have been identified only recently. The trigonal phase is the first polymeric phase of sulfur to be observed *in situ* [23] at high p-T conditions (3 GPa and 400^oC), and characterized.

The structure of this allotrope of sulfur is basically formed by two helical chains both with a triangular projection but with different bond lengths and S-S-S bond angles. The space group is $P3_221$ and the parameters of the hexagonal unit cell are a=6.976(1) Å and b= 4.3028(6) Å at 3 GPa and 400^{o}C. The unit cell contains nine atoms on two unique sites. The corresponding density is 2.559 g/cm^3 [23].

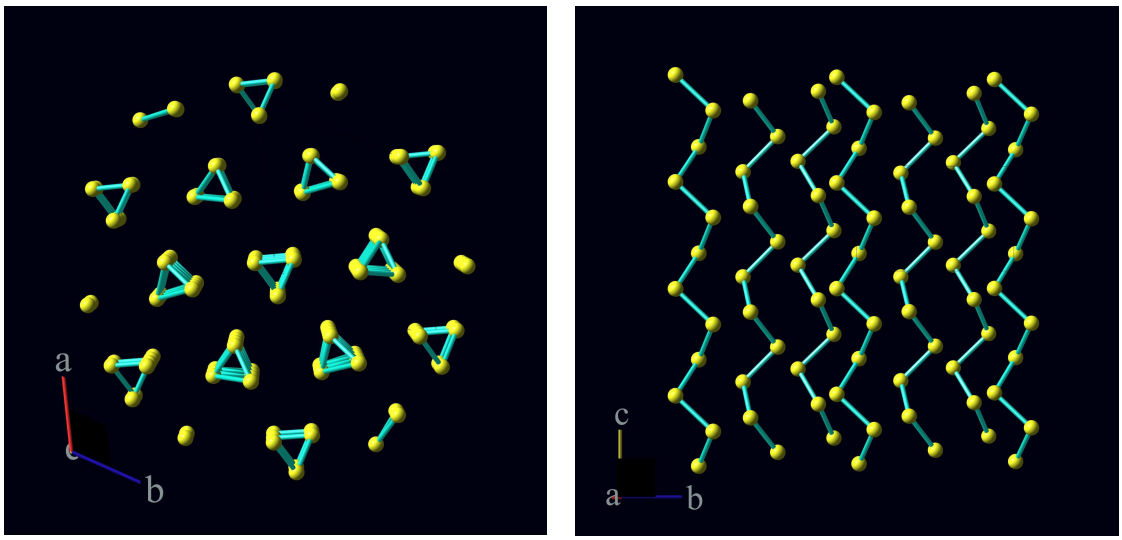

Figure 2.8: The structure of trigonal sulfur projected along the crystal c-axis in order to show the triangular projection and along the crystal a-axis to visualize the two different chains.

The two chains repeat along the c axis with one turn including three atoms ($^3S_1$ helix). The respective bond lengths and bond angles for the two helices are 2.070(4) Å and 102.7(2) ^{o} for the helix 1 and 2.096(7) Å and 101.7(3) ^{o} for the helix 2. This structure has observed to transform at pressures below 0.5 GPa to a phase which has been reported earlier by other authors and called fibrous sulfur [23]. The trigonal polymeric chains are represented in figure 2.8.

A structure similar to this polymeric form of sulfur have been also observed in selenium, despite the helical chains being slightly different [59].

2.1.4 Tetragonal polymeric sulfur

The polymeric tetragonal phase is a very recent addition to the ensemble of sulfur allotropes. Firstly, Fujihisa *et al.* [45] have observed and characterized this helical structure at pressures around 55 GPa and, in another study, Degtyareva *et al.* [46] have indicated the range 36-83 GPa as the stability regime of this phase at room temperature. Hejny *et al.* [48] indicates the value 37.5(1.5) GPa as transition pressure at room

temperature for the orthorhombic-tetragonal transformation. This transition is not reversible and on decreasing pressure, tetragonal sulfur also back-transforms to fibrous sulfur (1.5 GPa at room temperature [46]).

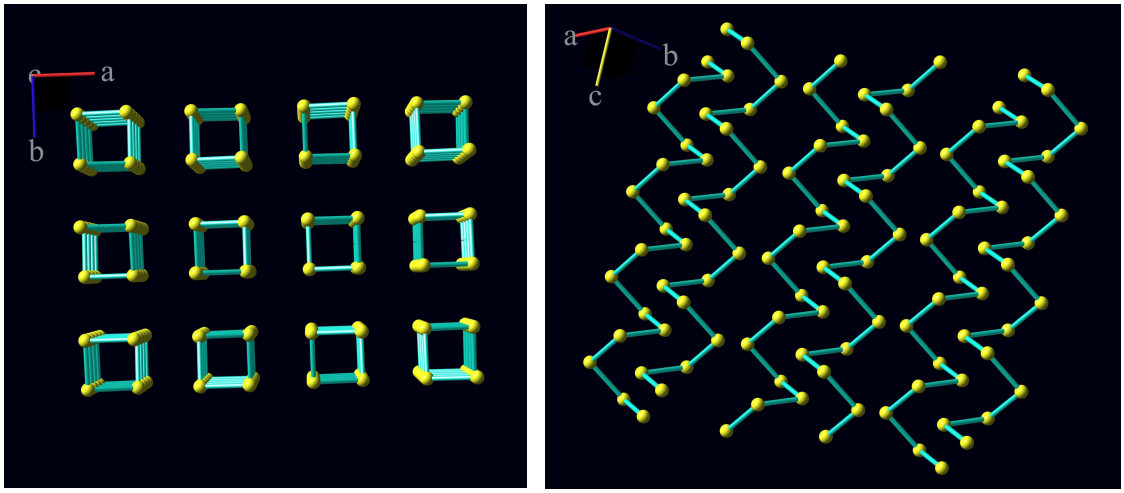

Figure 2.9: The structure of tetragonal sulfur represented similarly to the trigonal structure in figure 2.8 in order to allow the direct comparison. On the left, the structure is projected along the crystal c-axis showing the squared projection and at right the projection shows the packing and the turn (each 4 atoms) of the chains.

Tetragonal sulfur is formed by polymeric chains with a squared projection. The space group for this structure is $I4_1/acd$, which is made up of 16 atoms in the unit cell. The structure consists of spiral chains with squared projection [45]. The parameters of the unit cell are a=7.841(1) Å and c=3.100(1) Å at 55 GPa, as given by [45]. The correspondent density is 4.47 g/cm^3. The tetragonal polymeric chains are represented in figure 2.9.

A tetragonal structure identical to this structure of sulfur has been observed in selenium [45]. An analogous structure has not been seen in other elements.

2.1.5 Fibrous sulfur

Crystalline samples of fibrous sulfur can be prepared by stretching freshly quenched liquid sulfur or by drawing filaments directly from a hot sulfur melt. The quenched melt (plastic sulfur) is viscoelastic and transparent yellow but slowly transforms into an opaque crystalline material at room temperature. After several days the material contains the polymer, a fraction of S_8 rings, and traces of S_7. Other molecular forms, normally present in the melt [21], have converted to either polymer or S_8. The ring

fraction can be extracted by washing the material with CS_2. The insoluble fraction of polymeric sulfur can be then crystallized (termed S_μ, or sometimes S_ω [53]).

If plastic sulfur is stretched (by a factor of about thousand of its original length) crystallization is induced [53]. The resulting filaments are mixtures of S_8 rings and polymeric sulfur. After extraction of the soluble ring fraction the fibrous crystalline allotrope is obtained. [53]

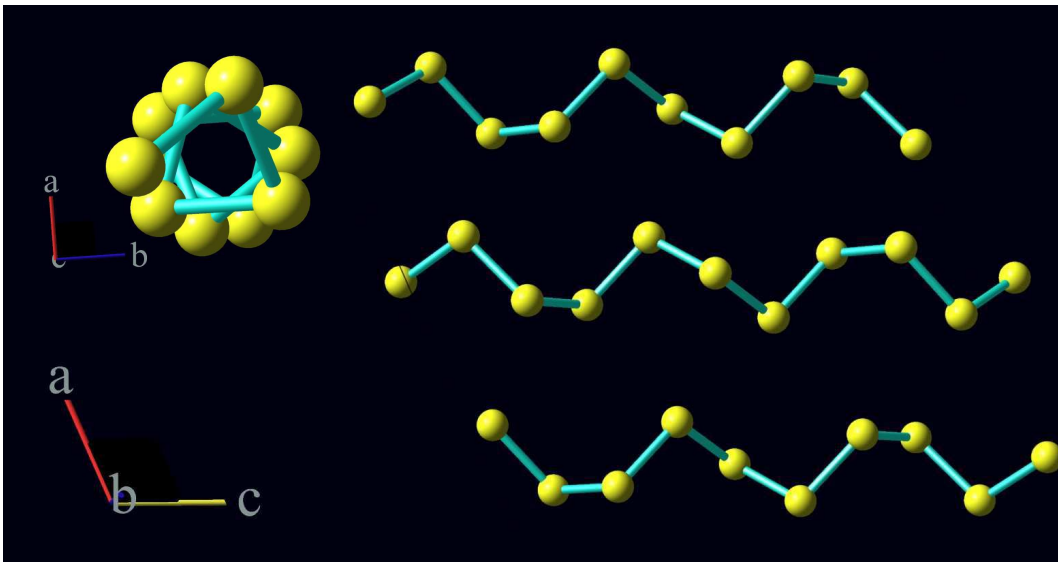

Figure 2.10: The proposed structure of fibrous sulfur from the model of Lind and Geller [60].

The structural characterization of fibrous sulfur has been discussed at length. Before 1956, various works in the literature discussed the structure of fibrous sulfur: a monoclinic unit cell was proposed by indexing the diffraction pattern and the number of atoms was derived from the density [44] or simply by comparison with the metallic chains of selenium or tellurium [61]. None of the proposed structures was tested by comparison of the observed intensities with those calculated from a set of atomic coordinates derived from a model, nor was the molecular packing explored in detail.

In 1956, Prins *et al.* [62] showed that the diffraction patterns of filaments of sulfur can be understood assuming a superposition of the patterns of two constituents, namely *catena*-polysulfur[2] and a metastable monoclinic form of sulfur called γ-S_8. After this, the fibrous sulfur was named S_ψ. Prins *et al.* [63] proposed a helical chain with a period of ten atoms in three turns with a length of 13.70 Å of the repeating unit.

[2]Name used for the polymeric chain in the solid state obtained by stretching a quenched sample of liquid sulfur or by drawing filaments from hot liquid sulfur.

In 1963, Prins and Tuinstra [64, 65] modified the model on the basis of new and improved data, by formulating alternating right- and left- handed helices. The unit cell of this arrangement is monoclinic, a=8.88, b=9.20 and c=13.7 Å, β=114^o, and contains 40 atoms. Again no comparison of the intensities was possible.

In 1966, Tuinstra proposed the refinement of 65 observed reflections giving a new orthorhombic structure, but defined the c-axis as "intermediate" [66]. This structure was based on helices containing 460 atoms in 137 turns. This structure has been severely criticized by Geller and Lind [67], and by Donohue *et al.* [68].

In 1966, Geller [40] synthesized single crystals of sulfur by first melting the sulfur at 2.7 GPa, then reducing the temperature below the melting and holding the sample at this temperature for three hours. Independently from the cooling rate, the final sample was plastic. Geller defined the sample obtained by this method: "very close but not exactly the same as" fibrous sulfur prepared by the method of Prins *et al.* [65]. The correspondence between the two phases was later pointed out by Lind and Geller [60], who stated that two photographs of fibrous sulfur and of the crystal of Geller superposed exactly one upon the other. The authors proposed an orthorhombic unit cell, without giving details on the molecular structure, but promising a complete structure analysis. Finally in 1969, Lind and Geller presented their structure model [60], describing the crystals as monoclinic, with a=17.6, b=9.25 and c=13.8 Å, β=113^o. The chains were described as ten-atoms three-turns helices, in a nearly closed packed arrangement. This unit cell is similar to that of Prins and Tuinstra [64, 65]. With the work of Lind and Geller [60, 67] the molecular and crystalline structure of fibrous sulfur seems to be well-constrained, though no modern refinement exist to confirm their model.

The chained molecules of fibrous sulfur have a helical conformation (figure 2.10). The chain bond length is similar to those of the trigonal helix 1 (see the paragraph on trigonal sulfur), the bond lengths are respectively 2.066 Å and 2.070(4). The helices are parallel and are regularly left-handed and right-handed. Efficient packing of the helices is attained by relative shift and rotations of the individual helices. A projection of the helices is shown in figure 2.10 together with a lateral view.

2.2 Liquid sulfur

Most of the studies on liquid sulfur have been conducted at ambient pressure around the well-known λ-transition.

At ambient pressure liquid sulfur exists at temperatures higher than 119^{o}C. The appearance and physical properties of this liquid differs in three distinct temperature ranges.

Immediately on melting, the liquid is purely molecular, based on S_8 unit rings. At 159^{o}C, with an increase in temperature, many properties of the liquid undergo a discontinuity (for example, the specific heat [69] and electroconductivity [70]). The most striking effect concerns, however, the temperature dependence of viscosity [22]. Above the melting point, the viscosity of liquid sulfur decreases like a *normal liquid*. At 159^{o}C, the viscosity suddenly increases by several order of magnitude, reaching a maximum value at 187^{o}C. At higher T, the viscosity of molten sulfur gradually decreases, and at 300^{o}C it becomes again that typical of a fluid substance [22]. These peculiarities of the physical properties are obviously linked to changes of the molecular structure. For that reason, the structure of liquid sulfur has been the subject of many experimental [71–77] and theoretical works [78–81].

An example of X-ray diffraction study, reported by Vavasenka *et al.* [72] is presented in figure 2.11. It illustrates the evolution of the structure factor as a function of temperature (130-300^{o}C) at ambient pressure.

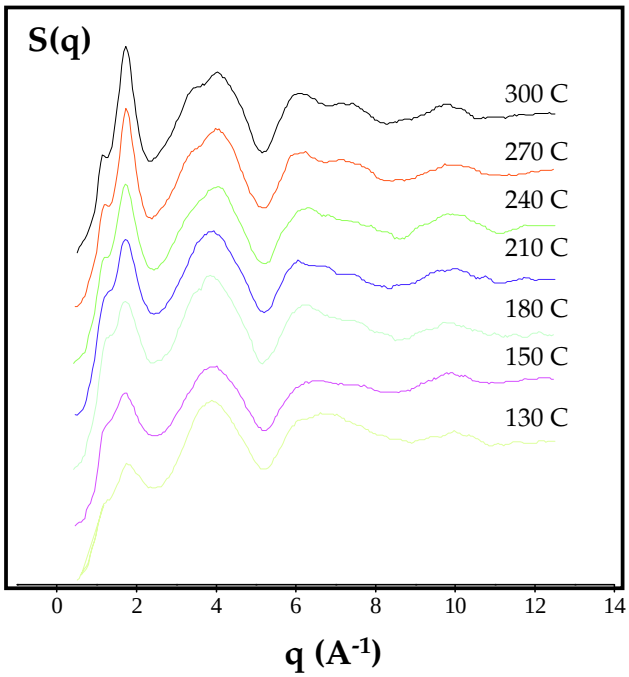

Figure 2.11: The structure factor evolution in liquid sulfur across the λ-transition at 159^{o}C from ref. [72].

Through comparison of the S(Q), it emerges that the structure factor shows very small difference for Q-values higher than 3 $Å^{-1}$. Bellissent *et al.* [74,75] have interpreted this feature, suggesting that the very short range order in the liquid does not change over the whole investigated temperature range.

This result is confirmed by the analysis of the pair distribution function: the positions of the low-r peaks in the pair distribution function are insensitive to the temperature increase. The coordination numbers corresponding to the first and second neighbors are almost constant whereas the third coordination sphere exhibits a decrease with temperature. The number of first neighbors at 2.06(1) Å is equal to 1.9(1) for all temperatures [71,72,74]. The number of second neighbors at 3.35 Å decreases from 3.12 at 130^{o}C to 2.92 at 300^{o}C [71]. The average coordination number around 4.5 Å varies from 7.52 at 130^{o}C to 6.45 at 300^{o}C (these values have been obtained from integration over the third coordination sphere considering a constant radius of 4.5 Å [71]).

After analysis of the coordination numbers and their temperature dependencies, Bellissent *et al.* [74] have also concluded that this behavior is consistent with a picture of a liquid made of S_8 rings at low temperature and a mix of rings and random chains above the λ-transition or polymerization temperature.

This picture is in agreement with the most of X-ray and neutron diffraction studies conducted on liquid sulfur, and it agrees also with the results obtained by other experimental techniques [21]. Nonetheless, an alternative interpretation of the diffraction data has been suggested in the literature. Based on their data analysis, Winter *et al.* [76] suggest that the local order in liquid sulfur is different from the solid molecular S_8, even immediately above melting. These authors have conducted a systematic investigation of liquid sulfur in a wide temperature interval by neutron diffraction [76]. It is noteworthy that the experimental values covered a wide range of wave vector from 0.2 up to 40 $Å^{-1}$. For Q < 0.2 $Å^{-1}$ the structure factor was extrapolated to $S(0) = \rho K_B T \chi_T$ using literature data on the isothermal compressibility χ_T and the number density ρ. Figure 2.12 shows the structure factor of liquid sulfur at 150^{o}C [76].

The shape of the first maximum of the experimental structure factor is very similar to the one of the structure factors obtained by earlier experiments. The first and second coordination distances are respectively 2.06 Å and 3.35 Å. The number of nearest neighbors was found to be less than 2 atoms for all temperatures. For the authors, this result may indicate that the local liquid structure near the melting temperature is not exactly the same as crystalline sulfur. Unfortunately, the value of isothermal compressibility χ_T of liquid sulfur reported in the literature is incorrect (see the sixth chapter), and then the coordination number calculated in ref. [76] is affected by error.

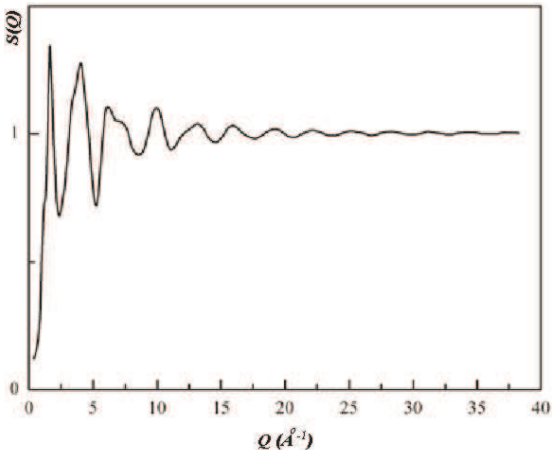

Figure 2.12: The experimental structure factor S(Q), for liquid sulfur at 150^{o}C [76]

The development of a theoretical model that matches well with the experimental structural data of liquid sulfur is a long standing problem. In ref. [76], the authors compare their experimental structure factors and the pair distribution functions of liquid sulfur below and above the λ-transition with the respective functions simulated with two available theoretical models based on S_8 rings [80], and on a packed structure of S_8 rings and polymeric chains [81]. From this comparison, the authors of [76] conclude that such simple models do not agree satisfactory with the experimental data. They propose an alternative picture of liquid sulfur consisting of roughly spherical molecular units. They hypothesize that the difference below and above the λ-transition temperature might be only due to different sizes of the structural units, and perhaps changes in their internal motion. However, no comparison between this model, and the experimental data has been reported.

Recent studies on the thermodynamic character of the λ-transition in liquid sulfur have been made by Jones and Ballone [78] who studied the polymerization phenomenon by density functional calculations and Monte Carlo simulations. Their simulations suggest that, above the λ-transition, the sulfur polymer coexists, at all temperatures, with a significant population of S_8 molecules, whose relative weight increases rapidly with decreasing temperature. This study is limited to the temperature range 177-577^{o}C, i.e. above the λ-transition. In this whole temperature range, calculation match the picture resulting from previous diffraction experimental data [74, 75].

Results analogous to those obtained with diffraction [71–77] are also obtained in recent in-situ Raman spectroscopy measurements on liquid sulfur [82–84]. The Raman spectra of the liquid as a function of temperature, indicates the appearance of a

polymeric fraction in correspondence to the λ-transition.

Comparing the results on liquid sulfur available in the literature, obtained with different techniques, Steudel [21] concludes that there is no indication for the presence of polymer chains below the λ-transition. The analysis of quenched samples from the melt suggests also that above the melting temperature a small percentage of the liquid is formed by S_6 and S_7 ring molecules and this percentage increases with temperature [21]. Traces of S_6 and S_7 in the liquids might activate and catalyze the λ-transition. In fact, a small amount of S_6 added to the liquid below 159^{o}C accelerates the polymerization [85]. However, S_6 and S_7 fractions in the liquid result to be small (about 5%).

A large number of *in situ* and *ex situ* studies have been conducted on the λ-transition of sulfur furnishing a rich database of information. In the present section we have briefly summarized the main results obtained by X-ray and neutron diffraction [71–77] and Raman spectroscopy [82–84] conducted *in situ*. However, a complete and detailed review on the results on liquid sulfur obtained with different experimental techniques and calculations has been recently published by Steudel [21].

The process of polymerization in liquid sulfur at ambient T can be summarized as follow:

- The liquid below the λ-transition is mostly composed of S_8 rings;

- At 159^{o}C a small fraction of the S_8 rings breaks, recombining in long polymeric chains;

- Above 159^{o}C the polymer fraction and the average length of the chains increase with the temperature. At around 200^{o}C, the relative concentration of the polymer stabilizes at almost half of the liquid composition while around 185 ^{o}C the length of the chains reaches its maximum value and starts to decrease continuously above this temperature.

This schematic description represents the state-of-the-art of our knowledge on the structural changes that take place in liquid sulfur at ambient pressure.

Despite no structural studies have been performed at higher pressures, several optical and electrical anomalies have been observed in the compressed liquid [3–5]. These anomalies may suggest the presence of further structural transitions in the liquid taking place at high pressure.

Part II

Experimental methods

Résumé du chapitre 3

La possibilité de réaliser des expériences in situ á haute température et haute pression est relativement récente. Elle doit beaucoup au développement de dispositifs efficaces permettant des mesures de diffusion á haute pression, enclume diamant, (DAC pour Diamond Anvil Cell) et presse á grand volume, (LVP pour Large Volume Press). Le principe de la production de hautes pressions en DAC est simple : une force est appliquée sur la base d'un diamant taillé en brillant puis transmise sur une face polie opposée de faible surface. L'enclume haute pression est faite de deux de ces diamants placés en opposition, l'un fixe et l'autre soumis á la force appliquée. L'échantillon est placé dans une cellule entre les deux petites faces polies. Il existe deux sortes de tels dispositifs : l'un "mécanique" ou la force est appliquée par un système à vis et un autre á "membrane" ou une membrane métallique torique est gonflée par un gaz transmetteur de pression. Les cellules peuvent être chauffées par un circuit électrique ou par laser et, grce á la transparence du diamant on peut également les utiliser pour des expériences de diffraction-X ou de Raman. Dans un DAC la pression est mesurée généralement á l'aide d'un étalon de fluorescence dont on mesure le déplacement des pics. Habituellement il s'agit d'un rubis dopé au Cr^{+++} toutefois dans le cas de mesures combinant hautes températures et hautes pressions le borate de strontium dopé au samarium Sm^{+++} fournit une meilleure sensibilité.

La presse Paris-Edimbourg est basée sur une enclume de conception différente afin de permettre l'utilisation de plus gros échantillons par rapport au DAC, ce qui la rend particulièrement adaptée á l'étude des liquides sous pression. La pression est ici transmise par des enclumes de grandes dimensions en carbure de tungstène ou en diamants frittés. Le chauffage est électrique, le four étant constitué d'un cylindre de graphite qui entoure l'échantillon. La température et la pression sont déterminées généralement á partir de l'équation d'état de deux calibrants placés dans la cellule porte échantillon.

Chapter 3

High pressure techniques

In general, the best way to achieve very-high pressures is to squeeze the sample with something hard.

Conditions of extreme pressure and temperature provide a valuable tool for the study of solid and liquid polymorphism of an element. Pressure is a physical variable that can be easily applied to a small sample volume. Thanks to the development of different high pressure devices, such as diamond anvil cells and large volume presses, coupled to modern X-ray and neutron sources, changes in structural and dynamical properties of solid and liquid materials can be studied in situ.

The scope of this chapter is to describe the pressure devices used for our experiments; i.e. the diamond anvil cell and the Paris-Edinburgh press. We also introduce the pressure-temperature metrology used.

3.1 Pressure generation techniques

The large number of modern high pressure devices can be entirely traced to the principles laid out by Bridgman (Nobel prize, 1946). If pressure is applied on the base of an anvil (that can be schematized as a truncated cone), a higher pressure is generated on the tip because its area is much smaller than the area of the base. The generated pressure will be proportional to the base to tip ratio and will depend on the mechanical properties of the anvil material. Instruments based on this principle include large-volume gas media and hydro-thermal apparata (at lower pressures), as well as multi-anvil and the conventional "large volume" opposed-anvil apparata (at higher pressures). The opposed anvils devices that have evolved over the years are the basic Bridgman anvil design, the supported anvil Drickamer cell, the Troitsk toroid cell, the Paris-Edinburgh cell and the DAC [86–89]. Figure 3.1 shows a picture of the original DAC constructed by Weir at al. in 1958 [89].

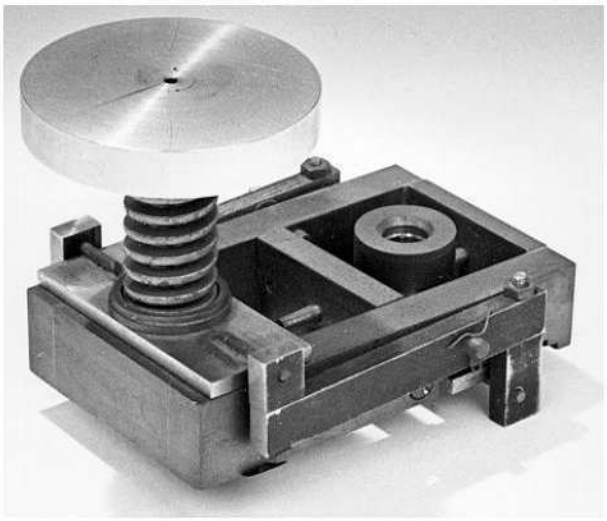

Figure 3.1: The original DAC, on display in the National Institute of Standards and Technology (NIST) Museum.

Various materials like steel, tungsten carbide, boron carbide, sapphire, cubic zirconia, sintered diamond, and single crystal diamond have been used as anvils. Their use for a specific technique and pressure ranges is related to their strength, available sizes and shapes, optical clarity, X-ray transmission, and other mechanical, thermoelectric and magnetic properties. For instance, considering an anvil base-to-top area ratio of 100, 30 GPa can be reached with tungsten carbide Bridgman anvils, 60 GPa can be reached with sintered diamond Bridgman anvils, and 140 GPa can be reached with single crystal diamond anvils.

The choice of a specific pressure device strictly depends on the measurements to carry out: despite highest pressures can be reached with DAC cells, often many macroscopic diagnostic techniques require sample sizes beyond those provided by DACs. In these cases, large volume pressure devices, such as the Paris-Edinburgh press, are more suited.

3.2 Diamond anvil cell

The diamond anvil cell (DAC) is currently the device that reaches the highest conditions of pressure: single crystal diamonds, the hardest material known, allow for the attainment of pressures far greater than any other material (300 GPa at ambient temperature). A picture of a diamond anvil cell is shown in figure 3.2.

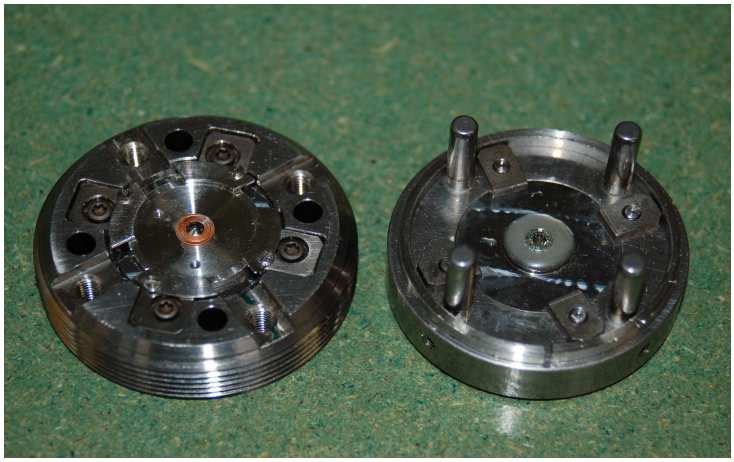

Figure 3.2: A DAC cell.

The cell is composed of two monocrystalline diamonds with a brilliant-like shape and with flat polished heads (see fig.3.3). The diameter of these surfaces ranges from

10 μm to 600 μm in order to reach pressures from 20 GPa to 300 GPa.

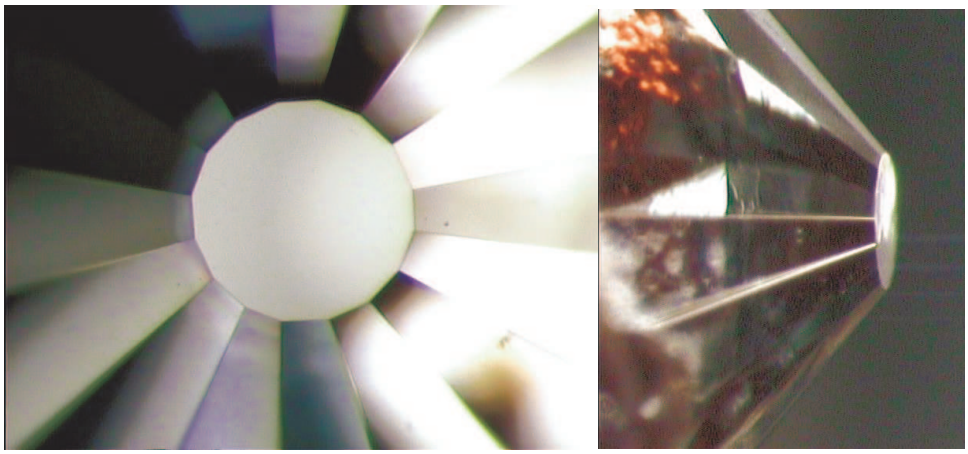

Figure 3.3: Top and side view of the diamond anvil.

The sample is confined between the two flat faces of the diamonds within a metallic gasket, through which a hole has been drilled (see figure 3.4 [90]) by electro-erosion techniques.

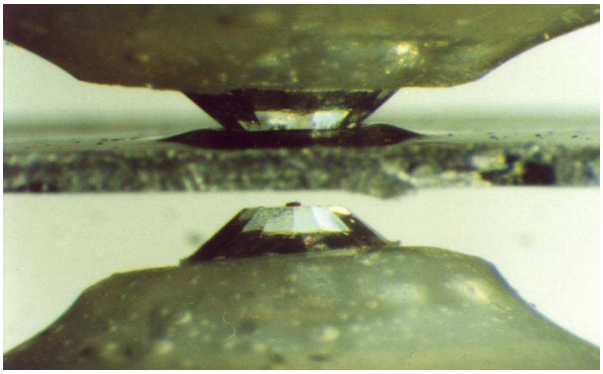

Figure 3.4: Metallic gasket between the diamond anvils.

When applying a force on the back of one of the diamonds, the other one being fixed to the cell, compression is applied. The deformation of the metallic gasket, when using a soft pressure transmitting medium, can create quasi-hydrostatic conditions to pressures exceeding 100 GPa.

The simple mechanical principle of DACs allows many convenient configurations depending on the experiment to be carried on.

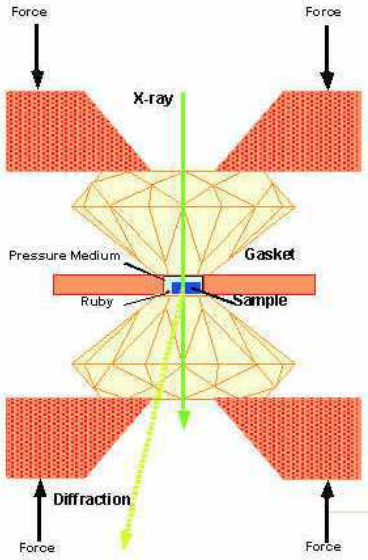

Figure 3.5: Basic principle of a DAC.

However there are two important kinds of DACs: those that are mechanically driven and those driven by membranes [91]. Membrane DACs have been used for the experiments reported in this thesis (a detailed description will be given in the next paragraph). The main advantage in the use of a membrane DAC is the possibility to change the pressure on the sample without removing the cell from the diffractometer and as a consequence without realignments.

The importance of DACs in high pressure research is due not only to their mechanical characteristics, but also to their optical properties. Diamond is ideal for *in situ* X-ray diffraction experiments on samples held at high pressure. Because carbon is a light element, diamond anvils are essentially transparent above 10-12 keV (assuming normal thicknesses of 2-2.5 mm each). Furthermore, diamond has a simple crystal structure with a small unit cell, so that its diffraction pattern is simple and easily identified. In any case, the diamond anvils are single crystals, and so their diffraction leads to few well-defined spots within the Laue zone that are easily identified in angle-dispersive experiments.

When carrying out optical experiments such as Raman scattering, it is important to carefully choose diamonds that do not give rise to strong fluorescence that would provide a strong baseline signal that might overwhelm the weak inelastic light scattering spectra. Natural diamonds exist in a wide variety of colors, the most common colors ranges

from perfectly colorless to light yellow or brownish. A lettering system from D to Z is used to identify the color of diamonds, with D awarded only to rare, totally colorless diamonds. Stones with color grades D or E, with low fluorescence, are suitable for Raman scattering experiments. A good "Raman" diamond should have a background that is flat. Synthetic diamonds are now available that are essentially impurity-free, with little or no observable fluorescence. Such diamonds are still difficult to obtain and are expensive however.

3.2.1 Generating high pressures and temperatures

Membrane DACs were first proposed by William Daniels around 1980. This stimulated Letoullec and collaborators [92], who constructed the first DAC in 1988. Its design was consequently modified to adapt the device to different experimental techniques.

Membrane DACs use a metallic toroidal membrane often inflated with helium to exert pressure on a piston. Axial forces are generated, which are therefore homogeneously extended over all the piston, thereby permitting a precise control of the pressure. The membrane is linked by a metallic capillary to a helium bottle through a pressure controller. A picture of a membrane DAC and its pressure controller is shown in figure 3.6.

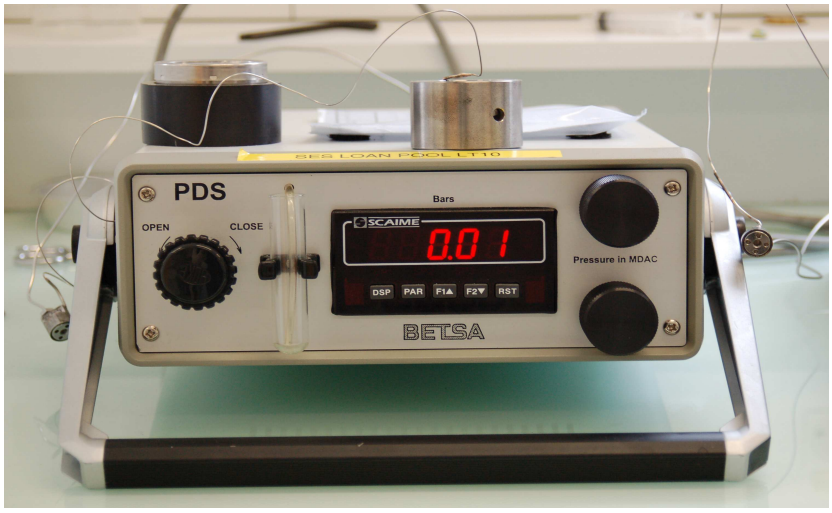

Figure 3.6: Membrane DAC and its pressure controller.

By using a membrane DAC, pressure on the sample can be easily tuned without

touching or displacing the cell. In this way time consuming realignment of the cell is reduced, which is specially important when working with small samples, as these need an accurate centering on the beam path in order to avoid parasitic diffraction from the sample environment.

The external electrical heating method has been used for all the experiments presented in this thesis [93]. A cylindrical heater is placed around the cell. Resistive heating allows to generate temperatures in a wide range (from 300 K to over 1500 K), which are easy to measure with thermocouples, and which can be maintained at constant value (±3 K) for several hours. Moreover in externally heated DAC at temperatures higher than 800 K pressure gradients are practically absent and the heating is very homogeneous.

However, with external heating many problems arise: oxidation and graphitization of the diamonds, rapid creep deformation of materials, welding of the gasket to the anvils, etc. Although conducting experiments at constant temperature with resistively heated DACs is relatively easy, maintaining constant pressure during heating is a problem. Differences in the thermal expansivity of diamonds, seats, and various mechanical parts of the cell often lead to significant variations in the pressure.

3.2.2 Measuring high pressures

A precise, fast and easy way to measure the pressure on the sample is to introduce a luminescent compound into the DAC. Forman *et al.* [94] were the first ones to propose the use of a small ruby crystal doped with Cr^{+++} in 1972. Ruby has since become a pressure standard in high pressure experiments.

Cr^{+++}-doped ruby shows two intense luminescence peaks, R_1 and R_2 (at 6942.48 and 6927.0 Å, respectively, at ambient conditions). The shift of R_1 with pressure has been calibrated several times [95–99]. It is linear up to about 20 GPa. The shift of the R_1 and R_2 peaks from 0 to 10 GPa at room temperature is shown in figure 3.7.

For higher pressures it can be calculated from the expression proposed by Mao *et al.* [99]:

$$P = \frac{0.274\lambda_{R1}(0)}{B}\,[(\frac{\lambda_{R1}(P)}{\lambda_{R1}(0)})^B - 1]$$

where B is a parameter related to the degree of hydrostaticity on the sample: $B = 5$ for non-hydrostatic conditions and $B = 7.665$ for conditions close to hydrostaticity.

As the pressure increases both components of the R_1, R_2 doublet broaden until there is a complete overlap at a pressure which depends on the quality of the hydrostatic conditions on the sample. The signal to noise ratio decreases with increasing pressure,

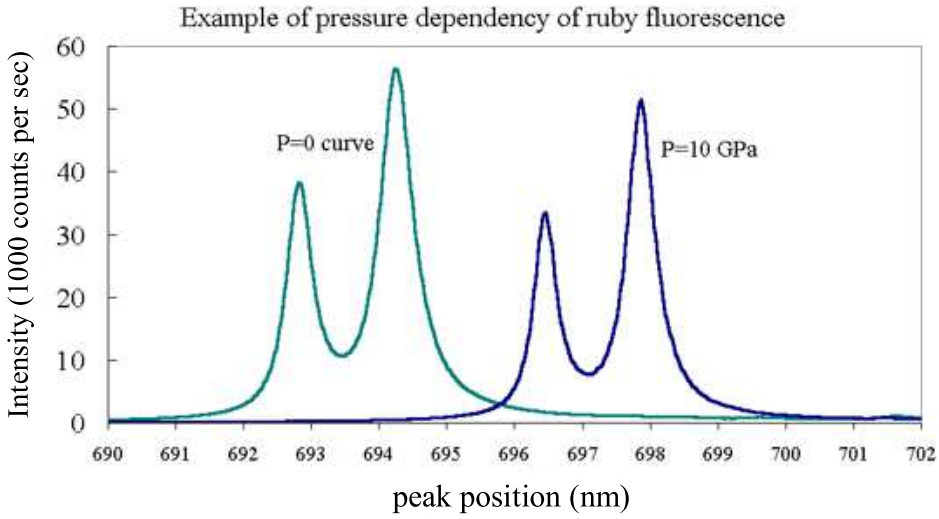

Figure 3.7: Example of pressure dependence of ruby fluorescence.

which makes precise high pressure measurement more difficult. The position of the R_1 peak is also dependent on temperature [100]. The same effects (widening of the peaks and lowering of the signal to noise ratio) are observed at high temperatures.

When high pressure and high temperatures are combined, there are other compounds that are more appropriate, one of them is strontium borate doped with samarium, SrB_4O_7:Sm^{++} [100]. In alternative, sometimes, the pressure transmitting medium can be used also as internal standard using *in situ* X-ray diffraction (this can be done, for example, with NaCl, KCl or MgO).

3.3 Paris-Edinburgh Press

The Paris-Edinburgh (P-E) press is a large volume device which was initially designed for high pressure neutron diffraction studies [101] being later adapted to synchrotron X-ray diffraction experiments [102]. A picture of the ID30/ID27 Paris-Edinburgh press is shown in figure 3.8.

This cell employs an opposed anvil design [103] and allows a sample volume as high as 80 mm^3. Its most characteristic features are the anvil design and the compact hydraulic ram which makes *in situ* variations of the sample pressure possible. Its principal advantage are:

Figure 3.8: Picture of the ID27 Paris-Edinburgh press.

Lightness: The press has a mass of 50 kg, and so it is easy to handle. For comparison the multi-anvil system MAX 80, with similar performance, has a mass of about 1.5 Ton weight, and the new press at DESY is 28 Ton.

Small size: Its dimensions are 200 x 200 x 200 mm^3 which enormously eases its installation at experimental facilities.

Fast installation: A complete installation of the device can be achieved in few hours, an important point in large facilities.

The mechanics of the press are relatively simple. fig.3.9 shows its different elements. The force is generated by an hydraulic jack.

An hydraulic pressure is exerted on a piston by means of an hand pump, up to 280 MPa capacity which is connected to the press by a flexible tube. The force is transmitted to two opposed anvils by means of two tungsten carbide (WC) or sintered diamond (SD) seats. The high pressure cavity lies between the two anvils and the ratio of its surfaces to those of the piston's is approximatively 0.01, that is to say, the hydraulic pressure is increased by a factor of 100 at the sample chamber. Much work was invested in

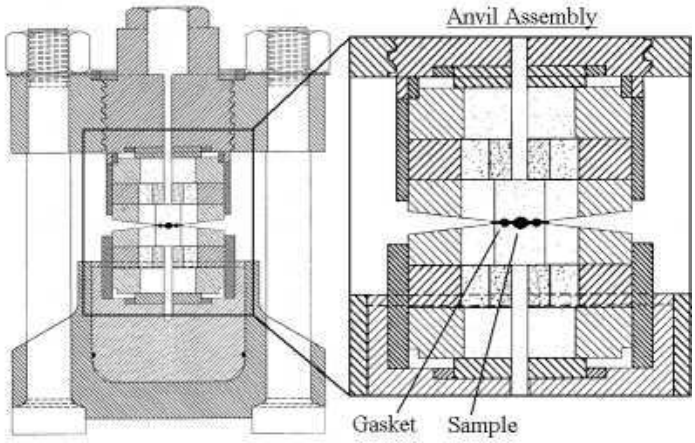

Figure 3.9: Scheme of a Paris-Edinburgh press and its components. The press is shown at left while the inset at right shows the anvil assembly where the sample is placed.

the design of the anvils; their shape is shown in figure 3.10 together with the sample environment.

The anvils are composed of a WC or SD core embedded in a ring of hardened steel, which increases much the mechanical resistance. The profile of the anvils is obtained by electro-erosion. The exact shape of the anvils has a crucial importance which must satisfy the following requirements:

- The generation of conditions that are as close as possible to hydrostaticity;
- The minimization of the deformation of the gasket located between the anvils, in order to keep open the access to the sample for the X-rays;
- The minimization of the radial deformation of the gasket in order to prevent thermocouple breakage;

In addition to the anvil shape, the pressure transmitting gasket also plays a crucial role in the optimization of the experimental conditions. It supports the mechanical stresses imposed by the anvils and thus, it has to be mechanically very resistant. For *in situ* experiments with X-rays, it is required that the gasket be composed of a light material, in order to minimize absorption. In addition, it must be a good thermal insulator for use in high temperature experiments. Several materials were tested, and the best compromise was obtained with amorphous boron. It is a light material (Z=5),

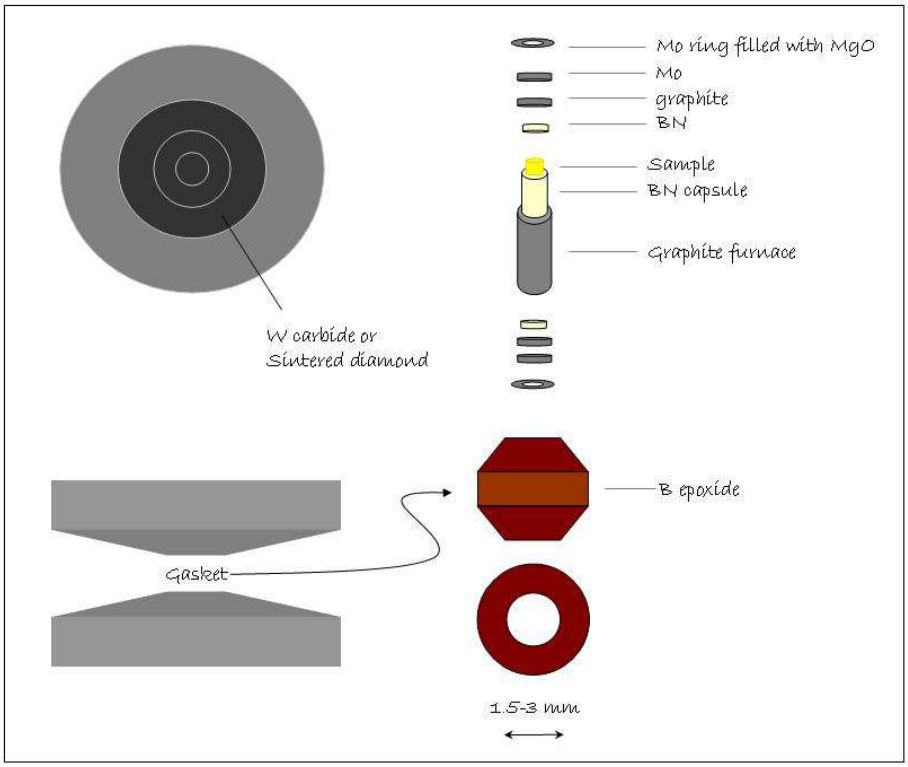

Figure 3.10: Anvils and sample environment for the Paris-Edinburgh press.

thus it only absorbs X-rays to a small extent. Its thermal conductivity is also very low (c=2.65 W/mk^{-}1 at 300K) which permits a good thermal insulation.

In order to make the gaskets, amorphous boron is mixed up with an epoxy resin (mass ratio 4:1). The resin is then polymerized and compacted. It gets its final shape (figure 3.10) after machining with WC tools. The sample assembly is held between two supported WC anvils with an opening angle of 15^o in the vertical direction and a quasi-conical profile. This ensures quasi-hydrostatic conditions. The powder sample of 2 mm height and 0.8 diameter is encapsulated in a hexagonal BN (hBN) cylinder which acts as a pressure transmitting medium, pressure standard and thermal insulator. Temperatures up to 2300 K are generated resistively by a graphite heater placed between the anvils that also act as electrodes. The top and the bottom of the furnace are closed by two graphite disks. A disk of molybdenum and a stainless steel ring filled with MgO are also placed at the top and at the bottom in order to guaranty good electrical

contacts.

3.3.1 Generating high temperatures

Most of the elements inside the boron-epoxy gasket assembly for Paris-Edinburgh press are present to ensure the proper heating of the sample. The aim is to conduct the electrical power from a power supply to the high resistivity graphite heater (stainless steel rings and molybdenum disks), and to thermally insulate the sample (hBN capsule). This assembly permits temperatures up to 2300 K to be achieved.

A slightly different assembly uses a thermocouple to measure the sample temperature. For this, a hole must be drilled through the gasket and close to the sample. The thermocouple sheath is surrounded by a protective ceramic sheath in order to be well isolated. This means that the diameter of the gasket hole must be relatively large, which gives raise to numerous drawbacks. Considerable quantities of both the gasket and the sample must be displaced, thus imperfections are introduced into the furnace and the capsule materials. The consequences of this are a reduced mechanical performance of the gasket around the intrusion, an increase of the risk of the furnace rupture, and the possibility of non-uniform thermal gradients. Some samples directly preclude the arrangement for the thermocouple, as it happens in the experiments on liquids or on high reactive samples; the first ones because they would escape from the sample holder through the hole; the latter ones because they would react with the material of the thermocouple with its consequent damage and, the contamination of the sample environment. This geometry also affects the extent of thermal insulation and restrict the ability to reach high pressures, due to the outside diameter of the thermocouple sheath, which is of the order of the gap between the anvils [104].

3.3.2 Measuring high pressures and temperatures

When a thermocouple is used the only variable still to be measured is the pressure. The sample environment is opaque in the Paris-Edinburgh press, so the ruby fluorescence method cannot be used. The most effective way is to use compounds whose equation of state (EoS) is well known, by calculating the variation of the cell dimensions from a diffraction pattern it is possible to determine the pressure or temperature conditions. Four important requisites must be respected:

- *The EoS (p,V,T) of the compound must be well known in the thermodynamic regime of interest;*

- *The compound has to be compressible enough as to allow a precise determination of the pressure;*

- *No phase transitions must take place in the (p,T) range in which the experiment is carried on;*

- *The gauge must not react chemically with the sample;*

In addition, it is preferable that the compound has a simple diffraction pattern (high symmetry, small cell), so that it will not interfere with the diffraction from the sample. NaCl [105, 106] and Au [107] are the most commonly used internal pressure standards. In our experiments, hBN is the primary material in the capsule, and it is used as well as the pressure standard following the recent EoS determination by Le Godec *et al.* [108]. For each p,T point investigated, a diffraction pattern of hBN is taken by slightly displacing the press.

Obviously, an internal standard allows to calibrate only one of the two p,T variables, so that the other one must be known. Because of the many inconveniences and physical limitations in the use of thermocouples discussed in the previous section, a non-invasive procedure has been recently developed for the determination of pressure and temperature in the Paris-Edinburgh press [104]. It consists of measuring the volume variations of two internal standards, whose the EoS are known. Ideally the materials chosen have well-determined and contrasting thermoelastic properties. Good choices could be Au/NCl or hBN/Pt couples. It is important to choose materials whose Bragg peaks used for the determination of the volume variation do not overlap. With this method, the estimation of the point of intersection in the p,T space is simple and precise; comparison between cross-calibrated p,T and an hBN internal standard give deviations of 0.2 GPa and 13% of the true values [104]. In addition, by considering the X-ray spot size, of approximately 30x20μm^2, the effects of p and T gradients are much reduced. This method uses only the thermoelastic properties of well-characterized materials, and as such, is theoretically limited by the ability to obtain precise unit cell volumes from good quality diffraction patterns.

Résumé du chapitre 4

L'utilisation des dispositifs haute pression décrits au chapitre précédant sur une source de brillance très élevée a permis la réalisation d'expériences de diffraction a haute pression. Cette brillance élevée était également nécessaire pour réaliser les mesures de diffusion inélastiques. Les lignes de lumière de la source de rayonnement synchrotron de l'ESRF constituent un outil idéal pour de telles études.

Par sa longueur d'onde du même ordre de grandeur que les distances inter-atomiques dans la matière condensée le rayonnement X est une technique très bien adaptée a la détermination de la structure. Les diagrammes de diffraction X obtenus permettent la détermination des paramètres du réseau cristallin. Les résultats décrits dans ce manuscrit ont été obtenus sur la ligne haute pression de l'ESRF (ID30/ID27) destinée á l'étude structurale de la matière sous conditions extrêmes. Son équipement haute pression est constitue de plusieurs DAC et d'une presse Paris-Edimbourg pouvant être utilises en EDX ou ADX.

Les expériences de diffusion inélastique sur le liquide ont été réalises sur la ligne ID16 de l'ESRF. Il s'agit d'un spectromètre trois axes : le premier axe étant celui du cristal monochromateur qui définit l'énergie des rayons-X du faisceau incident. Le second est celui de l'échantillon qui diffuse ce faisceau et change son énergie. Le troisième est celui du cristal analyseur qui définit, pour un vecteur de diffusion donne, le transfert d'énergie. Compte tenu de l'énergie élevée du rayonnement X et des faibles transferts d'énergie a mesurer (phonons dans la gamme de 1 a 10meV), les balayages en énergie tant du monochromateur que de l'analyseur sont réalisés en changeant leur paramètre de réseau par variation de leur température.

L'effet Raman correspond á la diffusion inélastique de la lumière visible par la matière. La gamme d'énergie concertiste permet de caractériser les vibrations de haute énergie du réseau mais aussi les modes internes de systèmes moléculaires. L'emploi d'un laser a bande étroite permet une bonne séparation des modes en fréquence et en particulier, a basse énergie, la séparation de la diffusion Rayleigh (élastique).

Chapter 4

X-ray and Raman techniques

Synchrotron radiation is the electromagnetic radiation emitted by electrons or positrons moving at relativistic velocities along a curved trajectory with a large radius of curvature

ESRF team, foundation phase (1988)

4.1 Introduction

High pressure and temperature diffraction experiments can only be performed if an extremely bright radiation is used. This is due specifically to the small size of the sample, which imposes the use of a highly collimated and extremely brilliant beam. The high pressure devices used to generate high pressure and temperature confine the sample in an environment that absorbs many of the incident photons. Therefore, these experiments are very difficult, if not impossible, to perform with conventional X-ray sources. With the construction of third generation synchrotrons it is now possible to perform very precise measurements under extreme p,T conditions.

The unique properties of third generation sources make inelastic X-ray scattering an excellent technique to perform dynamics studies, complementing, and often overcoming classic inelastic neutron scattering.

In this chapter, after an introduction to the main characteristic of synchrotron radiation and to the European Synchrotron Radiation Facility (ESRF), we will successively describe:

- *The principles of X-ray diffraction (XRD) and the characteristics of the ID30, ID27 beamlines at ESRF;*

- *The theory of inelastic X-ray scattering (IXS) and the characteristics of the ID16 beamline at ESRF;*

- *The principles of Raman spectroscopy and some related experimental details.*

In our study Raman spectroscopy has proven to be an excellent technique to be used to complement X-ray diffraction.

4.2 Synchrotron radiation

Synchrotron radiation is widely used in physics, chemistry, biology, and medical science due to its unique characteristics, particularly its spectral distribution. A typical electron accelerator emits synchrotron radiation in a very broad range of photon energies, from microwaves to hard X-rays and γ-rays, that is, from a few electronvolts to 10^5 eV. Thus, it provides electromagnetic radiation in spectral regions for which no comparable sources exist, for example most of the ultraviolet/soft-X-ray range. In addition, it is the best source of hard X-rays, even though other sources exist for this range. Within this wide range, the wavelengths range from 10^3 to 10^{-1} $\mathring{A}$. This is of the order of the sizes of the atoms and molecules, the lengths of chemical bonds and the minimum distances between atomic planes in the crystals. Thus, the photons provided by this sources have the right wavelengths for studying the atomic structure of solids, liquid and important biological structures. With these photons it is also possible to study the properties of valence and core electrons as well as of the electrons engaged in chemical bonds. The knowledge of the electronic properties of atoms, molecules, solids and biological systems is the key to understand most of their physical and chemical properties. The major stimulating factor in the early steps of synchrotron radiation research was its spectral distribution.

There were, however, other important factors, especially the intensity delivered by a synchrotron radiation source, the small size of the source, and the high degree of collimation of the radiation in a narrow cone around the trajectory of the electrons. These characteristics make it possible to concentrate high intensity in a small area, as it is required by many experiments.

One of the major problem of early synchrotron was the pulsed character of the radiation they produce, due to the rapid decay of the accelerated electron beam. In modern storage rings, instead, the accelerated electrons can be stored and circulate in a closed orbit for several hours. The beam decay is so slow that the source intensity can be considered as nearly constant over time for most of the experiments. Strictly

speaking, however, even the radiation emitted by a storage ring is not continuous, but is pulsed, due to the fact that the stored electrons circulate in bunches.

An important parameter that eases the characterization and comparison of synchrotron radiation sources is the *brilliance*, which is the number of photons emitted per unit source size, per unit solid angle, per unit time, within an unit spectral bandwidth (typically 1/1000 of the photon energy). As one can appreciate from the definition, brilliance puts a premium not only on the photon flux (photons per second in a given bandwidth), but also on the high phase space density of the photons, i.e. on being radiated out of a small area and with high directional collimation. Since 1960, the brilliance of available synchrotron sources has been growing at a formidable pace in the last decades (see figure 4.1).

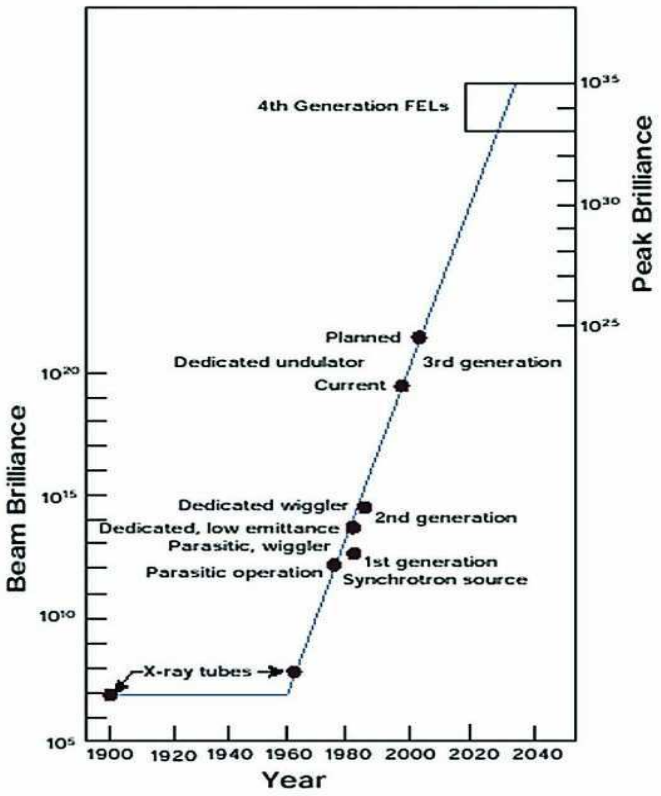

Figure 4.1: Historical evolution of the brilliance of 8 keV x-ray sources, extrapolated into the future. The left scale represents the average brilliance (averaged over the pulsed structure of the synchrotron beams), the right scale refers to the peak brilliance (at the top of one pulse) [109].

The X-ray measurements reported in this thesis have been performed at ESRF, that is classified as a "third generation" synchrotron. This class of sources is characterized by a reduced emittance (i.e. reduced phase space volume) of the circulating particle beam, and by the extensive use of undulators as radiation sources, with a further increase of the brilliance by several orders of magnitude. The specific characteristic of the ESRF will be described in the next paragraph.

4.2.1 The ESRF

The European Synchrotron Radiation Facility (ESRF, figure 4.2), is a research center created in 1986 and initially funded by twelve European countries: France, Germany, Italy, United Kingdom, Spain, Switzerland, Benesync (Belgium, Netherlands), and Nordsync (Denmark, Finland, Norway, Sweden). Since then, six more countries have joined the group: Portugal, Israel, Austria, Poland, Czech Republic and Hungary. The aim is the operation of a synchrotron radiation facility for external users, preferably belonging to the participating countries, though it is opened to any valuable scientific project coming from any country. The ESRF is the first *third generation* facility, that is, the first synchrotron radiation facility dedicated to the production of hard-X-rays (very high energy beams) of high brilliance. The X-ray beams at ESRF are about a trillion times brighter (i.e. a factor of 10^{12}) that those of conventional X-ray sources used in laboratories.

Figure 4.2: Photograph of the ESRF [110].

The peculiarities of the radiation of the ESRF come from the characteristic of the machine, constituted of three accelerators (see figure 4.3):

- A 16m long linear accelerator, LINAC, that takes electrons to an energy of 200 MeV.

- An acceleration ring, BOOSTER, with 300 m in circumference. It repeatedly accelerates the electron bunches emitted from the LINAC in order to provide them with the operating energy of 6 GeV. At that moment, the bunches are injected in the storage ring.

- The Storage Ring, with 844 m in circumference, where the electron beam is maintained at the operating energy. Here, the electrons traveling with nearly the speed of light, emit synchrotron radiation.

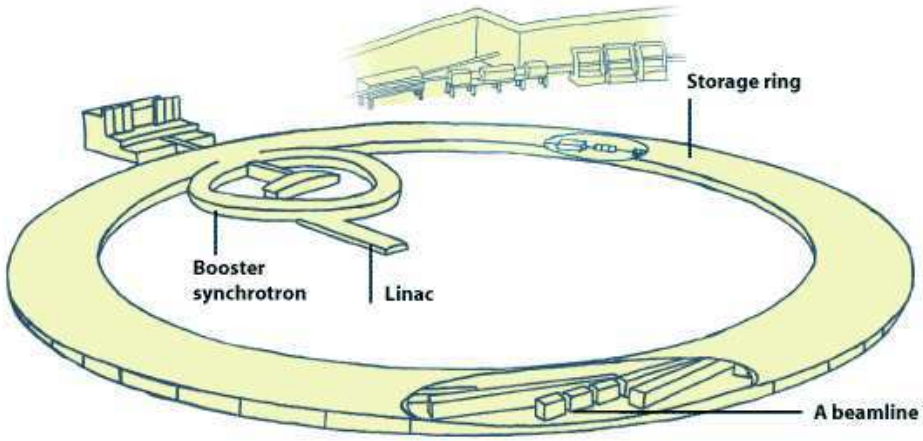

Figure 4.3: Schematic view of the ESRF. The location of the accelerators is indicated. [110].

In the storage ring, the radiation sources (insertion devices IDs, and bending magnets BMs), as well as the first sections of the beamlines (*front ends*) are installed. A radiation source consists of a periodic array of magnets which modify the trajectory of the electrons in straight sections of the ring. This modification of the trajectory from a straight line results in the emission of synchrotron radiation with the characteristics already mentioned (fig. 4.4).

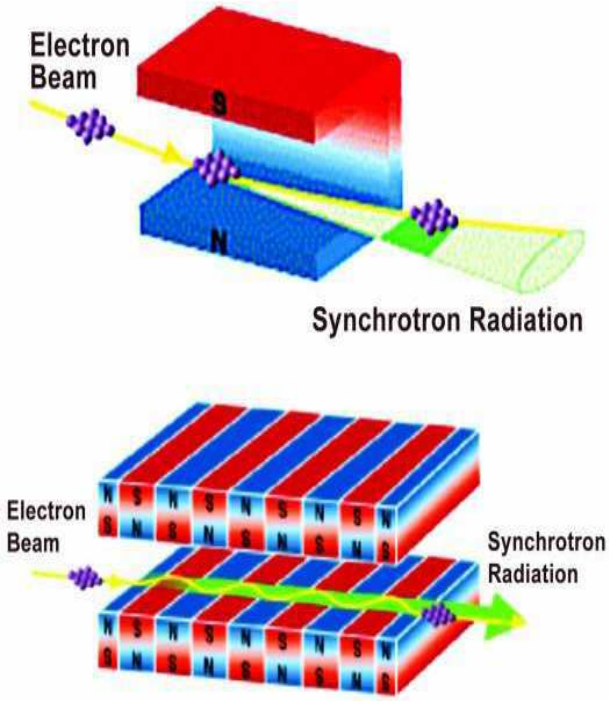

Figure 4.4: (Top) Schematic view of the generation of synchrotron radiation in a dipole bending magnet, where electron bunches are deviated to follow the orbit around the ring. (Bottom) Generation of synchrotron radiation in an insertion device, where the upper and lower magnet arrays produce vertical fields forcing the electrons to follow a zig-zag trajectory [109].

The storage ring is formed by 32 sectors with an analogue magnet structure. Each of them represents two straight sections of different length, only one being long enough to allocate an ID. These straight sections are connected by two different BMs which alternate along the circumference of the ring. The presence of the bending magnets just after the insertion devices serves to deviate the electron bunches, thus allowing the radiation generated to escape the insertion device. Additional BMs are exclusively used for the generation of the radiation. Thus it is possible to extract two useful beams from each sector, one from the insertion device ID, and one from the bending magnet (BM or D). In its normal mode of operation, the ESRF storage ring provides a current of 200 mA for a lifetime of about 50 h. Energy losses of the electron beam are compensated by six accelerating cavities, operating at frequency of 352 MHz.

4.3 X-ray diffraction

The wavelengths of the X-ray radiation are comparable to the interatomic distances characteristic of the condensed matter. It can elastically interact with the matter, giving rise to diffraction patterns that allow the reconstruction of the map of the atomic positions.

In 1912, Max van Laue found that X-rays that struck the surface of a crystal were diffracted into patterns that resembled the patterns produced when light passes through a very narrow slit. For that discovery, he received the 1914 Nobel Prize in Physics. In 1913 the English physicists Sir W.H. Bragg and his son Sir W.L. Bragg derived a simple law in order to explain this phenomenon. The cleavage faces of crystals reflect an X-ray beam at certain angles of incidence (θ), following the simple equation:

$$n\lambda = 2dsin\theta \tag{4.1}$$

where the variable d is the distance between atomic layers in a crystal, λ is the wavelength of the incident X-ray beam, and n is an integer.

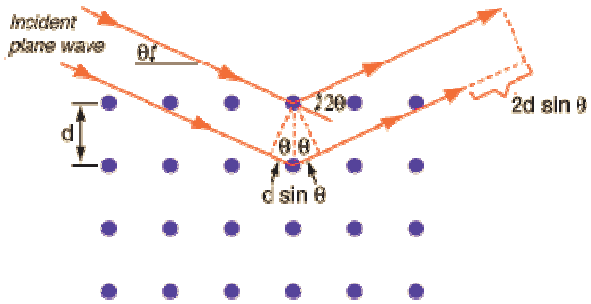

When X-rays are scattered from a crystal lattice, peaks of scattered intensity are observed which correspond to the following conditions:

1. The angle of incidence = angle of scattering.

2. The pathlength difference is equal to an integer number of wavelengths.

W.H. and W.L. Bragg were awarded the Nobel Prize in physics in 1915 for their work in determining crystal structures; beginning with NaCl, ZnS and diamond. Although Bragg's law was used to explain the interference pattern of X-rays scattered by crystals, diffraction has been developed to study the structure of all states of matter with any

beam, e.g., ions, electrons, neutrons, and protons, with a wavelength similar to the distance between the atomic or molecular structures of interest.

The Bragg's law can be derived by simple considerations on the periodicity of the crystalline structure and the form of the incident and diffracted waves. In the approximation that the X-ray source is so far that the incident waves can be considered planes [111], the amplitude diffused by a solid of volume V can be written as:

$$A = \int_V dV\, \rho_e(r)\, e^{(-2i\pi(\mathbf{k}-\mathbf{k'})\cdot\mathbf{r})} \tag{4.2}$$

$\rho_e(r)$ represents the local electron density and **k** and **k'** are the wave vectors of the incident and diffused radiation.

In a crystal the atoms are periodically arranged, so that each atomic position can be reconstructed from one origin by the translation vector $\mathbf{T} = u\mathbf{a} + v\mathbf{b} + w\mathbf{c}$ (where u, v, w are integer numbers and $\mathbf{a}, \mathbf{b}, \mathbf{c}$ are vectors that for $u = v = w = 1$ define the unit cell of the crystalline lattice). If we consider the atoms as punctiform, and each point characterized by an electron density ρ_e, the electron density map $\rho_e(r)$, can be described as:

$$\rho_e(r) = \sum_{\mathbf{h}} \rho_{e,\mathbf{h}}\, e^{(2i\pi\mathbf{h}\cdot\mathbf{r})} \tag{4.3}$$

where $\mathbf{h} = h\mathbf{a}^* + k\mathbf{b}^* + l\mathbf{c}^*$ and h, k, l are integer. The vectors $\mathbf{a}^*, \mathbf{b}^*, \mathbf{c}^*$ constitute the base of the reciprocal lattice defined as:

$$\begin{cases} \mathbf{a}^* = & \frac{1}{2\pi v}\, \mathbf{b} \times \mathbf{c} \\ \mathbf{b}^* = & \frac{1}{2\pi v}\, \mathbf{c} \times \mathbf{a} \\ \mathbf{c}^* = & \frac{1}{2\pi v}\, \mathbf{a} \times \mathbf{b} \end{cases}$$

v is the volume of the parallelepiped formed by the vectors $\mathbf{a}, \mathbf{b}, \mathbf{c}$; $v = |\mathbf{a} \cdot (\mathbf{b} \times \mathbf{c})|$. The vector **h** connects two nodes of the reciprocal lattice. Considering that for an elastic process ($|\mathbf{k}| = |\mathbf{k'}|$), and combining eq. 4.2 with the eq. 4.3 we obtain:

$$2\mathbf{k} \cdot \mathbf{h} = |\mathbf{h}^2| \tag{4.4}$$

that is the vectorial form of the Bragg's law.

The Bragg's law allows to determine the structure of the unit cell through the determination of the distance d between the lattice planes and their relative position. This information, anyway, does not allow to know the space group, i.e. the symmetrical relationship between like atoms in the unit cell. This problem can be solved by looking

at the relative intensity of the peaks. For a Bragg's reflection, the diffracted wave amplitude is expressed as:

$$F_{hkl} = \sum_i f_{at,i}(\mathbf{h})\, e^{(-2i\pi \mathbf{h}\cdot\mathbf{r}_i)} \tag{4.5}$$

the term $f_{at,i}$ indicates the *atomic form factor*:

$$f_{at,i}(\mathbf{Q}) = \int_{V_{at}} dV\, \rho_e(r)\, e^{(-2i\pi \mathbf{Q}\cdot\mathbf{r}_i)} \tag{4.6}$$

where $Q = \mathbf{k} - \mathbf{k'}$ is the momentum. if we indicate with I the diffracted intensity, then $I \propto |F|^2$ and considering that $f_{at,i} = Z$ when $k = 0$, the intensity of the diffraction lines will be proportional to Z^2. The term F_{hkl}, called *Structure Factor*, contains the information relative to the atomic positions. Considering that the Bragg's law involves at the same time the wavelength and the diffraction angle, two different modalities can be adopted to measure diffraction patterns: the Angle dispersive X-ray diffraction (ADX) and the Energy dispersive X-ray diffraction (EDX). In the case of ADX the wavelength of the experiment is fixed and the diffraction pattern is taken by varying the diffraction angle. In the case of EDX the diffraction angle is fixed and the spectra are measured by varying the wavelength. The diffraction data presented in this thesis are angle dispersive, starting from powdered samples.

4.3.1 Powder diffraction

Powder X-ray diffraction (PXRD) is a widely used diffraction technique for characterizing materials. As the name suggests, the sample is in a powdery form, consisting of fine grains of the single crystalline material to be studied. The technique is used also widely for studying particles in liquid suspensions or polycrystalline solids (bulk or thin film materials).

The term 'powder' means that the crystalline domains are randomly oriented in the sample. Therefore when the 2-D diffraction pattern is recorded, it shows concentric rings of peaks corresponding to their 2θ position (see figure 4.5). The positions and the intensities of the peaks are used for identifying the underlying structure (or phase) of the material.

In this thesis, the diffraction patterns from powdered (but also liquid) samples are measured in transmission and collected by using the image plate two-dimensional detector (Mar345). By knowing the wavelength, the exact sample-detector distance, the

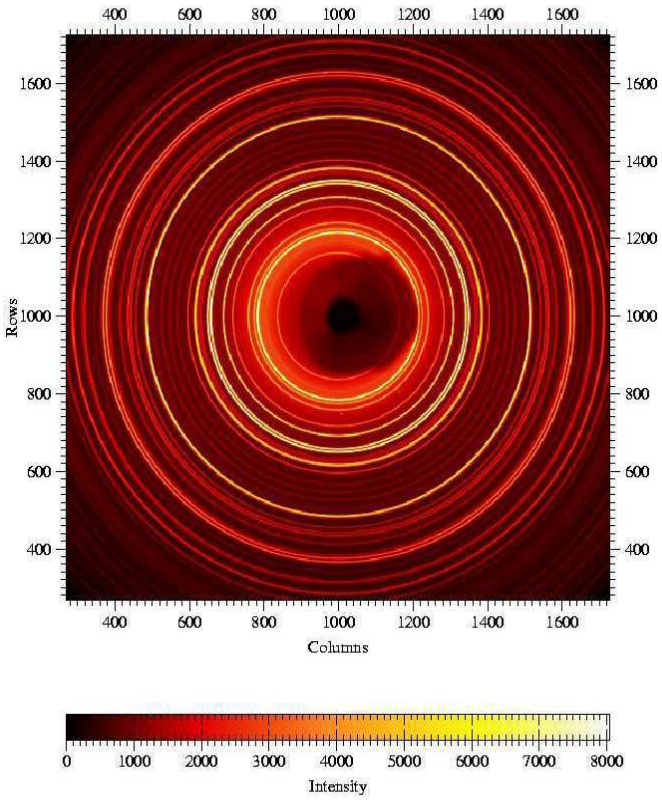

Figure 4.5: 2-D Powder diffraction pattern from a sample of olivine [110].

beam position, and the image distortions coming from the detector position [1], the *Fit2D* software, developed at ESRF, allows the extraction of the I(2θ) diffraction pattern with a simple integration.

4.3.2 The beamline ID30

The investigation of matter under extreme conditions is one of the natural issues addressed at a third generation synchrotron radiation source. Indeed, the highly collimated and intense X-ray beam available at the ESRF is the ideal tool for probing microscopic samples at maximum pressures and temperatures and for reducing the effects of gradi-

[1] *All these parameters are determined using the diffraction pattern of a well-known standard, typically* LaB_6 *or silicon*

ents in these variables. The ID30 high-pressure beamline was built to be fully dedicated to this topic.

It is a highly specialized beamline now in operation since June 1996 and is dedicated 25% to high-pressure large volume experiments in the Paris-Edinburgh press (HP-LVP) and 75% to high pressure Diamond Anvils Cell experiments. The main X-ray technique used is high resolution X-ray powder diffraction in monochromatic beam, although energy dispersive experiments are also possible. A schematic view of the beamline ID30 in large volume configuration is presented in figure 4.6

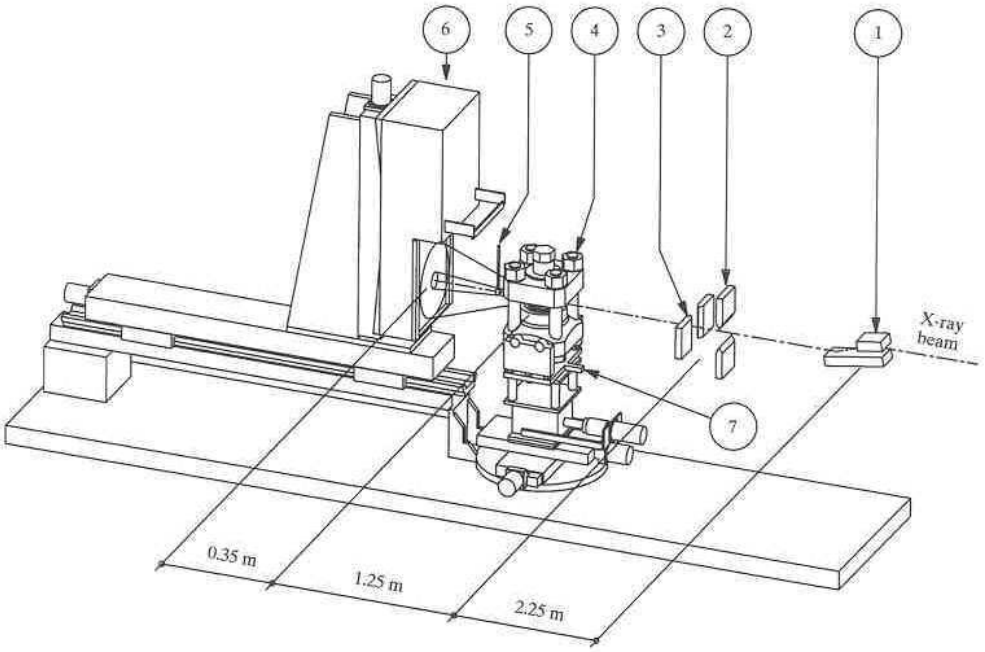

Figure 4.6: Layout of the high pressure beamline ID30 in LVP configuration. **1** : Si(111) channel-cut monochromator, **2-3** : Tungsten carbide slits, horizontal and vertical limits, **4** : Paris-Edinburgh Large Volume press, **5** : Beam stop, **6** : Image plate detector

The source: ID30 is equipped with three insertion devices (ID) on a high-β section ('*large*' source with a very small divergence). These IDs, two Undulators of 35 and 40 mm periods and a multipole Wiggler, are fully optimized for experiments at high pressure. They generate very bright beams at ultra-short X-ray wavelengths (0.25 Å for the undulators and 0.05 Å for the wiggler). For accurate X-ray powder diffraction

in monochromatic mode, the optimum X-ray energy considering the opening angle and the absorption of the diamond cells, is around 30 keV. This application, requires an excellent performance of the two phase undulators, which can close their magnetic gaps down to 16 mm and thus generate extremely bright beams in the X-ray energy region of interest. For the rest of the beamline activity (30%), i.e Paris-Edinburgh press and single crystal (in energy dispersive mode) experiments, a Wiggler W70 with high photon flux at high X-ray energies has been implemented in order to compensate for the huge absorption from the sample environment. At the minimum Wiggler gap, ID30 is ideally suited for experiments requiring energies up to 150 keV.

	Wiggler	**1st undulator**	**2nd undulator**
Magnet period	70 mm	40 mm	35mm
Max field	1.0 T	0.52 T	0.47 T
Min gap	16 mm	16 mm	16 mm

Table 4.1: Average parameters in the insertion devices of ID30

Optics: The optics of ID30 consists of a monochromator and a mirror system for focusing the beam. A water cooled Si(111) channel-cut monochromator is used to select monochromatic X-ray beam with wavelengths as short as 0.15 $\AA$ (E=100 keV). Two Kirkpatrick-Baez platinum-coated mirrors mounted on mechanical benders are used to obtain very bright and clean focal X-ray spots with a full width half maximum below 15 μm^2. The quality of the focussing optics is of primary importance for high pressure experiments because of the very small sample volume (typically 100 μm diameter by 40 μm thickness).

Detectors: The quality of the detector is of major importance for high pressure works. The criteria for a suitable detector in monochromatic mode are mostly dictated by the high pressure cell geometry (limited by 2 θ) and by the working X-ray energies. These criteria are listed below:

- a large input surface of more than 150 mm diameter;
- high spatial resolution;
- low noise and high dynamic range (14 bits or more);

- good sensitivity, even at high X-ray energies (60-80 keV);
- stable and easily tractable spatial distortions;
- fast reading (a few seconds or less) and erasing times;

The beamline ID30 is equipped with three different detectors:

Image plate detector: The MAR345 is a two-dimensional (2D) detector. It is equipped with a large image-plate surface (STN5 from Fuji) with a 345 mm diameter. The scanned size can be configured; possible resolutions are 1200, 2300, 3450 pixels. the pixel size can be chosen; the minimum size being 100x100 μm^2. A photograph of ID30's MAR345 is shown in figure 4.7

Figure 4.7: Photograph of the image plate detector, MAR345, used at the ID30 beamline.

CCD camera: A commercial large area CCD (Charge Coupled Device) detector (Bruker 6500) is available at ID30, which is optimized for high X-ray energies. It is of special interest for the new studies that are under development at the beamline ID30: *in situ* chemistry at high pressure in the Paris-Edinburgh press, single crystal in monochromatic mode and laser heating in DAC.

Image plate detectors may be a source of inaccurate integration of the images, due to the vibrations intrinsic to the detector, and to the repositioning of the plate after reading the data. All these movements of the plate lead to a continuous change in the

perpendicularity between the surface of the detector and the incident beam. The effect of a bad orientation of the detector surface is an elliptical deviation from the circular shape of the diffraction signals. For that reason, image plate detectors are usually provided with a convenient software to calculate the tilt angles from the shape of the diffraction images. The image plate detector, MAR345, has been used for the diffraction experiments presented in this thesis. The data obtained can be treated and integrated with the software Fit2D developed at the ESRF [110].

The Multi-Channel Collimator (Soller slits)

A new Multi-Channel Collimator optimized for the use of the Paris-Edinburgh press in combination with a 2D imaging plate detector was developed at the ID30 beamline. This system allows the *in situ* collection of high quality X-ray diffraction data of liquids, amorphous and crystalline materials at both high pressure and high temperature conditions. It has allowed excellent improvements in terms of signal to background ratio obtained.

The determination by X-ray diffraction of the evolution at high pressure-high temperature of the inter-atomic distances and number of first neighbors of disordered systems (liquids, amorphous materials), is of great importance in various domains such as material science or geophysics. This lack of information on the structure of weakly scattering compounds at high pressure is mostly due to experimental difficulties : i.e. low and diffuse signal, high background, high chemical reactivity of liquid phases at high temperature. Thus, the weak diffraction from the sample is seriously contaminated by its heavy environment. This contamination is usually difficult to subtract, as it changes with pressure and temperature conditions. For experiments with the Paris-Edinburgh press in particular, the sample is confined within a complex environment (BN capsule, graphite heater, boron-epoxy gasket). This environment, which is necessary to ensure an efficient thermal insulation and to produce quasi-hydrostatic pressure conditions, generates a strong X-ray diffraction background. In order to eliminate this parasitic signal, a simple idea already employed for the energy dispersive X-ray diffraction method consists on limiting by a convenient slits system the volume seen by the detector to just the sample volume. This simple method cannot be applied in monochromatic mode because of the 2-dimensional nature of the detection. In order to measure high quality diffraction data of non-crystalline samples a collimator with multiple channels (multi-channel collimator, MCC) can be used, as represented in figure 4.8. In this case the spatial selectivity operates simultaneously in the whole angular domain defined by the

detector area and the opening angle of the pressure cell.

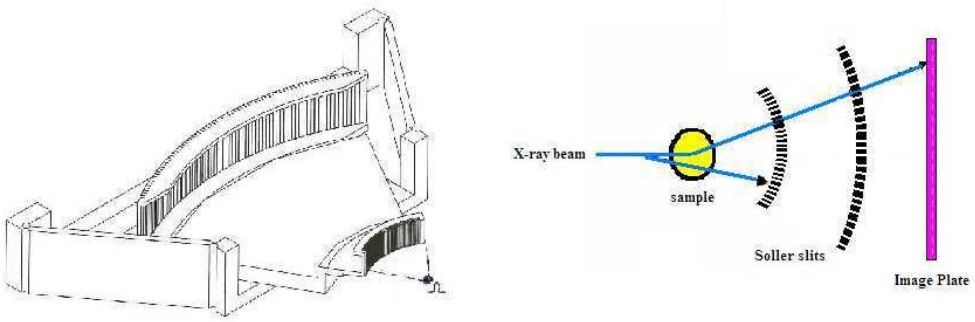

Figure 4.8: Scheme of the Soller slits design and their functioning.

The volume seen by the detector is defined by the inner and the outer slit network. A compromise that is difficult to attain, between the optimal dimension of the network of slits and the machining limitations of a highly X-ray absorbing material, i.e., a heavy metal, must be found. For the design of the slits the dimensions were optimized for the Paris-Edinburgh press geometry. In particular, the constraints concerning the opening angles defined by the WC-anvils in the vertical plane (15^o) and by the aperture of the Paris-Edinburgh press in the horizontal plane (60^o) were used to initially define the slits network geometry. The Soller slits system optimized for the Paris-Edinburgh press and developed at ID30 consists of two sets of slits, in an inner and outer block, with a radial alignment. It is set on a goniometer, so it can be oscillated during the measurements. Before the experiment, it must be centered on the beam, so that only the beam diffracted by the sample passes through. The widths of the inner and the outer slits, $w_i = 100$ μm and $w_o = 300$ μm, determine the divergence and the brightness of the channel. The Soller-slit system is made of highly absorbing Tantalum which allows for an excellent improvement in terms of signal to noise ratio. Tantalum was chosen as bulk material for two main reasons: i) it is a heavy metal with high X-ray absorption; ii) it can be machined with high precision using wire electro-erosion. The basal plate supporting the slits system is made of Invar in order to prevent any variation of the system dimensions in case of temperature fluctuations in the experimental hutch. The alignment procedure of the Soller slits system is quite fast when compared with previous existing systems. The complete positioning of the LVP-MCC is done in few hours. The

inner and outer central slits are aligned parallel to the beam axes by iterative rotation and translation perpendicular to the beam axis. For this task, a visible red laser that reproduces the beam path is used. Then, the parallelism is checked by scanning the slits system successively in rotation and translation, relative to the X-ray beam. The transmission signal through the slits is measured by a silicon photodiode positioned behind the slits.

4.3.3 2004/2005: ID27 becomes the new high pressure beamline

The ID30 beamline stopped its activity in August 2004. At the beginning of 2005 a new beamline, ID27, fully optimized for monochromatic high-resolution X-ray diffraction (XRD) under extreme pressure and temperature has been built [112]. ID27 is based on the same principle as ID30, however, in the new instrument important upgrades have been realized, principally concerning the changes of the X-ray source and the monochromator.

Beamline ID27 is upgraded with two U23 in-vacuum small-gap undulators on a low-β section (small source but higher divergence in the horizontal direction). The source size at ID27 is approximately seven times smaller than the source at ID30 in the horizontal direction, which allows for a much better focusing in this direction.

The X-ray optics installed at beamline ID27 are based on the same principle as ID30 because of their simplicity and flexibility. The water-cooled channel-cut Si(111) monochromator available at ID30 has been replaced by a more efficient nitrogen-cooled monochromator [113], because of the high heat load generated by the two in-vacuum undulators. The dimensions of this monochromator are optimized to select a broad energy domain from 6 keV (equal to 2 Å) to 90 keV (equal to 0.14 Å) which largely covers the energy band needed for high-pressure diffraction experiments. The 170 mm-long multilayer mirrors of ID30 were upgraded to a pair of 300 mm-long mirrors at ID27, developed by the ESRF optics group [114]. The optical acceptance of these new mirrors is 70% greater than that of the 170 mm mirrors, giving a substantial gain in photon flux. Moreover, their alignment is simple and fast and they are mechanically very stable. A focal beam spot of 6 μm diameter at full width half-maximum (FWHM) is easily obtained.

ID27 has been used for the final series of experiments of this thesis project.

4.4 Inelastic X-ray scattering

The inelastic x-ray scattering (IXS) technique allows to determine experimentally the dynamic structure factor $S(Q,\omega)$, which is the time and space Fourier transform of the correlation function of the particle density fluctuations in the investigated system.

IXS is a powerful method to investigate the high frequency collective dynamics in liquids and disordered systems. Traditionally the study of the atomic motion in condensed matter in this high frequency region has been the domain of inelastic neutron scattering (INS). Neutrons are particularly suited to these studies mainly for two reasons:

- neutrons with wavelengths comparable to the interparticle spacing have kinetic energy of $\cong 100\ meV$, and therefore, with a moderate relative energy resolution, it is possible to study efficiently the collective atomic excitations.
- neutrons scatter from the nuclei;

The INS technique has been successfully applied to the study of the density fluctuations spectrum of crystalline solids and low density gases. In disordered systems, like liquids, glasses and dense gases, very few neutrons studies have been performed so far. In fact, due to the kinematics of the scattering process, the neutron technique cannot be efficiently applied to study sound modes in materials with a large speed of sound, typically above 1500 m/s. These kinematics limitations do not apply to x-rays which are, therefore, particularly well suited to study the small momentum and large energy transfer regions.
The kinematics of an inelastic x-ray scattering process is illustrated in figure 4.9. A photon with an initial energy $\hbar\omega_0$, a wave vector $\mathbf{k}_0$, and a polarization ϵ_0, impinging upon a target, S, is scattered in the solid angle $d\Omega$, centered on the scattering angle θ. The scattered photon will have a final energy $\hbar\omega_1$, a wave vector $\mathbf{k}_1$, and a polarization ϵ_1.

From the energy-momentum conservation law, the energy, $\hbar\omega$, and momentum, $\mathbf{Q}$, transferred to the scattering system are $\hbar\omega = \hbar\omega_0 - \hbar\omega_1$ and $\mathbf{Q} = \mathbf{k}_0 - \mathbf{k}_1$.
When $\omega << \omega_0$ the wave vectors $\mathbf{k}_0$ and $\mathbf{k}_1$ have basically the same modulus and, as a consequence, the momentum transfer is simply connected to the scattering angle 2θ by the relation $Q = 2k_0 sin(\theta)$. The scattered intensity is determined by the scattering *double differential cross-section* $\partial^2\sigma/\partial\Omega\partial\omega_1$, which determines the number of scattered photons into a solid angle $d\Omega$ around the direction defined by $\mathbf{k}_1$, with a frequency ω_1 in the solid angle $d\Omega$.

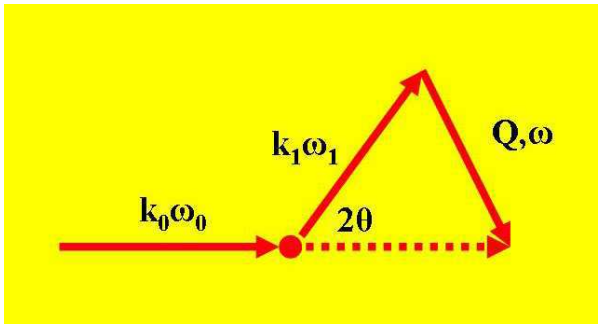

Figure 4.9: Kinematics of the inelastic x-ray scattering process.

4.4.1 Inelastic X-ray scattering cross-section

For x-rays in the energy range of $10 - 20$ keV, neglecting the magnetic term and for energies away from the absorption edge, the scattering cross-section reduces to the following simple expression:

$$\frac{\partial^2\sigma}{\partial\Omega\partial\omega_1} = r_e^2\left(\frac{\omega_1}{\omega_0}\right)(\epsilon_\mathbf{0}\cdot\epsilon_\mathbf{1})^2\sum_{I,F}p_I\left|\langle\Phi_F|\sum_j e^{i\mathbf{Q}\cdot\mathbf{r_j}}|\Phi_I\rangle\right|^2\times\delta(E_F-E_I-\hbar\omega) \tag{4.7}$$

where p_I is the statistical weight of the initial state $|\Phi_I>$. Using the integral representation of the δ function, the Van Hove transformation [115,116] and the definition [115]:

$$\left(\frac{d\sigma}{d\Omega}\right)_{th} = r_e^2\left(\frac{\omega_1}{\omega_0}\right)(\epsilon_\mathbf{0}\cdot\epsilon_\mathbf{1})^2 \tag{4.8}$$

the double differential cross-section can be rewritten as:

$$\frac{\partial^2\sigma}{\partial\Omega\partial\omega_1} = \left(\frac{d\sigma}{d\Omega}\right)_{th}\frac{1}{2\pi}\int\sum_{l,l'}< e^{-iQ\cdot r_l(t)}e^{iQ\cdot r_l(0)} > e^{-i\omega t}dt \tag{4.9}$$

The integral representation is used to highlight that the cross-section can be expressed as the time evolution of ground state properties and, in fact, it corresponds to the Fourier transform in space and time of the electron-electron pair correlation function. This quantity is by definition the dynamic structure factor of the electron density, $S(Q,\omega)$:

$$S(Q,\omega) = \int \sum_{l,l'} < e^{-iQ\cdot r_l(t)} e^{iQ\cdot r_l(0)} > e^{-i\omega t} dt \tag{4.10}$$

The quantity $(\frac{d\sigma}{d\Omega})_{th}$ corresponds to the coupling of the beam to the scattering system and does not depend on the detailed properties of the scattering system. It is possible to reduce further the expression 4.7, and to derive a relation where, instead of the electron-electron pair correlation function, one directly considers the dynamic structure factor associated to the atomic motion. This is possible within the validity of the following two assumptions:

- The validity of the adiabatic or Born-Oppenheimer approximation. It assumes that electronic velocities are much greater than ionic velocities; one therefore assumes that because ions move so slowly compared to electrons, at any moment electrons are in their ground state for that particular instantaneous ionic configuration. This allows to separate the electronic and the ionic motion. This means that the wavefunction Φ that describes the *ensemble* ions plus electrons of our target can be factorized in the product of a wavefunction ϕ describing the ions states depending on the nuclear coordinates and a wavefunction ψ describing the electrons states which depends only parametrically on the nuclear coordinates. For a monoatomic system we then assume that the initial and final states can be written as:

$$\begin{aligned} \Phi_I &= \phi_{I_N}(\mathbf{R_1},\ldots,\mathbf{R_N}) \cdot \psi_{I_e}(\mathbf{r_1^1},\ldots,\mathbf{r_z^1}\ldots\mathbf{r_1^N},\ldots,\mathbf{r_z^N}) \\ \Phi_F &= \phi_{F_N}(\mathbf{R_1},\ldots,\mathbf{R_N}) \cdot \psi_{F_e}(\mathbf{r_1^1},\ldots,\mathbf{r_z^1}\ldots\mathbf{r_1^N},\ldots,\mathbf{r_z^N}) \end{aligned} \tag{4.11}$$

  where $\mathbf{R}$ and $\mathbf{r}$ are respectively the ions and electrons position vectors, N and Z the ions and the electrons numbers, $\phi_{I_N}(\mathbf{R_1},\ldots,\mathbf{R_N})$, $\phi_{F_N}(\mathbf{R_1},\ldots,\mathbf{R_N})$ the ions wavefunctions, and finally $\psi_{I_N}(\mathbf{r_1^1},\ldots,\mathbf{r_z^1}\ldots\mathbf{r_1^N},\ldots,\mathbf{r_z^N})$, $\psi_{F_N}(\mathbf{r_1^1},\ldots,\mathbf{r_z^1}\ldots\mathbf{r_1^N},\ldots,\mathbf{r_z^N})$ are the wavefunctions of the electrons on the nth atom. This approximation neglects any interaction between electrons of different atoms, and between electrons of one atom with the nucleus of another atom. This approximation is particularly good as far as the energy transfers are small with respect to the electron excitation energies, and therefore it assumes implicitly that the valence electrons with small binding energies are few compared to the core electrons, an assumption that is valid in most cases.

- The scattering process does not lead to electronic excitations; this means that the difference between initial and final state concerns only excitations related to atomic density fluctuations.

The double differential scattering cross-section, under these hypotheses, can be written as:

$$\frac{\partial^2\sigma}{\partial\Omega\partial\omega_1} = r_e^2\left(\frac{\omega_1}{\omega_0}\right)(\epsilon_0\cdot\epsilon_1)^2\sum_{F_N I_N} p_{I_N}\left|<\phi_{F_N}|\sum_l f_l(Q)e^{-iQ\cdot R_l}|\phi_{I_N}>\right|^2\delta(E_F-E_i-\omega)$$

$$= r_e^2\left(\frac{\omega_1}{\omega_0}\right)(\epsilon_0\cdot\epsilon_1)^2|f(Q)|^2\frac{1}{2\pi}\frac{1}{N}\int dt e^{-i\omega t}\sum_{l,l'}<e^{-iQR_l(t)}e^{-iQR_{l'}(0)}>\Rightarrow$$

$$\boxed{\frac{\partial^2\sigma}{\partial\Omega\partial\omega_1} = r_e^2\left(\frac{\omega_1}{\omega_0}\right)(\epsilon_0\cdot\epsilon_1)^2|f(Q)|^2 S(Q,\omega)} \tag{4.12}$$

4.4.2 Triple axis spectrometer

The general principle of a triple axis spectrometer is schematized in figure 4.10
The first axis corresponds to the backscattering crystal monochromator, here the energy E_i of the incident beam is selected by an elastic Bragg scattering process. The second axis, corresponds to the sample. If we collect the photons scattered at an angle θ, we also choose the moment transfer Q. The scattered photons of energy E_f are finally analyzed by the backscattering crystal analyser through an elastic Bragg scattering process, as in the case of the first axis. This analyser defines the third axis. According to the Bragg's law, the energy difference between incident and analyzed beam can be achieved by varying the lattice parameter d_h of one of the two crystals by changing its temperature. This latter method is well suited for high resolution inelastic x-rays scattering to perform energy scan at fixed momentum transfer. To obtain high energy resolution, two conditions are necessary:

- use of high order reflections from perfect crystals
- use of an extreme backscattering geometry

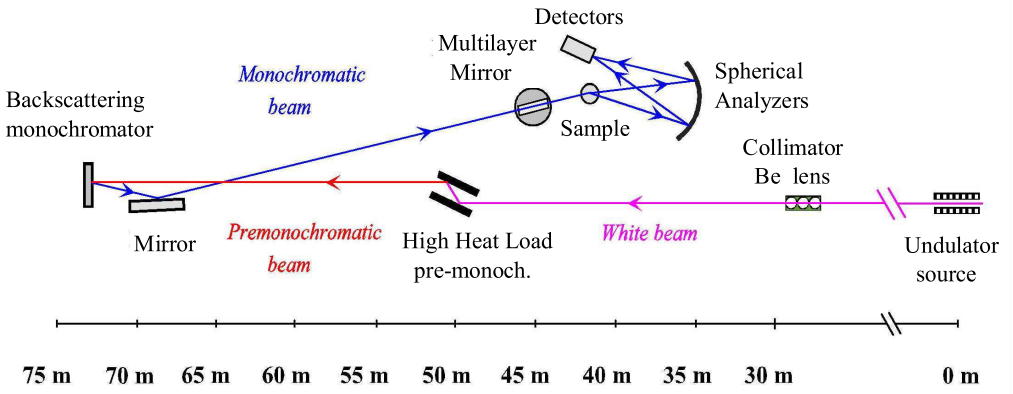

Figure 4.10: Schematic side view of the main optical elements of the ID16 spectrometer. The optical lay-out is based on the triple-axis principle, composed of the very high energy resolution monochromator (first axis), the sample goniometry (second axis) and the crystal analyser (third axis).

In the conditions of backscattering chosen for the design of ID16 (θ=89.98^o), the energy resolution provided by the backscattering monochromator, $\frac{\delta E}{E}$, can approximated by its contribution, $(\frac{\delta E}{E})_h$, due to the intrinsic properties of the crystal.

The best relative energy resolution $(\frac{\delta E}{E})_h$ at a given diffraction order h, can be derived in the framework of the Dynamical Theory of x-ray diffraction [117]. Using this theory, the *extinction length* t_{ext} defined as the penetration length of the beam into a perfect crystal in the direction perpendicular to the diffraction planes after which the intensity of the incident beam has decreased by 1/e, can be calculated as:

$$t_{ext} = \frac{V}{2dr_0C|F_h|} \tag{4.13}$$

where V is the unit-cell volume, r_0 the classical electron radius, C the polarization factor and F_h the crystal structure factor.

At a given diffraction order h, the best relative energy resolution is an intrinsic property of the crystal. This quantity is inversely proportional to the number of lattice planes effectively involved in the reflection process. From the dynamical theory of x-ray diffraction [117] this quantity can be related to the extinction length through the relation:

$$\left(\frac{\delta E}{E}\right)_h = \frac{1}{\sqrt{b}\pi}\frac{2d}{t_{ext}} \tag{4.14}$$

where b is the asymmetry factor[2]. From eq. 4.13 and eq. 4.14 we derive that the intrinsic energy resolution of a Bragg reflection varies with the square of the d-spacing d and is proportional to the structure factor F_h. Most importantly, it is independent of the Bragg angle θ. This is a very important point, which underlines the fact that the resolving power is determined by the number of planes participating in the diffraction process. This number of planes is determined by the transmission and reflection probabilities of a single plane, a quantity that again, cannot depend on the scattering geometry but only on the intrinsic properties of the reflection, i.e. the unit cell form factor F_h (calculated at the Q-value corresponding to the considered reflection $Q_h = 2\pi/d$), and the d-spacing d. This accounts for the decrease of $(\Delta E/E)_h$ with increasing the order of the reflection. In fact, both F_h and d decrease as the order is increased. The structure factor F_h is strictly connected to the atomic form factor $f(Q)$ through the relation $F_h = \sum_{i=1}^{N} f_i(Q)e^{iQ_h \cdot r_i}$. The atomic form factor, decreases with Q, or equivalently, with increasing the reflection order. As a consequence, increasing the reflection order one decreases the number of reflected photons by each plane. This allows the photons to penetrate deeply inside the crystal. This picture is true as far as the crystal is perfect and the penetration length due to the photoelectric absorption t_{abs} is larger then the extinction length t_{ext}.

For low order Bragg reflections, the extinction length is always much shorter than the absorption length. In a perfect silicon crystal, indeed, for Bragg reflection of low order, the Bragg reflection is described successfully by the dynamical theory of a perfect non absorbing crystal. The situation is not as satisfactory approaching $Q_h = 30\ \mathring{A}^{-1}$, here in fact the two lengths become equal. At even larger Q_h values, the ideal resolving power cannot be any longer achieved because the needed theoretical penetration depth into the crystal is limited by the photo-absorption length. The ideal penetration depth can also be reduced by crystal defects or imperfections which limit the maximum size of the grain that one considers to be the perfect crystal. In our specific context, therefore, the definition of perfect crystal is related to the considered reflection order, and the required crystal perfection implies that the relative variation of the lattice constant in the diffraction volume, $\Delta d/d$, is smaller than the intrinsic relative energy resolution

[2]The asymmetry factor is defined as: $b = sin(\theta - \alpha)/sin(\theta + \alpha)$, where α is the angle between the crystal surface and the family of the h diffracting planes.

of the considered reflection. In our case we aim to $\Delta E/E \approx 10^{-8}$. At high reflection orders, actually, this "perfection" is obtained only with silicon.

4.4.3 The beamline ID16

This paragraph is devoted to illustrate the characteristics of the ID16 beamline at ESRF. In particular we will review the working principle, the layout, and the general performances of this very high energy resolution spectrometer.

As described in previous section, an energy scan is possible either by varying the Bragg angle or by varying the lattice parameter d of one of the two crystals by changing its temperature. In the case of backscattering geometry it is not possible to change the relative energy between monochromator and analyser by changing the Bragg angles because, the energy variation is small and the loss in energy resolution, due to the geometrical contributions, becomes very large for small angle variations ($\approx tan\theta$). In order to overcome this difficulty, the energy scans can be performed by varying the other parameter: the lattice parameter d. A variation of d is obtained by changing the temperature of the crystal. In fact, a change ΔT induces a relative variation in the lattice constant given by:

$$\frac{\Delta d}{d} = \alpha(T)\Delta T \tag{4.15}$$

where $\alpha(T)$ is the coefficient of thermal expansion ($\alpha = 2.56 \cdot 10^{-6} K^{-1}$ in silicon at 294 K [118]). According to Bragg's law $\lambda = 2dsin\theta$ at fixed θ:

$$\frac{\Delta\lambda}{\lambda} = \frac{\Delta E}{E} = -\frac{\Delta d}{d} = -\alpha(T)\Delta T \tag{4.16}$$

This shows that a scan $\Delta d/d$ is analogous to a scan $\Delta E/E$. Therefore, the energy scans between monochromator and analyser are obtained by changing the temperature of one of the two crystals, in our case the monochromator, keeping the other crystal (the analyser) at constant temperature. Under these experimental conditions the geometrical contributions to the energy resolution are constant because the scattering geometry of the first and third axis is the same for any energy transfers. To obtain a sufficiently small energy step size for reflections with a resolving power $\Delta E/E$ in the order of $10^{-7} - 10^{-8}$, the temperature of the monochromator and analyser crystals has to be controlled with mK precision, considering that $\alpha \approx 10^{-6}$. A schematic side view of the main optical elements of the beamline and of the horizontal spectrometer is shown in figure 4.10. Starting form the source and following the x-rays path down to the detector, the main

characteristics of each element will be discussed in some detail. The vertical scale is expanded with respect to the horizontal one to better show the different components.

Undulator source: The x-rays source is composed of three linear undulators with a magnetic period of 35 mm and length 1.6 m, which are located on a high-β straight-section of the storage ring. The undulators are normally used from the 3rd to the 7th harmonic in order to cover an the energy range from 7 to 30 keV. The angular divergence of the central cone of the X-ray beam coming from the undulators is roughly 15 vertical x 40 horizontal μrad^2 (FWHM), with a bandwidth $\delta E/E = 10^{-2}$ and an integrated power of roughly 200 W.

Double-Crystal Premonochromator: The white x-rays beam coming from the undulators is premonochromatized by a Si(1,1,1) double crystal monochromator to a bandwidth of $\delta E/E = 2 \cdot 10^{-2}$. The premonochromator is cryogenically cooled with a closed-loop circuit of nitrogen in order to absorb the beam power and to reduce thermal deformations. The premonochromator crystal works in nearly fixed-exit conditions and diffracts the beam vertically 22 mm above the white beam. In the used energy range $(7-28keV)$ the angular acceptance of the Si(1,1,1) crystal is either larger or pretty well matched to the vertical divergence of the undulator source.

High Energy Resolution crystal Monochromator: The photons coming from the premonochromator impinge on the very high resolution monochromator constituted by a flat Si(1,1,1) crystal symmetrically cut and temperature controlled with a precision in the mK range. The specific Si(h,h,h) reflection is chosen by simply tuning the premonochromator Bragg angle at the correct energy and adjusting the undulator gap accordingly. The Bragg angle of the Si(1,1,1) matching the energy of a Si(h,h,h) reflection with $\theta_B = 90^0$ is given by the relation:

$$2d_1 sin\theta = 2d_h = \frac{2d_1}{h} \rightarrow sin\theta = \frac{1}{h} \tag{4.17}$$

where h indicates the desired reflection order. The monochromator crystal has an operative Bragg angle of 89.98^0 in the vertical plane and the diffracted x-ray beam is monochromatized to a bandwidth $\Delta E/E$ in the order of $10^{-6} - 10^{-8}$. This extreme backscattering angle, is chosen to insure that the divergence of the incoming beam is always much smaller than the Darwin width of the considered reflection, while the deviation from perfect backscattering is still large compared to the beam divergence.

The design and the performances of this very high energy resolution monochromator are described in detail in ref. [119].

Toroidal mirror: The very high energy resolution x-ray beam is focused on the sample by a grazing incidence (2.76 mrad) toroidal mirror to a spot size of 100 vertical x 250 horizontal μm^2 (FWHM). The mirror has a platinum coating deposited on the optically polished surface obtained from a silicon substrate. The mirror has two arms of 78 m and 24 m. This gives approximately 3:1 demagnification of the source in the image plane at the sample position.

High Energy Resolution Spherical Crystal analyser: The photons scattered by the sample are collected by a spherical silicon crystal analyser positioned at the tip of an arm able to rotate around the scattering sample in order to select the desired Q-value. This analyser crystal is operating at the same Si(h,h,h) as the monochromator crystal and at a Bragg angle very close to backscattering ($\theta = 89.98^0$). This spherical analyser crystal is also temperature controlled with a precision in the mK range, and it is desired to have the same energy resolution as the monochromator crystal but with a much larger angular acceptance. This angular acceptance is chosen by moving a set of apertures in front of the analyser crystal, and it is defined by the desired Q-resolution. An angular acceptance up to $4x10\ mrad^2$ is an adequate compromise of Q-resolution ($\Delta Q \approx 0.5nm^{-1}$) and signal maximization. Such a large angular acceptance, larger than the deviation $\epsilon = 350\mu rad$ from perfect backscattering, can be only obtained by using a focussing optics and by keeping, at the same time, the characteristics of a perfect crystal analyser. This excludes the possibility to bending a crystal because such a procedure introduces important deformations which degrade the energy resolution [119]. A possible solution to the problem is to position small flat crystals, squares of side length c, on a focusing substrate of radius R, where $c \ll R$. Providing that this focusing substrate is a sphere in 1:1 Rowland geometry, the Bragg angle variation on these small crystals will be c/R. If the size c is chosen in a way that the ratio c/R is comparable or smaller than the Darwin width, the spherical analyser will reflect the X-rays with almost the intrinsic energy resolution of the considered reflection. Following this idea, within the Inelastic X-ray Scattering Group at the ESRF a method has been developed that allows to glue 12000 independent silicon crystals on a spherical substrate with radius R. The spherical substrates are obtained from silicon disks with a diameter of 100 mm. The size c of these small crystals is $\sim$ 0.7 x 0.7 mm^2, and their thickness is 3 mm [120, 121].

At the moment at the beamline ID16 there are five analysers simultaneously working during an IXS experiment. They are fixed at the end of an arm able to rotate in the horizontal plane and are located one next to the other with an angular offset of 1.56^0. This allows to measure five IXS energy spectra at five different Q-values simultaneously. The arm, 6.5 m long, is able to cover an angular range between 0^0 and 13^0. With such a considerable length, it is possible to reduce the geometric contribution to the energy resolution function. The spherical analysers with a radius R = 6500 mm are equipped with analyser slits. The most used reflections at the beamline are the Si(h,h,h) with h = 5, 7, 8, 9, 11, 12, 13.

Detector: The detector is a silcon diode with 2.5 mm equivalent thickness and with a background signal of the order of 1 $count/min$. The detector is placed on the same arm as the analyser crystal. On this arm are also mounted an entrance pinhole placed just after the sample and a detector pinhole placed before the detector (see figure 4.10). Due to the extreme backscattering geometry the detector is basically on top of the entrance pinhole at a distance from the scattering plane ranging between 3-4 mm.

Beamline performances

Momentum resolution: The momentum resolution is basically determined by the opening of the analyser's slits at the selected Si(h,h,h) reflection. This value is related to the minimum scattering angle that allows to avoid that the direct beam transmitted by the sample enters in the spectrometer vacuum chamber through the spectrometer entrance pin-hole.

Energy resolution: The energy resolution is measured by looking at the elastic scattering from a 5 mm thick polymethylmethacrylate (PMMA) sample at $Q = 10\ nm^{-1}$. At this Q value the spectrum of PMMA is dominated by the extremely narrow quasi-elastic component, namely the incident beam can be assumed as a delta function of the energy. The inelastic scattering contribution has been further reduced by keeping the PMMA at 10 K. At this temperature the inelastic signal is drastically reduced over the whole Q range, allowing measurement of the energy resolution, even at Q values lower than $Q = 10\ nm^{-1}$ and excluding the presence of any unwanted Q-dependence. The measured experimental resolutions are presented in Chapter 6. Using the horizontal arm analyser with $R = 6500\ mm$ we measure an energy resolution of $1.5 \pm 0.2\ meV$ at the Si(11,11,11) reflection with an angular acceptance of 100 $mrad^2$.

4.5 Raman spectroscopy

The Raman effect has been discovered in 1928 by the Indian Venkata Raman; it is consequent to the interaction of the electromagnetic (visible) radiation and the molecules or the lattice vibrations. The interaction can induce one of two different scattering processes, i.e. Rayleigh and Raman diffusion. The Raman diffusion is 10^3-10^5 times less probable than the Rayleigh diffusion.

The Rayleigh scattering is an elastic process. The Raman diffusion is an inelastic process: the incident beam interacts with the rotation or vibration modes of the molecules or with the phonons of the lattice, and, as consequence of energy exchanges, the wavelength of the diffused beam will be different respect to the one of the incident beam. Historically, the two distinct contributions to the Raman signal are referred as Stokes and anti-Stokes scattering lines. The Stokes contribution follows to an energy absorption, while the anti-Stokes contribution follows the relaxation of excited states; for that reason the Stokes spectral lines are observed at lower frequencies respect to the frequencies of the anti-Stokes spectral lines. A diagram that reports the energy exchanges related to the Rayleigh and Raman processes is represented in figure 4.11.

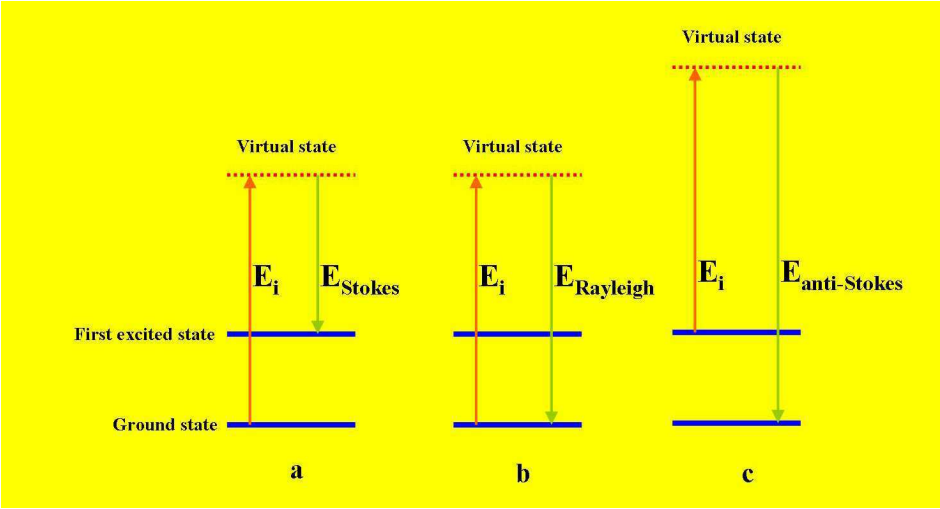

Figure 4.11: Energy level diagram for Raman and Rayleigh scattering; (a) Stokes Raman scattering, (b) Rayleigh elastic scattering, and (c) anti-Stokes Raman scattering.

If the excitation frequency of a such mode is ν_c and the frequency of the incident radiation is ν_i, the frequency of the Stokes line will be ν_i-ν_c, and the frequency of the anti-Stokes line will be at ν_i+ν_c. As consequence, the analysis of the Raman frequencies

gives us information about the energy of the characteristic molecule/lattice modes. It is noticeable that the anti-Stokes line is much less intense than the Stokes line. This occurs because only molecules that are vibrationally excited prior to irradiation can give rise to the anti-Stokes line. Hence, in Raman spectroscopy, only the more intense Stokes line is normally measured.

4.5.1 The Raman effect

The Raman effect is due to the interaction of the photons with the electrons of the matter. Let us to consider the interaction of electromagnetic radiation with a diatomic molecule. Suppose that the incident radiation has an angular frequency ω much higher than the angular frequency ω_v of the vibrational mode. It is reasonable to suppose that the distance between the nuclei, $r(t) = d_o + r_o cos(\omega_v t)$ varies with a velocity much less than that of one of the electrons. We can then separate the electronic and nuclear wave function (Born-Oppenheimer approximation), and the electron states can be studied as a function of the variable parameter r.

The electric field, $\vec{E}$(t)=$\vec{E_o}$cos(ωt), induces an electric dipole $\vec{M}(t)$ on the electronic cloud that can be expressed as:

$$\vec{M}(t) = \bar{\bar{\xi}}(\omega)\vec{E_o}cos(\omega t) \tag{4.18}$$

where $\bar{\bar{\xi}}(\omega)$ is the electric susceptibility tensor that depends on the distance r(t) between two nuclei. Being the nuclei distance a function of ω_v, $\bar{\bar{\xi}}(\omega)$ will depend also on the angular frequency of the vibration mode ω_v. $\bar{\bar{\xi}}(\omega)$ can be expanded around its average value:

$$\bar{\bar{\xi}}(\omega) = \bar{\bar{\xi}}_o(\omega) + \Big(\frac{\delta\bar{\bar{\xi}}(\omega)}{\delta r}\Big)_{d_o}(r - d_o) + ... =$$

$$= \bar{\bar{\xi}}_o(\omega) + \Big(\frac{\delta\bar{\bar{\xi}}(\omega)}{\delta r}\Big)_{d_o} r_o cos(\omega_v t) + ... \tag{4.19}$$

The ω_v dependence of the susceptibility $\bar{\bar{\xi}}(\omega)$ implies that the amplitude of the induced dipolar moment $\vec{M}(t)$ is modulated by the vibration of the molecule. It can be written as:

$$\vec{M}(t) = \bar{\bar{\xi}}_o(\omega)\vec{E_o}cos(\omega t) + \Big(\frac{\delta\bar{\bar{\xi}}(\omega)}{\delta r}\Big)_{d_o} r_o\vec{E_o}cos(\omega t)cos(\omega_v t) + ... \tag{4.20}$$

Applying the trigonometric relation $cos\alpha\, cos\beta = \frac{1}{2}[cos(\alpha+\beta) + cos(\alpha-\beta)]$ to eq. 4.20, we obtain:

$$\vec{M}(t) = \bar{\bar{\xi}}_o(\omega)\vec{E_o}cos\omega t + \frac{1}{2}\Big(\frac{\delta\bar{\bar{\xi}}(\omega)}{\delta r}\Big)_{d_o} r_o\vec{E_o}cos(\omega+\omega_v)t + \frac{1}{2}\Big(\frac{\delta\bar{\bar{\xi}}(\omega)}{\delta r}\Big)_{d_o} r_o\vec{E_o}cos(\omega-\omega_v)t \tag{4.21}$$

Considering the spectrum as a function of ω, the Fourier transform of eq. 4.21 contains the observed Rayleigh (ω), Stokes ($\omega - \omega_v$) and anti-Stokes ($\omega + \omega_v$) contributions [122].

4.5.2 Experimental setup

The spectra collected for this thesis, were recorded in back-scattering geometry with a Jobin-Yvon (T-64000) multichannel spectrometer equipped with a 20 SLWD-microscope objective[3]. A picture of the spectrometer is shown in figure 4.12

Figure 4.12: Jobin-Yvon (T-64000) multichannel spectrometer at Université Joseph Fourier.

The relative weak intensity of the Raman effect imposes the use of a laser as light source. The laser beam is directed by a system of mirrors to a focussing/collecting lens. The scattered light is filtered to eliminate the Rayleigh signal. The scattered light is collected by a lens and then brought on a grating, which is used to separate the different wavelengths. Since light of different wavelengths is now traveling in different directions, at this stage the spectrometer selects wavelengths inside of a user-defined range. A second stage focusses the filtered light on a final grating. The dispersed light

[3] 20 indicates the magnification of the objective and SLWD is the acronym of Super Long Working Distance

is now analyzed as a function of position, which corresponds to wavelength. The signal as a function of position is read by the system detector. The wavelength/intensity information is then read by a computer and converted by the appropriate software to frequency/intensity data. The spectra are in general obtained by accumulating the scattered intensity in the Stokes region in the energy domain.

Part III

Results

Résumé du chapitre 5

Les mesures de diffraction et de Raman in situ sur le soufre ont permis d'observer des séquences structurales différentes en fonction de la pression. Dans la perspective de reconstruction du diagramme de phase il était donc intéressant de rechercher une correspondance entre les phases observées par les deux techniques et de vérifier la nature, stable ou photo induite, des phases observées par effet Raman.

La molécule S_8 constitue la base structurale la plus stable pour le soufre dans un grand domaine de température et de pression autour des conditions ambiantes. En particulier c'est l'élément de base des structures rhomboédrique, monoclinique et de l'ordre local du liquide juste au-dessus du point de fusion. Des monocristaux des phases rhomboédrique, et monoclinique ont pu être observés, dans le DAC, en équilibre avec le liquide ce qui constitue un bon critère de stabilité de ces phases. La courbe de fusion du soufre a été reconstruite jusqu'á 5 Gpa ; elle montre un point triple vers 2.3 Gpa et 577 K. Un ensemble de mesures de diffraction en DAC ou LVP a conduit á la détermination de la ligne de transition orthorhombique-trigonal et les points de coexistence appartiennent á un isotherme á 580K. Des mesures Raman ont été effectuées dans un domaine de longueur d'onde ou on n'attend pas de transition vers une phase polymérique. Puis, en choisissant un domaine de pression et température dans le domaine de stabilité de la phase trigonale on a pu établir ses liens avec la phase polymérique. Des mesures in situ haute température et haute pression ont établi l'existence d'une phase nouvelle, rhomboédrique, construite sur des molécules S_6, en correspondance avec les phases moléculaire et polymérique observées á la température ambiante par diffusion Raman. Le Facteur de structure du soufre liquide á été mesuré en fonction de la température, a pression ambiante, puis en augmentant la pression. Nous avons pu estimer un degré de polymérisation qui est en accord avec les données á basse pression de la littérature. Des mesures Raman montrent que la pression favorise la polymérisation du liquide. D'autre part la forme du facteur de structure mesuré á haute pression correspond parfaitement á celle du sélénium á pression ambiante ce qui conforte encore le rôle de la pression pour favoriser la polymérisation. Ces résultats ont abouti á la construction d'un nouveau diagramme de phases du soufre.

Chapter 5

The phase diagram of sulfur

It is easier to measure something than to understand what you have measured.

Anonymous

5.1 Introduction

As presented in the bibliographic chapter, there are numerous contradictions in the literature on sulfur: contradictions between X-ray and Raman results, or even between results obtained with the same technique. In particular, these discrepancies concern:

- *The existence and position of phase boundaries;*

- *The identification of thermodynamically stable polymorphs;*

For most part, these differences are due to inherent limitations in the experimental techniques employed, the currency of quench recovery methods, the formation of metastable phases (kinetics). In addition to that, we are forced to consider the high reactivity of sulfur[1] that limits the number of surrounding materials that are normally used for experiments at these extreme conditions.

The experimental approach is important in the study of such a complex system. For that reason, we have conducted an extensive *in situ* study in a wide pressure (P), temperature (T) domain: $0 < P < 15$ GPa and $300 < T < 1000$ K. The measurements have been carried out using powder and single crystal XRD and Raman spectroscopy.

[1] *For example, we have tested that, at high pressure (above 5 GPa) and high temperature (above 600 K) conditions, sulfur reacts with nickel and aluminium.*

These *in situ* techniques allow us to check the nature of the sample directly at the thermodynamic conditions of interest.

In this chapter, we review the available literature on XRD and Raman measurements and the results obtained with both techniques have been summarized graphically (section 5.2). This, combined with the introduction chapter, will serve as a basis for the interpretation of the data collected on solid and liquid sulfur. After this introduction, we successively present:

- The characterization of the low pressure polymorphs (P $<$ 0.5 GPa) using powder and single crystal XRD;

- The construction of the melting line (0-5 GPa) from powder XRD;

- The observation of the high pressure solid transformations (0-15 GPa) by powder and single crystal XRD and Raman spectroscopy;

-The characterization of the liquid state (0-2 GPa) by XRD and Raman spectroscopy;

-The phase diagram of sulfur (up to 15 GPa).

5.2 Solid Polymorphism

As discussed in the Chapter 2, α-orthorhombic sulfur is the stable thermodynamic phase of sulfur at ambient conditions. Other molecular [57] or polymeric [123] forms reported at ambient conditions in the literature are metastable.

What happens when the pressure is increased?

This question is difficult to answer based on the published data, many contradictory results are in fact reported. Indeed, the diffraction results conflict with the information obtained using Raman spectroscopy, suggesting that, up to 15 GPa, orthorhombic sulfur transforms to other phases only at high temperature [23] or if exposed to proper visible light [82, 124].

From ref. [82], it is clear that, if a laser of suitable wavelength and power is used to illuminate a sulfur sample, a transition from the molecular S_8 phase to a polymeric form (*p-S*) and then to the molecular S_6 can be detected. The dependence on the energy and the power of the laser indicates that these transformations are photo-induced. Besides that, at pressures above 12 GPa, a new phase called *hplt* (high pressure low temperature), has been observed by Hafner *et al.* [125]. From comparison between the Raman spectrum of the *hplt* phase and the spectra of known sulfur species, Hafner

et al. [125] conclude that the nature of *hplt* is polymeric. Analyzing the available spectroscopic data, it results that S_6 and *hplt* can be obtained pure or mixed with *p-S* phase at pressures higher than 12 GPa, depending only on the power density of the illuminating laser [82,126]. At higher pressures, the observation of these transitions does not depend on the wavelength of the laser used for the experiment. The pressures at which these transitions have been observed at room temperature and the corresponding wavelength have been reported in table 5.1.

Laser wavelength	**p-S**	**S_6**	**hplt**	**References**
488 nm	3.6 GPa	-	-	[127]
488 nm	-	9 GPa	-	[128]
488 nm	-	12 GPa	12 GPa	[125]
515 nm	-	12 GPa	12 GPa	[125]
515 nm	6 GPa	9.7 GPa	-	[129]
515 nm	5.2 GPa	-	-	[130]
515 nm	5.7 GPa	10 GPa	-	[124]
515 nm	5, 6-6.7 GPa	8.8, > 10 GPa	-	[131]
576-605 nm	?	12 GPa	?	[129]
590 nm	-	13 GPa	-	[124]
647 nm	13.2 GPa	13.2 GPa	20 GPa	[132]
647 nm	13.5 GPa	-	13.5 GPa	[132]
1064 nm	-	-	-	[133]

Table 5.1: Pressures onset of the appearance of *p-S*, S_6 and *hplt* and the different wavelength used for the experiments.

In order to clarify the situation, the laser radiation energy/wavelength and pressure effects on the transitions from S_8 to *p-S* (red dashed) and to S_6 (blue dashed) have been plotted in figure 5.1. In the same figure, we report the pressure dependence of the optical absorption edge of the S_8 molecule [134]. The experimental points above 12 GPa corresponding to: S_6, *hplt*, S_6-*hplt*, S_6-*p-S*, and *p-S* from table 5.1 have also been included. A correlation between the pressure dependence of the S_8-*p-S* transition and the optical absorption edge of sulfur is evident, the two sets of data are indeed almost parallel, shifted by ∼0.22 eV in energy or 1-1.5 GPa in pressure. A similar pressure dependence is also identified for the onset of the polymer to S_6 transition.

As already mentioned, no pressure-wavelength dependence can be ascribed to the transitions above 12 GPa (black dashed line in figure 5.1), where S_6, *hplt* and *p-S* make

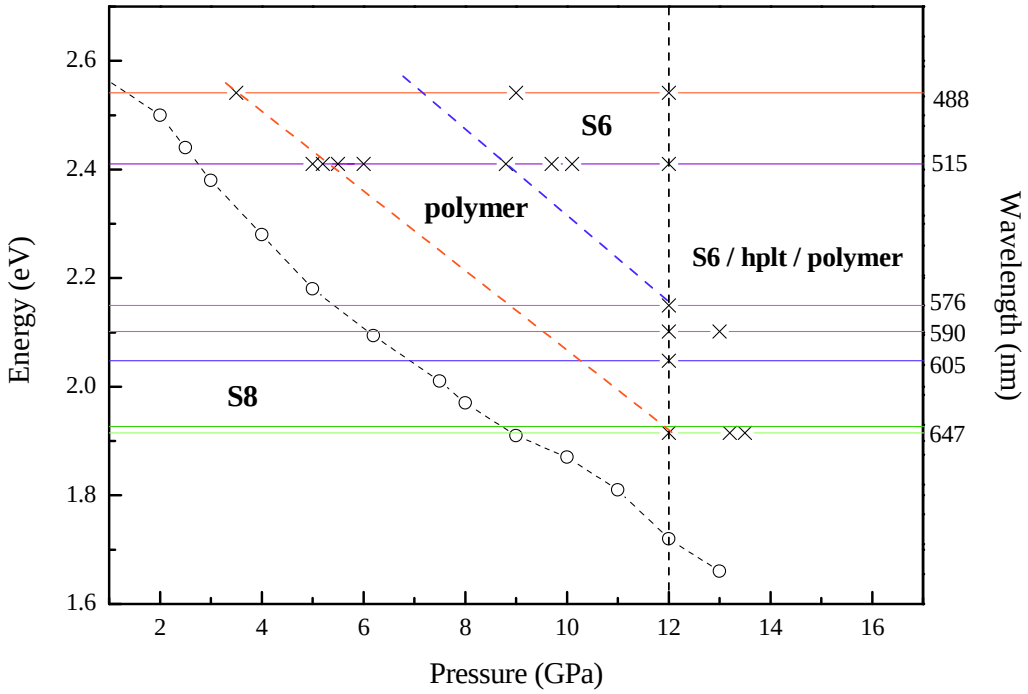

Figure 5.1: Diagram that illustrates the correlation between the energy and the pressure at which *p-S*, S_6 and *hplt* have been observed (the crosses correspond to the data of table 5.1) and the optical absorption edge of sulfur from [134] (open circles and black line). The dashed lines are guidelines to indicate the transition to *p-S* (red line) and to S_6 (blue line). Above 12 GPa (black dashed line) the three phases, *p-S*, S_6 and *hplt* can be observed, separately or mixed, depending only on the laser power.

a different scenario. However, the observation of these transitions is strongly dependent on the laser power used for the experiment. Indeed, Eckert *et al.* [82] have pointed out that if sulfur is illuminated with a laser light with average power density below 30 $\mu W/\mu m^2$, no transition to *p-S* can be induced; whatever is the laser energy [82].

In the light of these Raman results, several diffraction experiments have been performed over the same pressure range. At room temperature, Luo and Ruoff [52] have reported the observation of new phase around 5 GPa. The structure of this phase has been successively re-examinated and identified as orthorhombic S_8 phase [130]. This result is confirmed in the most recent *in situ* XRD works on sulfur performed at room temperature, where there are no indications for the occurrence of any phase transitions up to 36 GPa [45]; at this pressure, the transition from orthorhombic to tetragonal sulfur takes place.

As introduced above, the results obtained with Raman spectroscopy and XRD at

room temperature contrast: Raman data have evidence for three transitions up to 15 GPa (*p-S*, S_6 and *hplt*), while the most recent diffraction data have none up to 36 GPa [45, 46].

At high temperature (573K) Kusaba and Kikegawa [135] report the observation of three new phases in the range 3-16 GPa and 570-1170 K; however, their structures have not been fully characterized. One of these three phases, the lower pressure one, corresponds to the trigonal sulfur characterized by Crichton *et al.* [23]. The intermediate phase has been interpreted as molecular S_6 by the authors, while they do not give indications about the nature of the higher pressure phase. Sakurai *et al.* [136] report the observation of a new high pressure phase at 11 GPa by using a laser heating system. Based on the diffraction lines of this phase, Sakurai *et al.* [136] have evaluated it as being different from S_6. Comparing its diffraction pattern with the one reported by Fujihisa *et al.* [45], we conclude that it corresponds to the polymeric tetragonal phase. More recently, Degtyareva *et al.* [46] have reported a diagram that contains the line corresponding to the orthorhombic-trigonal and trigonal-tetragonal phase transformations. All these data are summarized in figure 5.2.

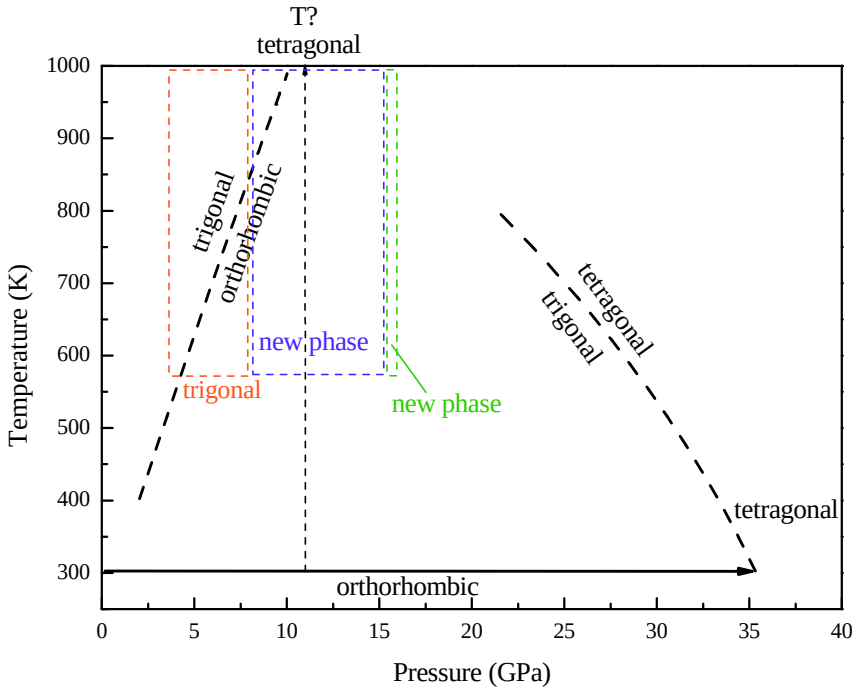

Figure 5.2: Summary of the different results that have been obtained on the solid phase transformation of sulfur in the 0-40 GPa pressure range (Data from ref. [45, 46, 48, 135, 136]).

The picture that emerges is confused, making it difficult to construct a reliable phase diagram that is coherent with all available information (see figure 5.2).

Another important point concerns the observation of a pressure-induced amorphization in solid sulfur and its interpretation. Using *in situ* XRD, Luo and Ruoff [52] have reported the occurrence of a pressure-induced amorphization at room temperature at a pressure around 25 GPa. Recently, Hejiny *et al.* [48] have demonstrated that this amorphization is an effect of the strain caused by the absence of an hydrostatic pressure medium.

A pressure-induced amorphization, associated with the weak and broad peaks in the Raman spectrum, is also reported by several authors [53, 82, 124]. The amorphization can be observed at about 1 GPa lower than the S_8-polymer transition [53]. By looking at figure 5.1, it is noticed that the pressure at which the amorphization is reported is close to the optical absorption edge of sulfur. A consequence is that the measured Raman intensity in the spectra of the pure amorphous phase is weak. In figure 5.3, we report a spectrum that has been associated with the amorphous phase [53]. At 4.6 GPa all the peaks relative to the S_8 molecule becomes broad and less intense, while at 5.5 GPa the peaks are not visible.

A possible interpretation of the amorphization phenomenon in sulfur has been suggested by Eckert *et al.* [126]. In their interpretation, the laser induces, in the solid as in the liquid [137], the opening of the S_8 rings and the formation of radicals that recombine randomly giving rise to the amorphous phase. Moreover, the fact that the transition to the polymeric phase is observed $\sim$0.22 eV higher than the absorption edge of sulfur, can be correlated to the torsional energy in the cis-trans conversion of the ring fragments into chain segments. Actually, this torsional energy is about 0.25 eV [126], value that is reasonably close to the 0.22 eV energy shift.

There are two proposed hypotheses to explain why phase transitions observed with Raman spectroscopy have not been observed with X-ray diffraction: 1) the laser provides the metastable S_8 form sufficient energy to promote the transitions to the thermodynamically stable phases; or, 2) the transitions are simply photo-induced. this implies a metastable character for the polymeric phase and also for the molecular S_6 phase. These hypotheses clearly need to be supported by experimental data. If the first hypothesis is correct, a correspondence between the transitions observed by Raman and the ones observed by XRD at high temperature must exist. Indeed, in most cases, a kinetically inhibited transformation between a metastable and the stable phase can be induced by increasing the temperature. Actually, this correspondence can be assumed if we consider

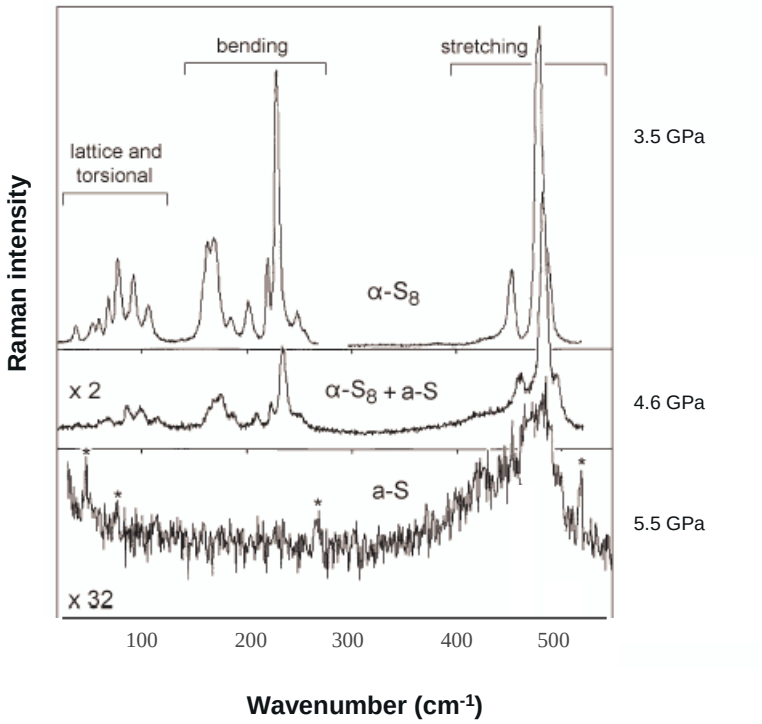

Figure 5.3: Pressure evolution of the Raman spectra from [53] using a laser with 515 nm wavelength. At the top is reported the spectrum of orthorhombic sulfur at ambient temperature and 3.5 GPa, increasing pressure (4.6 GPa) the peaks become weaker. At the bottom, the spectrum at 5.5 GPa associated to the pure amorphous phase is reported. Plasma lines of the Ar ion laser are marked by asterisks.

the transition from S_8 to *p-S* observed by Raman [82, 125, 130] and the orthorhombic to trigonal phase transition observed by XRD at 3 GPa and 673 K [23]. Most likely, the same assumption can be make considering, on one side, the transition from S_8 to polymeric *hplt* observed by Raman [125] and on the other side, the orthorhombic to polymeric tetragonal phase transition observed by Fujihisa *et al.* [45] at 36 GPa, and by Degtyareva *et al.* [46] at lower pressures and high temperatures using XRD. In this picture the missing link is molecular S_6: we need clear XRD evidence for molecular S_6 observed by Raman at high pressure.

In order to shed a light on this issue, and as consequence, on the phase diagram of sulfur, a detailed mapping has been performed varying the external pressure and temperature. In the next paragraphs, the information available from X-ray diffraction and Raman spectroscopy have been cross-linked in order to define the stability domains of the sulfur polymorphs.

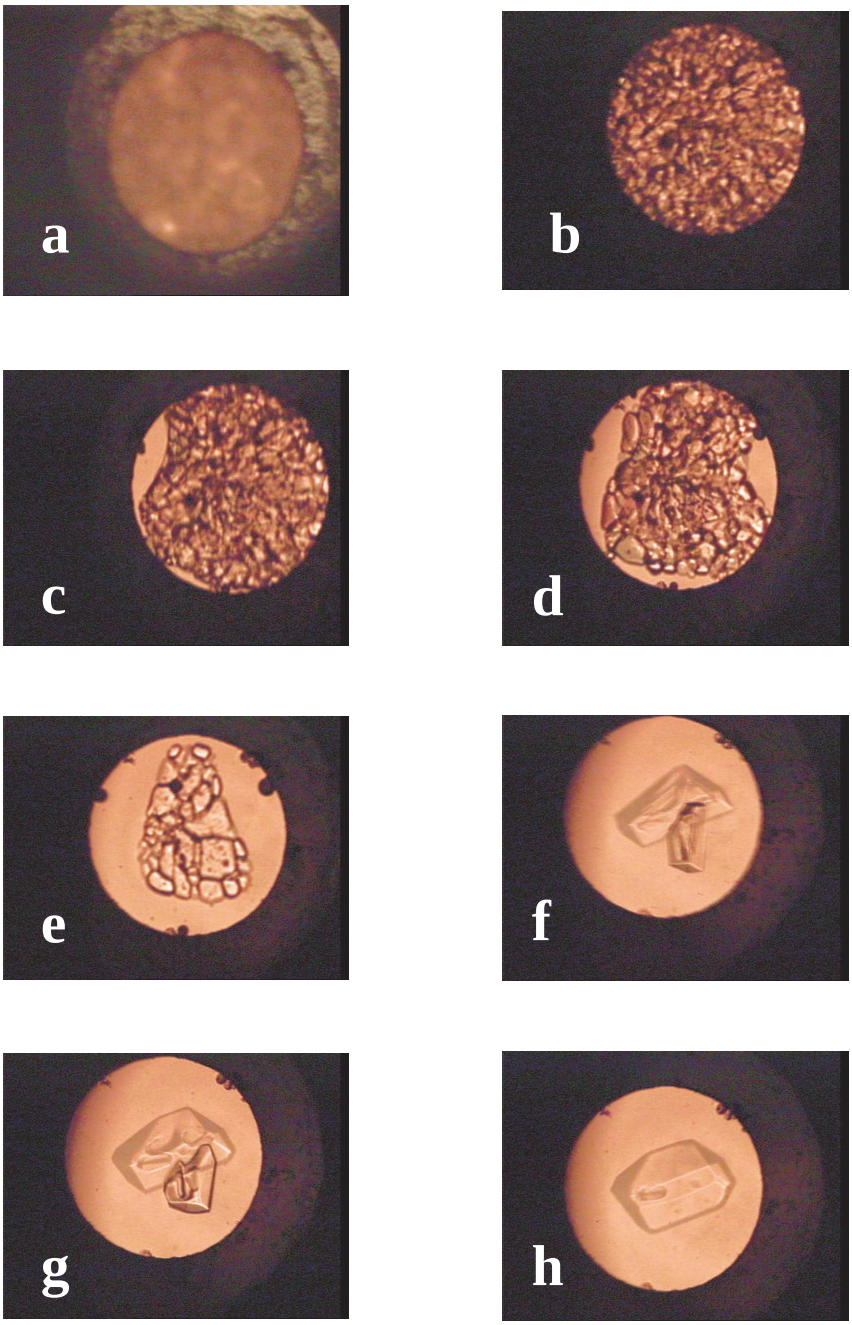

Figure 5.4: Formation of a single crystal of monoclinic sulfur on the melting line in the DAC. (a) Orthorhombic sulfur at ambient conditions, (b) Orthorhombic sulfur at 363 K and ambient pressure, (c,d,e,f,g,h) time-lapsed images on the formation of the monoclinic single crystal at 400 K and 0.03 GPa.

5.2.1 The stability of S_8 rings at low pressures

Orthorhombic and monoclinic sulfur are the two thermodynamically stable forms of sulfur at ambient pressure (monoclinic is the stable form at T > 371 K). In our reconstruction of the melting curve we have collected several optical data and XRD data.

During these measurements we have observed the formation of two different single crystals and their coexistence with the liquid. A sequence of photos showing the growth of a single crystal in the DAC is shown in figure 5.4.

One of this crystals (figure 5.4 and 5.5(b)) has been observed within the monoclinic stability regime (400 K and 0.03 GPa), while the other at higher pressure (448 K and 0.27 GPa), where we expect to observe orthorhombic sulfur [2]. The habits of the two crystals have been compared with the shapes of sulfur's crystals reported by Goldschmidt in his "Atlas der Kristallformen" [138], suggesting a correspondence with orthorhombic and monoclinic sulfur; figure 5.5(a) and 5.5(b) respectively.

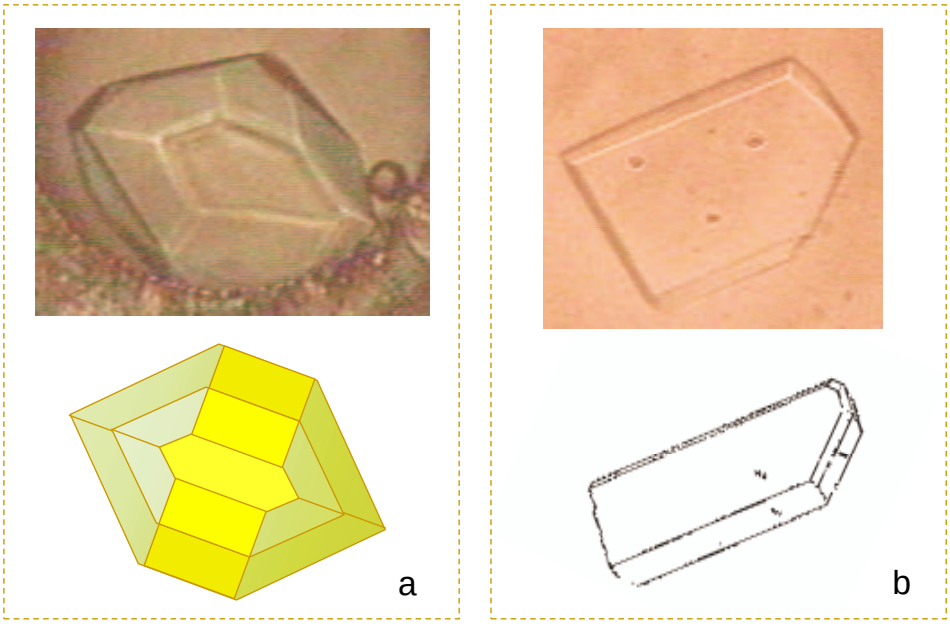

Figure 5.5: Top: the single crystals of orthorhombic (a) and monoclinic (b) sulfur synthesized in the DAC. The two crystals are in equilibrium with the liquid. Bottom: the shape of an orthorhombic and a monoclinic sulfur crystals from the "Atlas der Kristallformen" of Goldschmidt.

[2] Pressure and temperature have been cross-calibrated by measuring at the same time the shifts of the fluorescence peaks of ruby and strontium borate doped with samarium.

Along the melting curve, we assume there are not significant kinetic barriers. As a consequence, the coexistence of the liquid and the crystal should confirm that these phases, that have their own stability regime below the melting curve, actually correspond to thermodynamically stable phases.

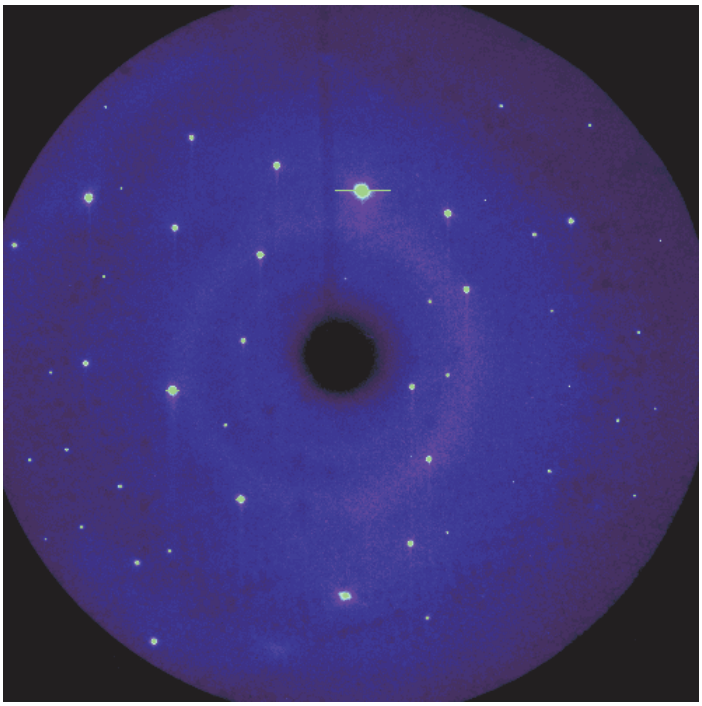

Figure 5.6: Single crystal diffraction pattern of the α-orthorhombic sulfur crystal grown in the DAC at 448 K and 0.27 GPa.

XRD data have been collected on the single crystal of figure 5.5(a). The corresponding 2D pattern has been shown in figure 5.6. The structure refinement confirms that the structure is *Fddd* orthorhombic, with the following refined cell parameters: a=10.51(6) Å, b=12.94(5) Å and c=24.6(2) Å. The calculated density is 1.92(3) g/cm^3 at 448 K and 0.27 GPa.

The stability regime of the β-monoclinic phase has been already determined by means of volume measurements by several authors ([139, 140] and references therein, figure 5.7). The single crystal shown in figure 5.5(b) has been observed within this thermodynamic range. We have also collected powder diffraction data (figure 5.8) using ID30's LVP.

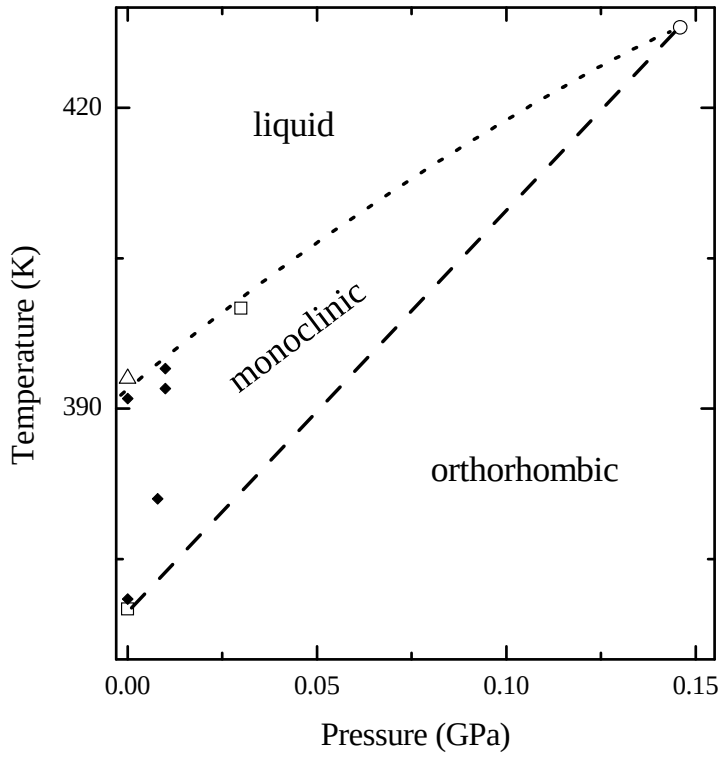

Figure 5.7: Stability regime of the β-monoclinic phase adapted from reference [139]. The open circle indicates the triple point reported in [139]; the black rhombuses indicate the data relative to the monoclinic phase; the open squares indicate the coexistence points between the orthorhombic and the monoclinic and the liquid and the monoclinic. The open triangle indicates the liquid.

The evolution of the diffraction patterns across the orthorhombic-monoclinic transition is shown in figure 5.8, where the experimental diffraction pattern have been plotted with the calculated patterns of the monoclinic and the orthorhombic phase. The plotted patterns, from the bottom to the top, corresponds to room temperature, 354 K, 364 K, 370 K, 370 K one half hour later, 381 K. The transition is slow, in all the plotted data (that have been collected within one hour) above 370 K we still observe a fraction of the orthorhombic phase. The pure monoclinic phase has been obtained only very close to the melting curve at 0.01 GPa and 392 K, where temperature and pressure have been cross-calibrated from the equations of state of BN and MgO [104]. The corresponding structure has $P2_1/c$ space group, the cell has been refined giving the following parameters: a=10.948(1) Å, b=10.943(1) Å and c=10.856(1) Å, and β=96.366(9)^o. The corresponding density is 1.977(2) g/cm^3.

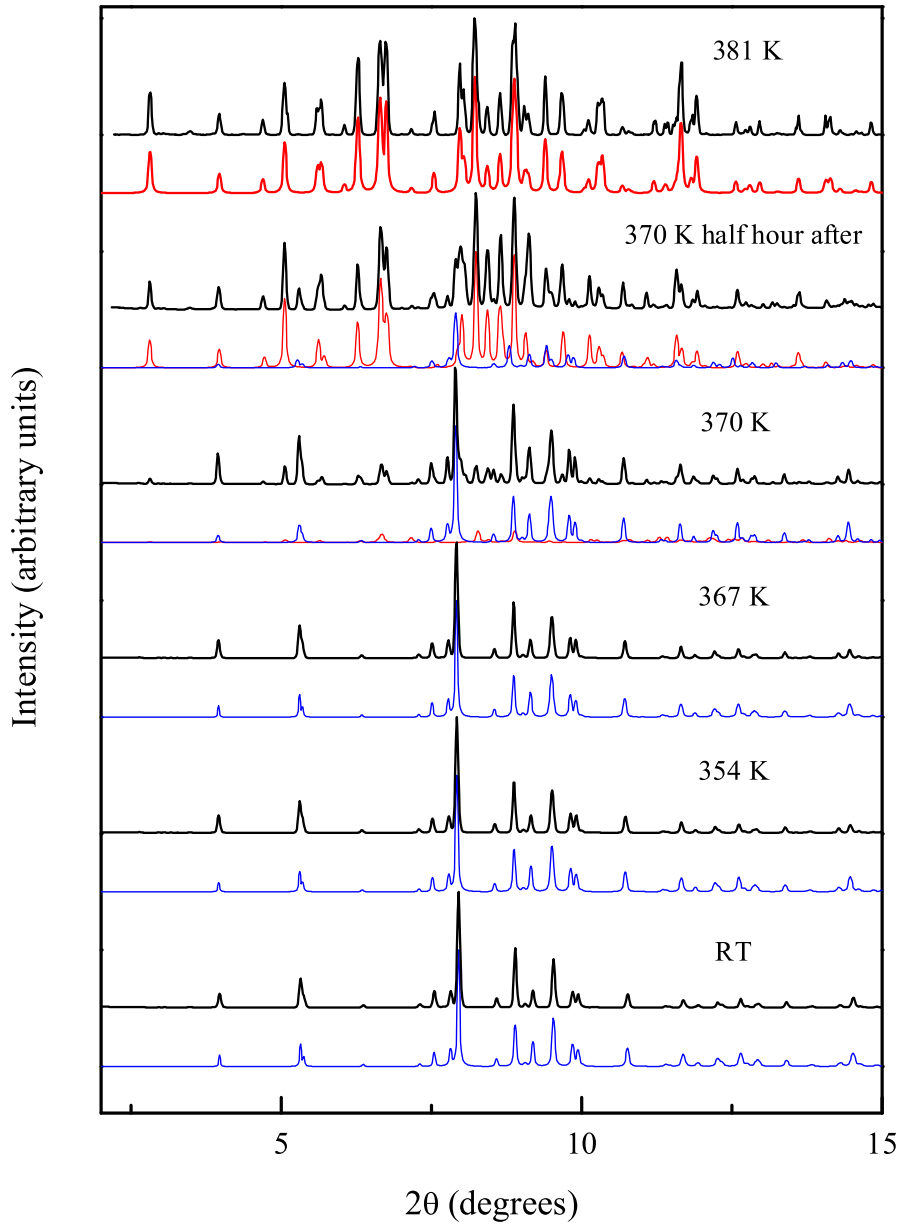

Figure 5.8: Evolution of the diffraction patterns going across the orthorhombic-monoclinic transition line. The patterns have been measured at ambient pressure; starting from the bottom to the top the corresponding temperatures are 273 K, 354 K, 364 K, 370 K, 381 K. The black line indicates the experimental data, the *blue* the fitting relative to the orthorhombic phase, and the *red* the fitting relative to the monoclinic phase.

The coexistence pattern of the monoclinic phase with the liquid has been also reported in figure 5.9.

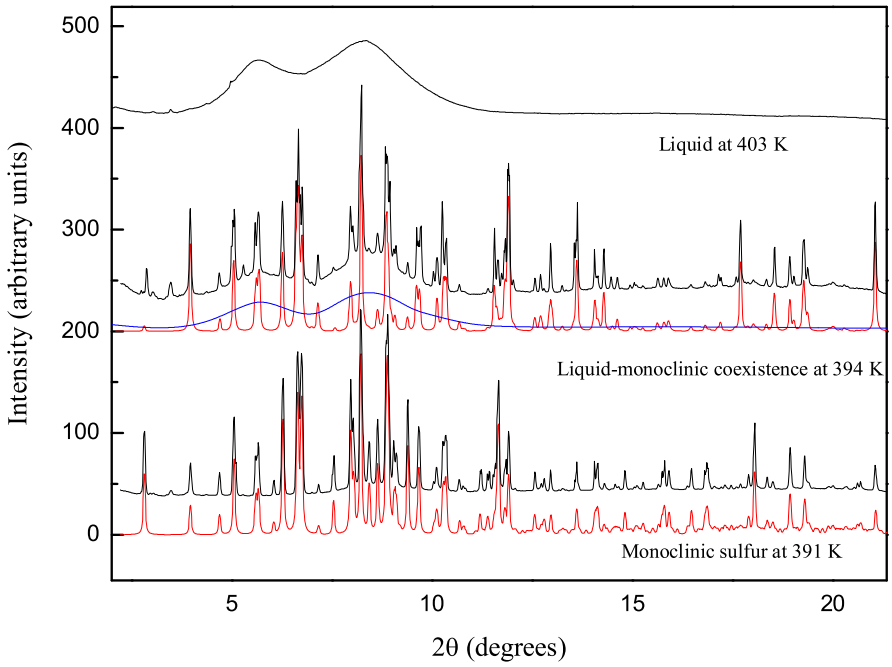

Figure 5.9: Diffraction patterns measured with the LVP close to the melting conditions of monoclinic sulfur at P = 0.01 GPa. The patterns are relative to the solid (bottom), to the solid liquid coexistence (middle), and to the liquid (top). The respective temperatures are 391 K, 394 K, and 403 K. Black lines correspond to experimental data, red to monoclinic calculated patterns, and the blue line indicates the liquid contribution to the coexistence pattern.

The slope of the monoclinic-orthorhombic transition at ambient pressure and 370 K, has been calculated by means of the Clapeyron equation (eq. 1.7) using the enthalpy variation, ΔH (0.096 kcal mol^{-1}, from ref. [141]) and the volume variation, ΔV (0.4254 cm^3 mol^{-1}), derived from the cell parameters of the orthorhombic and monoclinic structures. The transition does not involve changes in the molecular structure but just a different packing of the S_8 molecules; for that reason both the variations of enthalpy and volume are small. This slope is equal to 40.2(8) K/kbar, value that is in agreement with the literature one that is equal to 39 K/kbar [139, 140]. The value of the melting temperature T_m is also in good agreement with previous work. Indeed, we have obtained T_m = 394(3) K and T_m = 392 K in ref. [54].

5.2.2 The melting curve

In the second chapter, we have summarized the available literature relative to the measurements of the melting curve of sulfur, highlighting the discrepancies between the different available data. The construction of a reliable melting curve requires an accurate pressure-temperature measurements, and obviously, reproducible results.

We have measured the melting curve of sulfur by using the Paris-Edinburgh press (LVP). A few data points have been also measured using an high temperature DAC . In the observation of melting we have considered the following criteria:

1. *The solid-liquid coexistence points, indicated by the appearance of the broad liquid peaks under the crystalline pattern at melting (figure 5.9);*

2. *The absence of Bragg peaks from the diffraction patterns of sulfur (figure 5.9);*

3. *The visual observation of the solid-liquid equilibrium in the DAC (figure 5.4).*

Considering **1.** and **2.**, each occurrence of melting shall be constrained: a) by the pattern corresponding to the coexistence; b) by the two patterns below and above the melting (in absence of a coexistence point). In the first case the melting conditions are directly obtained from the pressure and the temperature at which the pattern has been measured; in the second case, pressure and temperature are averaged from the pressure-temperature conditions relative to the crystalline and liquid patterns.

In the LVP, BN has been used as internal pressure standard. In the DAC, pressure has been measured by measuring the shift of the ruby luminescence peak. In both cases, the temperature has been accurately measured by means of a thermocouple. In the LVP, it has been placed directly in the sample chamber (as described in chapter 3). In the DAC, the thermocouple has been used to measure the temperature close to the diamonds surface [3].

Our melting points have been plotted in figure 5.10 (yellow filled circles; the dashed line is a guideline for the eyes). The melting curve raises to a saddle point at around 2 GPa, above this pressure it follows a linear trend to 5 GPa with a slope $\Delta T/\Delta P$ that is equal to 71(2)^{o}C/GPa.

[3]The temperature error has been measured in a separate experiment by using the ruby luminescence peaks for the pressure calibration, and both a thermocouple and NaCl as internal standard. Considering the high thermal conductivity of diamonds, the finite equilibration time (typically one hour) imposed by the experiment is the principal source of error. The absolute error has been valued equal $\pm 2\%$.

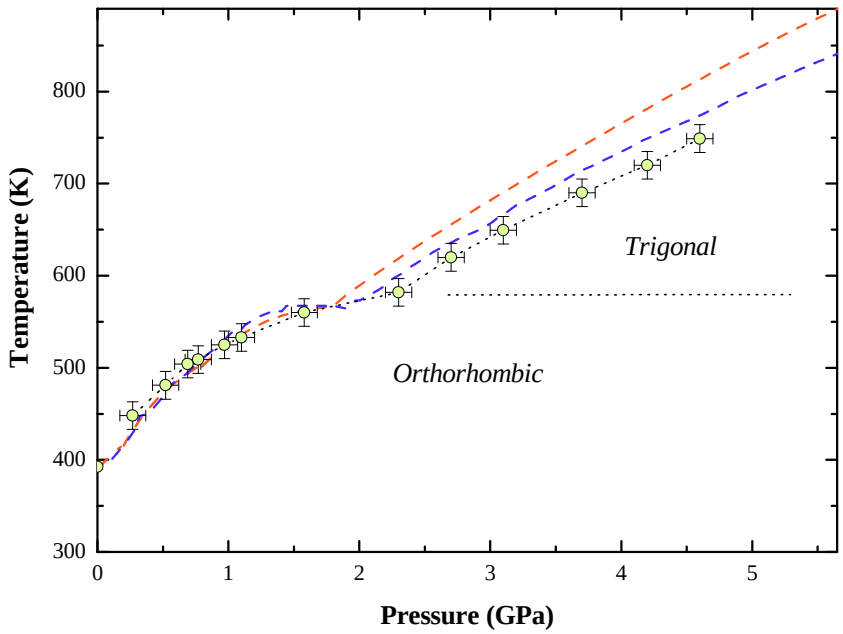

Figure 5.10: Comparison between the two melting curves measured by Susse *et al.* [31] (*red*), Paukov [30] (*blue*) and our experimental data (yellow circles). The error bars indicates the maximum error on our experimental points.

In figure 5.10, the melting curves proposed by Susse *et al.* [31] (red dashed line) and Paukov *et al.* [30] (blue dashed line) have been plotted in comparison with our data. The agreement between the three set of data is good in the pressure range up to 2 GPa and 580 K, while at higher pressures and temperatures our melting curve is shifted with respect to both the literature curves. The disagreement between the three set of data increases with pressure and temperature. Other than the errors that can arise from the different calibration procedures, we have to take into account that in constructing the melting curves of ref. [31] and [30] pressure have been determined *ex situ*. When DTA (Differential Thermal Analysis) measurements are conducted at high pressure conditions, a piston-cylinder device is used to generate pressure; the thermocouple is placed in contact to the sample, with an error on the temperature in the order of ± 4 K. Pressure is instead obtained from the room temperature calibration curves of the pressure device, with a consequent error that is temperature dependent. These temperature dependence can explain the shift between the DTA curves with respect to our data. Nonetheless, the agreement between the three curves (within the 5%) can be considered acceptable.

All the curves show an inflection around 2 GPa that can be associated with a triple point. Considering the data that we have collected on the solid in this area of the phase diagram (more details are reported in the following sections), we conclude that this point corresponds to the equilibrium between the liquid, the orthorhombic and the trigonal polymeric phase recently reported by Crichton *et al.* [23] (see chapter 2). Unfortunately, this triple coexistence has not been observed directly. However, from our data we find the triple point likely located at 2.3 GPa and 577 K, with the reported triple points of ref [31] and [30] located respectively at 1.9 and 2 GPa, and 565 K.

5.2.3 Orthorhombic-Trigonal transformation: effect of kinetics.

In order to determine the transition line between the orthorhombic and the trigonal phase, we have performed *in situ* XRD measurements at different pressures and temperatures.

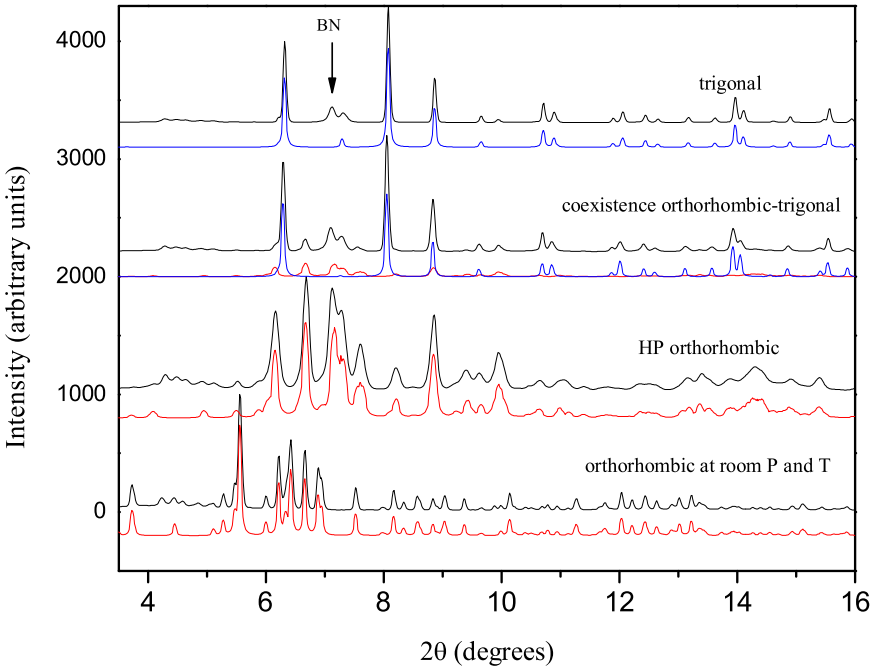

Figure 5.11: Evolution of the diffraction patterns across the orthorhombic-monoclinic transformation line. The orthorhombic patterns are relative to ambient conditions and 5.7 GPa - 300 K; the coexistence has been observed at 6.8 GPa - 600 K, and the trigonal phase at 6.9 GPa - 610 K (red and blue lines correspond to the orthorhombic and trigonal calculated patterns).

The measurements have been conducted using the DAC and LVP with the same pressure-temperature calibration system previously used for the construction of the melting curve. A typical sequence of diffraction patterns measured during the transformation in the LVP, is presented in figure 5.11.

At high temperature, close to the triple point at 2.3 GPa and 577 K, the transition has been observed to be reversible. If instead, the pressure on the sample is released after cooling to room temperature, fibrous sulfur with traces of S_8 is formed at 0.5 GPa [23]. The diffraction pattern of fibrous sulfur after recovery, is reported in figure 5.12.

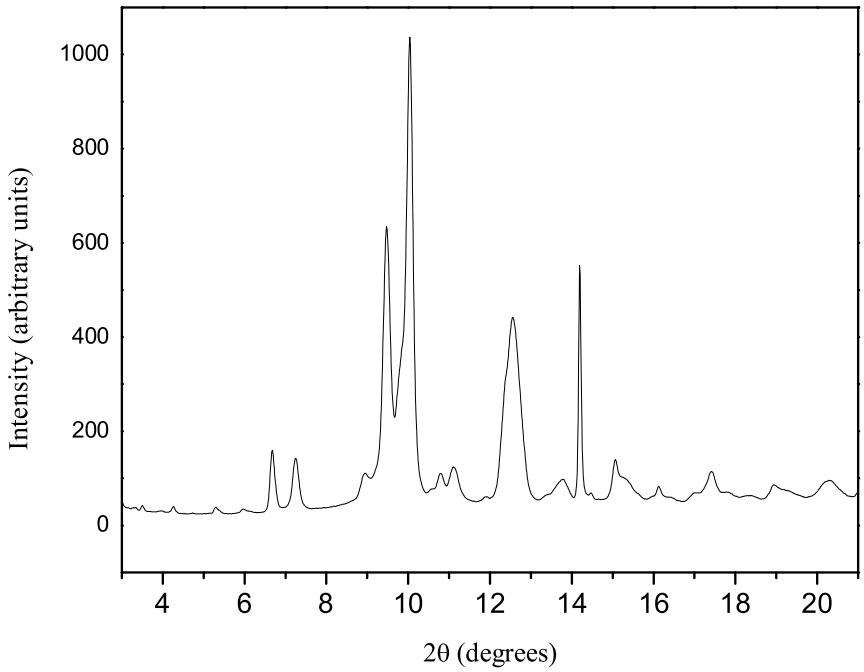

Figure 5.12: Diffraction pattern of fibrous sulfur at ambient conditions after cooling and decompression of trigonal sulfur.

For that reason several runs have been carried out in order to measure the orthorhombic-trigonal transition line. The transition line derived from the coexistence points is shown in figure 5.13. The line is practically horizontal: up to 11 GPa, independently of the applied pressure the transformation is observed at about 580 $\pm$ 20 K.

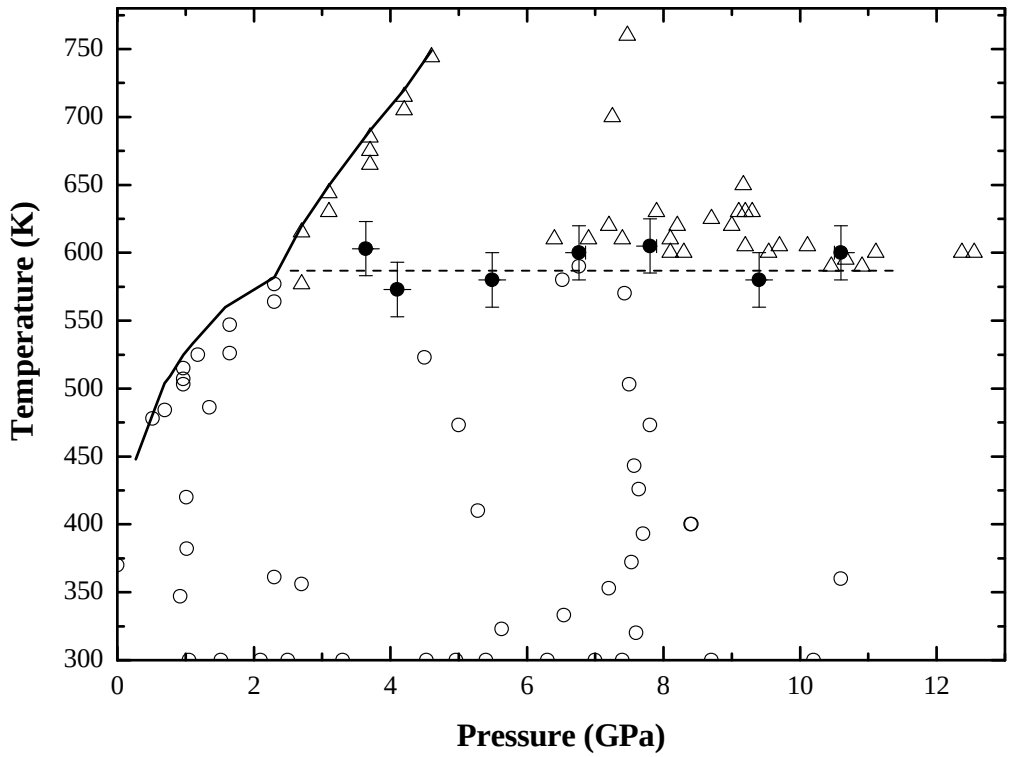

Figure 5.13: Experimental points relative to the orthorhombic-trigonal transition. Open circles and open triangles indicate respectively orthorhombic and trigonal sulfur; the full circles correspond to the observed coexistence points. The transformation is observed at the constant temperature 580 ± 20 K. The melting curve is the one reported in figure 5.10.

We also have collected several Raman spectra in the solid region between 0 and 5 GPa. The 514.5 nm line of an argon-krypton laser was used as excitation line. An average power of 2 mW on the sample was chosen in order to avoid any thermal effect. Raman spectra were taken with increasing pressure at ambient temperature up to 2.8 GPa. From the wavelength-pressure diagram reported in figure 5.1, we expect to observe the orthorhombic phase. The spectrum corresponding to these conditions is reported in figure 5.14 (b). Among the 48 expected Raman active bands for orthorhombic sulfur, 24 modes are observed in agreement with previous works of Zallen [142] and Wang *et al.* [143]. We have then gradually increased the temperature of the sample up to 629 K whilst maintaining the pressure between 3 and 4 GPa. The Raman spectra, up to 565 K and 3.5 GPa, are still representative of the S_8 molecular phase without any striking spectral modification apart from the expected pressure-shifts and gradual broadening of peaks due to temperature (figure 5.14 (c)).

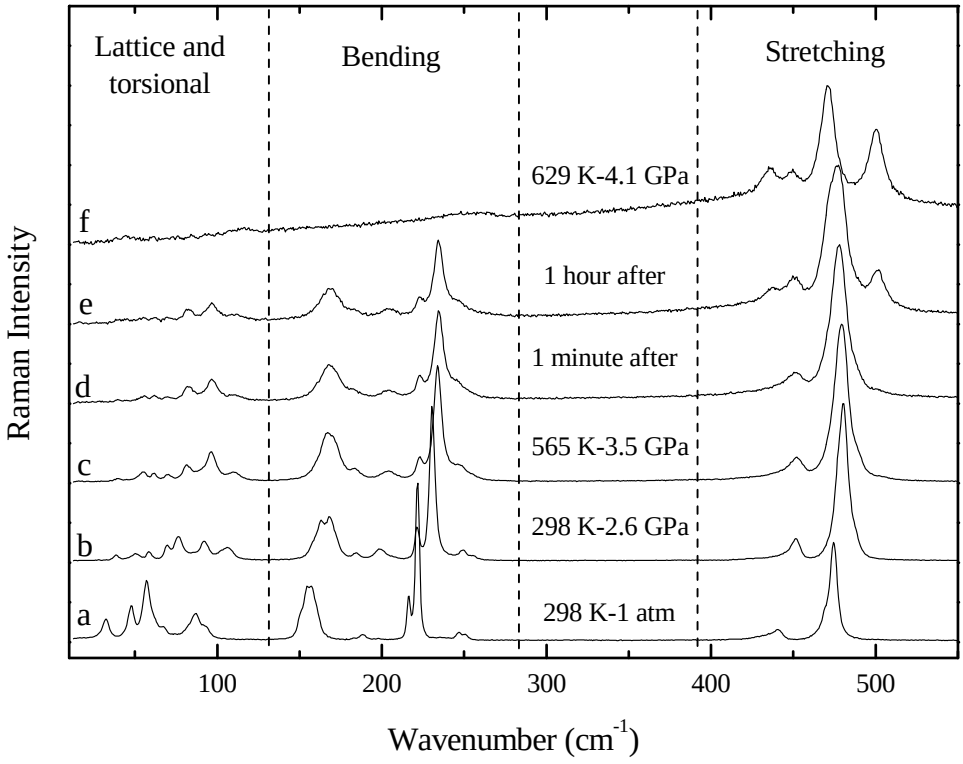

Figure 5.14: Raman spectra of sulfur at different thermodynamic conditions. (a) Orthorhombic sulfur at ambient conditions, (b) orthorhombic sulfur at room temperature and 2.6 GPa, (c,d,e) evolution of the spectra during the orthorhombic-*p*-*S* transition at 565 K and 3.5 GPa, (f) trigonal sulfur at 629 K and 4.1 GPa.

However, after one minute (which corresponds to the acquisition time of the first Raman spectrum at this temperature and pressure), we observed a gradual modification of the Raman spectrum (figure 5.14 (d)) under the laser illumination with a progressive appearance of two new peaks in the high wavenumber region (peaks at 437 and 500 cm^{-1} in figure 5.14 (e)). The Raman spectrum taken at 629 K and 4.1 GPa (figure 5.14 (f)), is characterized by four intense bands located at 435, 449, 470 and 500 cm^{-1} and three rather broad and less intense bands located at 45, 115 and 260 cm^{-1}. The peaks in the 130-300 cm^{-1} region are instead disappeared.

In the region principally associated with bending vibration modes, 130-300 cm^{-1}, both the S_8 and the S_6 molecules present well-defined sharp lines [53]. The bending lines are instead weaker or vanish in the background, when we deal with polymeric structures [82,125]. As a consequence, the presence or disappearance of the strong lines in this region, could be considered as an indication of the molecular or polymeric nature of the considered sample.

The region around 400-500 cm^{-1} is representative of the stretching vibration modes that are common to both the molecular and the polymeric species. Comparing the mode frequencies of *p-S* phase reported by Eckert *et al.* [131] and Nagata *et al.* [130] extrapolated at P=0 GPa, with the positions of our stretching spectral lines at 629 K and 4.1 GPa (table 5.2), we conclude that our spectrum is characteristic of *p-S*.

ν_o (cm^{-1}) [131]	ν_o (cm^{-1}) [130]	ν (cm^{-1}) our data
437	440	435
444	not seen	449
476	475	470
496	500	500

Table 5.2: Stretching mode frequencies of *p-S* phase extrapolated to P=0 GPa by Eckert *et al.* [131], by Nagata *et al.* [131] and our data at 629 K and 4.1 GPa.

It is important to point out that the transition from S_8 to *p-S* that we have observed by Raman spectroscopy is not photo-induced. This is because it has been observed at a lower pressure with respect to the laser-energy used (line 515 nm in figure 5.1), and because it has been observed at around 565 K, concurrent with the diffraction measurements. That means that there is a correspondence between the trigonal polymeric phase of sulfur observed by X-ray diffraction and the p-S polymeric phase observed by Raman spectroscopy.

We have interpreted these results as experimental evidence of a kinetic barrier associated to the orthorhombic-trigonal transformation. This kinetic barrier can be overcome by increasing the temperature or, by a suitable laser illumination. The critical step of the S_8-polymer transformation is the breakdown of the S_8 molecules: it has been shown in fact, that the role of the laser illumination is, in a first step, the opening of the rings [82].

5.2.4 Rhombohedral S_6: a new HP-HT polymorph.

The existence of an high pressure phase based on S_6 molecular units, can be considered the missing link between the Raman and the diffraction experiments. Behind the correspondence of trigonal and *p-S*, the existence of S_6 molecules confirms the correlation between the phases observed with Raman spectroscopy and the phase diagram of sulfur. This high pressure phase, never detected by diffraction experiments at room

temperature, could be one of the phases observed at high temperature by Kusaba and Kikegawa [135].

Our diffraction measurements, conducted first with the LVP, and repeated with a high temperature DAC, extend between 0 and 15 GPa and between 300 and 1000 K [4]. In the LVP a phase transition to a new phase and the stability domain of this phase have been detected. In the DAC, the new phase has been synthesized as a single crystal.

Rietveld refinement of the powder diffraction pattern of this new phase, taken at 7.2 GPa and 950 K (figure 5.15), confirms $R\bar{3}$ symmetry (a=10.1508(5) Å and c=3.6756(2) Å) with 18 atoms per unit cell organized in three S_6 ring molecules with S located on the *6c* positions with x=0.17581(5), y=0.19250(5) and z=0.15027(5), and a calculated density of 2.922(1) g/cm^3. The single S-S bond length is 2.1762(1) Å and the torsion angle is 78.89(2) ^{o} (figure 5.16) [144].

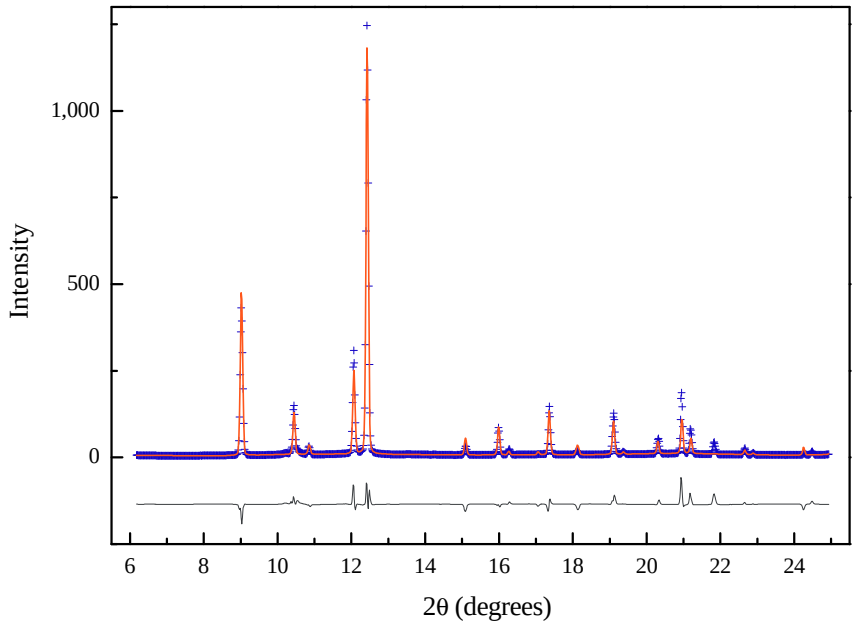

Figure 5.15: Diffraction pattern of the S_6 rhombohedral phase. Refinement results on the diffraction pattern obtained from in-situ measurements at 7.2 GPa and 950 K; the data are represented by blue crosses, the red line corresponds to the Rietveld refinement and the black line beneath these, the difference between the observed and calculated data.

[4]The pressure-temperature calibration has been carried out with the use of two internal standards, MgO and BN, in the LVP, while NaCl, the ruby and the samarium doped SrB_4O_7 (SrB_4O_7:Sm^{2+}) fluorescence in the DAC.

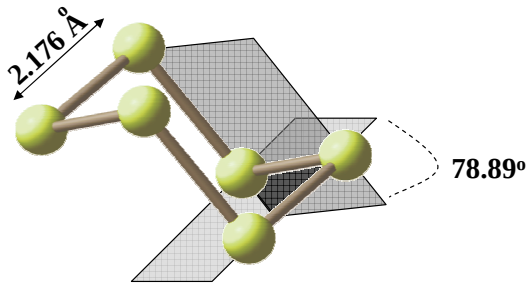

Figure 5.16: Geometry of the S_6 molecule. The parameters refer to the fitting at 7.2 GPa and 950 K.

The occurrence of this phase in this thermodynamic regime is new; however, the phase itself is not. A hexameric cyclic form of solid sulfur has been known since its first synthesis by Engel in 1891 but it has only been prepared via chemical methods at room pressure [56, 57]. The study of this molecule, variously called Engel's sulfur, S_ε, S_ϱ, S_φ, trigonal sulfur, and rhombohedral sulfur has attracted a lot of interest because it is a constituent of gaseous and liquid sulfur [21, 145]. In 1978, Steidel *et al.* [58] unambiguously determined its molecular and crystal structure at 183 K, due to its rapid decomposition at room temperature. The structural refinement by Steidel *et al.* has shown that three S_6 rings in the chair conformation fill the $R\bar{3}$ trigonal unit cell and the corresponding cell parameters are a=10.766(4) Å and c=4.225(1) Å. At 183 K, the S_6 molecule is characterized by a bond length of 2.068(2) Å and a torsion angle of 73.8(1)^o. All these structural parameters are in good agreement with a large number of theoretical calculations [78, 146, 147] that also suggest the chair as the more stable conformation.

Considering the effect of compression on the cell parameters and the reassessment of the molecular structure we conclude that the structure observed at 7.2 GPa and 950 K, and the structure of cyclohexasulfur chemically prepared by Engel are the same. Despite this is not a new phase, this is the first time that a sulfur polymorph previously prepared by chemical reaction, metastable at ambient conditions is directly formed by increasing temperature and pressure of the pure element, and clearly indicates the reason why the metastable S_6 rapidly decomposes at ambient conditions.

In our mapping of the phase diagram we have defined also the stability regime of the S_6 molecular structure through the observation of points of coexistence along the univariant with the trigonal phase (figure 5.17 (a)), and with the higher pressure

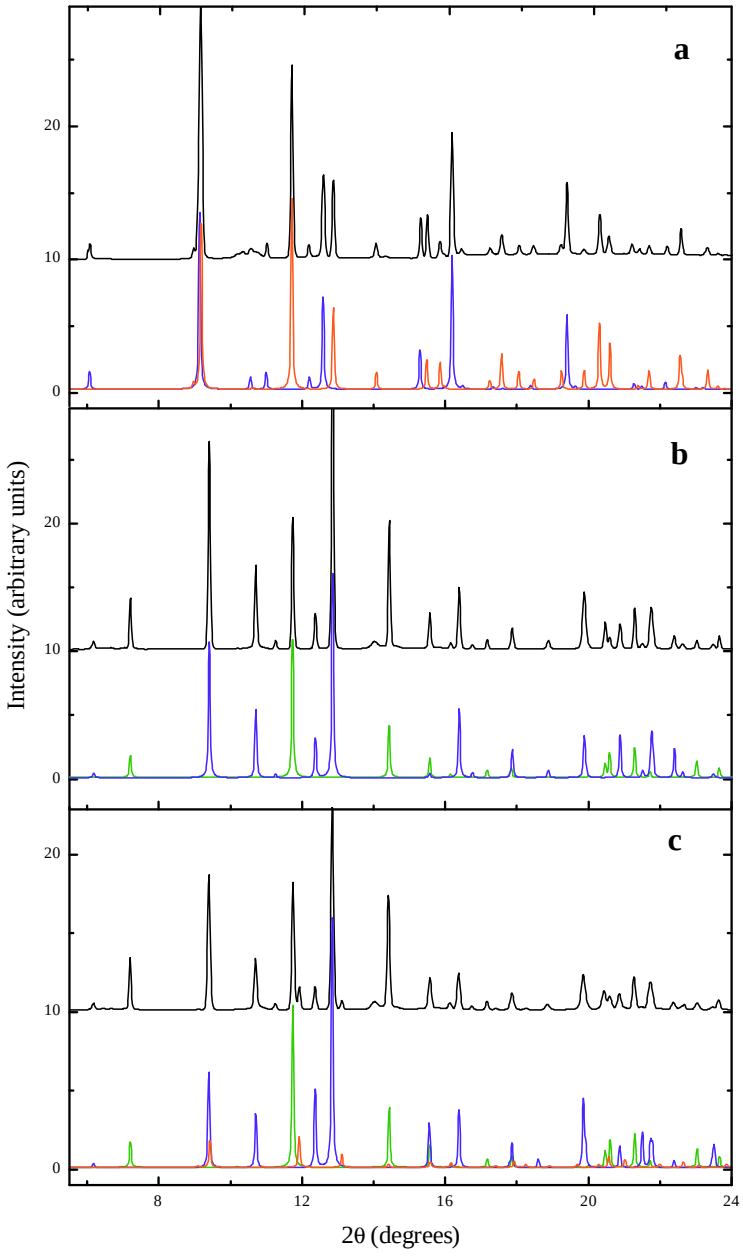

Figure 5.17: - Diffraction patterns corresponding to the triple and coexistence points around the stability regime of the S_6 phase. Comparison between calculated (blue lines indicate the S_6 phase, red lines the trigonal one and green lines the tetragonal one) and experimental patterns relative to: (a) coexistence point between the S_6 and the trigonal phases, (b) coexistence point between S_6 and the tetragonal phases, (c) the triple point corresponding to the trigonal, the S_6 and the tetragonal phases.

tetragonal phase (figure 5.17 (b)). We report also in figure 5.17 (c) the diffraction pattern relative to the triple point (10.7 GPa and 650 K) corresponding to the trigonal-rhombohedral-tetragonal phases. The densities relative to the three phases at the triple point are 3.116 g/cm^3 for the trigonal, 3.196 g/cm^3 for the rhombohedral and 3.284 g/cm^3 for the tetragonal phase.

The existence of this triple point is important because, it unambiguously demonstrates that the S_6 molecular phase can be observed directly, only at high temperature. The high temperature stability regime of S_6 is the reason why it has not been observed by the X-ray diffraction experiments conducted at room temperature and high pressure [135, 136].

5.3 Liquid Polymorphism

The nature of the polymorphism in the solid suggests some questions on the polymorphism in the liquid. In particular, if the sequence of transformations observed in the solid can be observed also in the liquid. From our study of the solid phases we can distinguish two parallel behavior of sulfur with increasing pressure, in correspondence to the ambient or the high temperature regime. Orthorhombic sulfur transforms directly to tetragonal at ambient temperature and 36 GPa or transforms respectively to the trigonal polymer [23], rhombohedral S_6 [144], and finally tetragonal [45, 46] at higher temperature and in the pressure range up to 15 GPa. We could expect that the liquid behavior is correlated to the high temperature polymorphism of the solid. So that in the liquid, as in the solid, we could observe the presence of several molecular-polymer transitions or the presence of mixed phases in determined pressure-temperature ranges. Actually this correspondence has been already partially observed in the liquid at low pressure (less then 0.085 GPa), where the λ-transition corresponds to the initiation of a polymerization process [74, 75]. The polymerization is in fact characterized by the formation of a small quantity of long polymer chains at 159^{o}C and 1 atm, this fraction increases with temperature. This transition has been widely studied *in situ* by neutron and x-ray diffraction [72–75,148], different spectroscopies [83,84,126,149,150] as well as by various *ex situ* techniques [21] (the state-of-the-art in the study of liquid sulfur has been summarized at the end of the second chapter).

What happens in the liquid if we increase the pressure?

Unfortunately, in the literature on the high pressure liquid domain of sulfur there are no structural studies, despite that optical and electrical measurements indicate the potential for liquid-liquid phase transitions [4, 5, 151].

By looking the solid behavior, we expect that, at a determined pressure, the liquid becomes purely polymeric. We could also expect to observe some aspect of the sequence: S_8-polymer-S_6-polymer in the liquid, like in the solid.

Obviously such a kind of study needs in-situ measurements: we have used *in situ* XRD and Raman spectroscopy to characterize sulfur liquid at high pressure and temperature.

XRD measurements on liquid sulfur have been conducted using both the LVP and the DAC. Raman measurements have been also conducted using a DAC. The different thermodynamic paths that have been followed are presented in figure 5.18. The results obtained are detailed in the following sections.

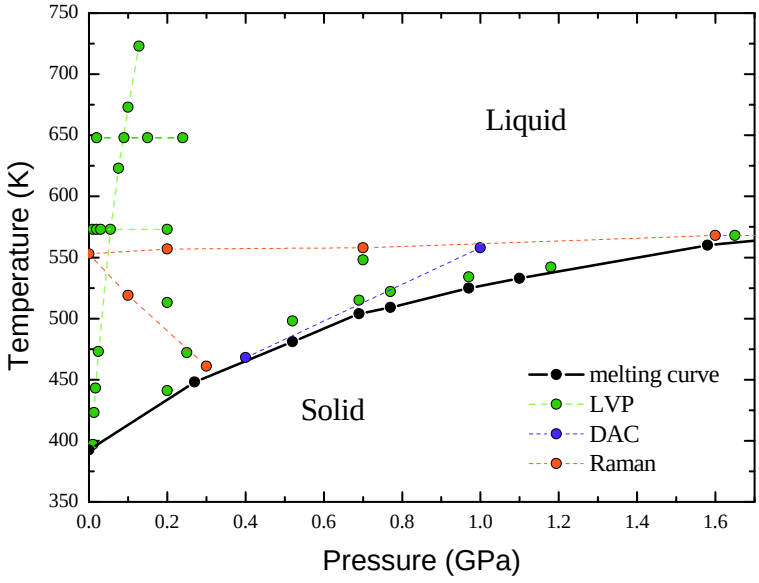

Figure 5.18: Thermodynamical paths followed in the study of the liquid, performing XRD with the LVP (green) and the DAC (blue), and Raman spectroscopy again in the DAC (red).

5.3.1 The liquid above the λ-transition

The λ-transition in liquid sulfur has been the subject of an intensive research because it represents clear evidence of polymorphism in an elemental liquid. The liquid immediately above the melting point at ambient pressure is purely molecular. The increase of the temperature, is accompanied by deep changes in the physical properties; so that, for example, in correspondence to the λ-transition, we observe a sharp change in the viscosity of liquid sulfur (figure 5.19, [22]).

These effects on the physical properties reflect changes in the structure of the liquid: indeed, at 159^{o}C we observe the formation of a small fraction of long polymer

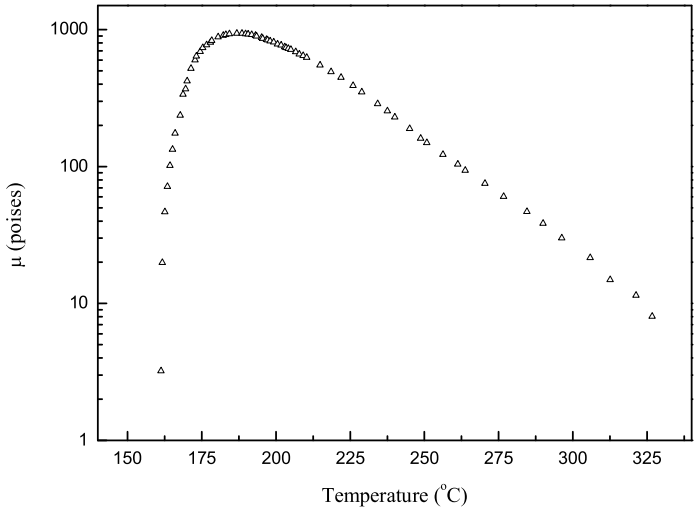

Figure 5.19: Viscosity of liquid sulfur above the λ-transition. The graph is a semi-log graph.

chains in the molecular liquid. By further increasing the temperature the polymeric fraction increases, reaching a plateau at around 230-240^{o}C. The maximum chain-length is reached at around 180^{o}C [54] and thereupon decreases continuously as the temperature is increased [152], coincident with the increase in the small molecule fraction (S_6 or S_7) [85]. The presence of several molecular and polymeric forms in the same liquid makes it difficult to obtain suitable structural information with a unique technique. As a consequence, the complementary use of the information coming from different techniques becomes needful in composite liquids. This is the reason why in this thesis several diffraction, Raman spectroscopy and inelastic scattering (see next chapter) data have been collected on liquid sulfur.

Despite several diffraction studies have been already conducted on liquid sulfur at ambient pressure [72–75, 148], we have performed a detailed X-ray diffraction study raising the temperature up to the limit of the liquid domain. This is because we are interested above all in the changes of the structure factor of the liquid above the λ-transition that corresponds to the maximum of the viscosity.

Previous calculations on the structure factor of liquid sulfur show that the S-S-S unit is only slightly different in the annealed and in the polymeric structures [77]. This is reasonable considering that in both these kind of structures sulfur forms two sigma bonds and it has two couples of electrons delocalized on two sp_3 orbitals that impose

a pseudo-tetrahedral angle in the different structures (in the solid phases this angle is 107-108^o for orthorhombic and monoclinic S_8 rings, 102-103^o for trigonal chains, 103^o for S_6 rings and 101^o for tetragonal chains). In all these structures the S-S-S unit varies slightly; therefore, only a small variation in the liquid structure factor S(Q) is observable. Calculations performed on the structure factor of liquid sulfur starting from molecules and/or polymeric chains show, in fact, that most of the structural information associated with a transition is contained in the first peaks of the structure factor [77]. These peaks contain the information on the packing of the molecules/chains, and on the structural details that distinguish the S_8, S_6 rings from the chains; that is the conformation of the S-S-S-S-... units. This information is contained in the low-Q range (less than 4-6 Å^{-1}, from the third shell of coordination on). It is for that reason that in the planning of our experiments we preferred to have a short Q-range with a better resolution on the first peaks (wavelength, λ, equal to 0.53394 or 0.3738 Å). However, an extended Q-range is important for the extraction of the structure factor from the raw data. The classic structure factor extraction is in fact carried out by applying the equation:

$$S(Q) = \frac{I_c(Q) \; - a\, C(Q)}{a\, F(Q)} \tag{5.1}$$

where I_c(Q) is the intensity corrected for the sample environment contribution, F(Q) represents the square of sulfur atomic form factor *f(Q)*, C(Q) represents the Compton scattering and *a* is a constant. Apart of a series of corrections that have to be applied to the raw data in order to obtain I_c(Q) from I(Q)[5], a short Q-range causes problems in the determination of the constant *a*. This constant is generally obtained by scaling the intensity, I_o(Q), on the function F(Q) in the high Q region, where the oscillations of the structure factor are weak. Actually, our Q-range is too short to perform this normalization. In order to overcome this problem we have firstly measured the diffraction pattern of liquid sulfur at ambient pressure and 150^{o}C where the structure factor has been accordingly measured by several authors with different diffraction techniques [72–75, 148]. The constant *a* necessary to the extraction of the structure factor has been then determined by scaling our data to the reference data [72]. The constant *a* has been used for the extraction of all the others structure factors measured in the same run.

[5]The contribution of the sample environment has to be subtracted, and the I(Q) has to be normalized using a Q-function that takes in account the angular dependence introduced by the presence of the Soller's slits.

For the experiment, the LVP has been used for measuring the temperature evolution of the structure factor at low pressure. The temperature has been measured by means of a thermocouple and pressure has been measured through the BN's equation of state.

The temperature evolution of the structure factor has been measured from 150^{o}C up to 450^{o}C (the pressure varies from 0.01 to 0.1 GPa). The obtained patterns are shown in figure 5.20.

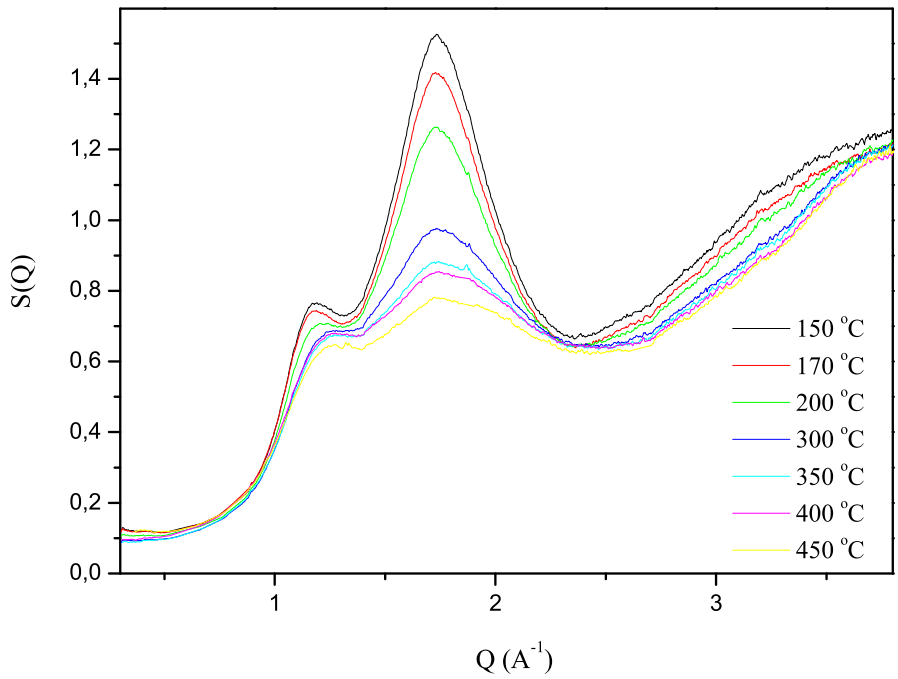

Figure 5.20: Evolution of the structure factor of liquid sulfur with temperature: effect on the first peaks. The exact thermodynamic conditions are: 150^{o}C, 0.013 GPa; 170^{o}C, 0.017 GPa; 200^{o}C, 0.024 GPa; 300^{o}C, 0.055 GPa; 350^{o}C, 0.076 GPa; 400^{o}C, 0.1 GPa; 450^{o}C, 0.128 GPa.

As noticed above the structure factor corresponding to the first peaks changes significatively with temperature. There is a diminution of the intensity of the peak at 1.7 Å^{-1} respect to the intensity of the one at 1.1 Å^{-1}. We have hypothesized that there is a correlation between the area of these peaks and the fraction of polymer and molecules S_8 in the liquid. Actually, we know that the polymer fraction increases when the temperature is increased: as a consequence, if these first two peaks, in such way, are related to the molecule and the polymer, we can assume that the area of the second peak has

to be related to the concentration of the molecules S_8 that diminish with increasing the temperature.

In order to check the existence of this correlation we have normalized the structure factors subtracting a constant baseline (figure 5.21).

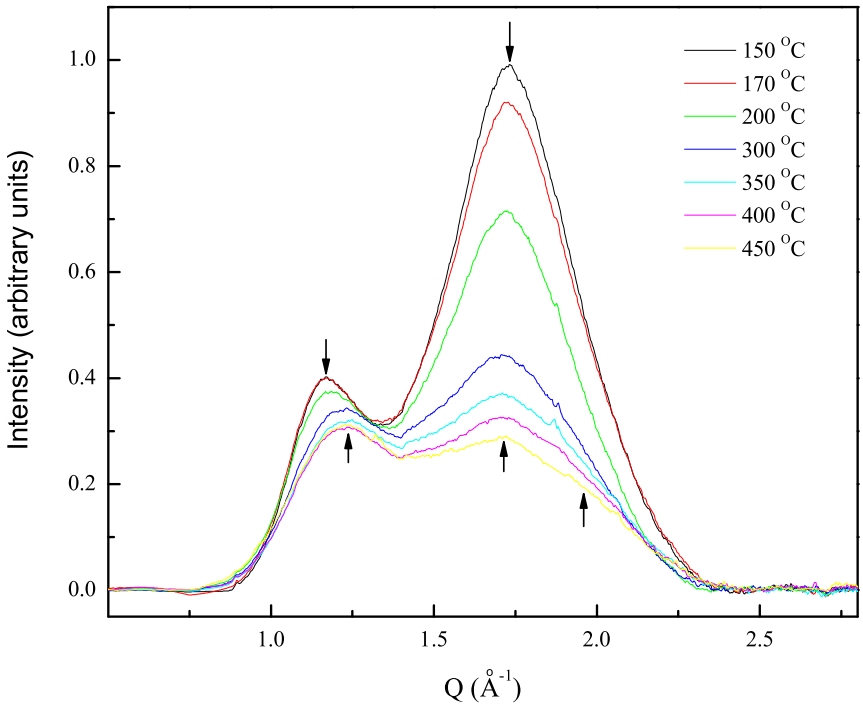

Figure 5.21: Plot of the structure factor of liquid sulfur with temperature after the substraction of a baseline. Between 200^{o}C and 300^{o}C the minimum shifts and the appearance of at least one new peak is observed.

This plotting evidences not only the relative variation in the peaks intensity, but also: i) between 200^{o}C and 300^{o}C, a global shift of the peaks and of the minimum at 1.3-1.4 Å^{-1} and, ii) above 300^{o}C, the appearance of new peaks under the curves.

We have hypothesized that the peak at 1.7 Å^{-1} contains exclusively the structural information on the molecule S_8. This assumption implies that the diminution of this peak area is related to the variations in the composition of the liquid. By following this hypothesis, the molecular, ϕ_m, and the polymeric, ϕ_p, fraction can be calculated as:

$$\phi_m = \frac{A_t}{A_o} \tag{5.2}$$

$$\phi_p = 1 - \frac{A_t}{A_o} \tag{5.3}$$

where A_o is the area of the peak measured under conditions that correspond to the purely molecular liquid ($\phi_m = 1$), while A_t represents the area of the peak above the λ-transition, where the liquid is supposed to be formed by both molecular and polymeric species. The areas A_o and A_t have been derived from the structure factors reported in figure 5.21 by integration. The area A_o has been obtained from the data at 150^{o}C, below the λ-transition, where the liquid is supposed to be purely molecular.

In the figure 5.22 we report the polymeric extent measured by Koh *et al.* [153] and the polymeric extent, ϕ_p that we have calculated from the area diminution of the second peak. Actually the agreement is good up to 200^{o}C. Above this temperature the appearance of new features in this Q-region degrades the model. Nonetheless, the agreement with the literature data is qualitatively good.

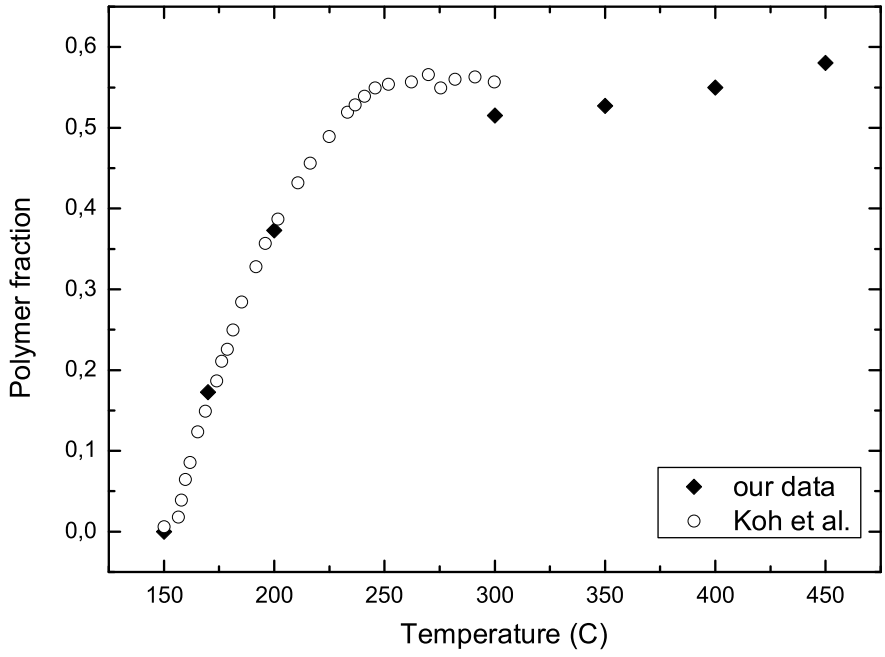

Figure 5.22: Polymer fraction in liquid sulfur calculated from the intensity diminution of the second peak in figure 5.20 (black rhombuses). The open circles indicate the data from ref. [153].

To have a better idea of the region between 200^{o}C and 300^{o}C, the same normalization applied to our data has been applied to the data reported in ref. [72]. These authors

have performed a fine temperature scan between 130^{o}C and 300^{o}C in a wide Q-range (the full structure factors have been reported in the second chapter, figure 2.11). The normalized data are plotted in figure 5.23.

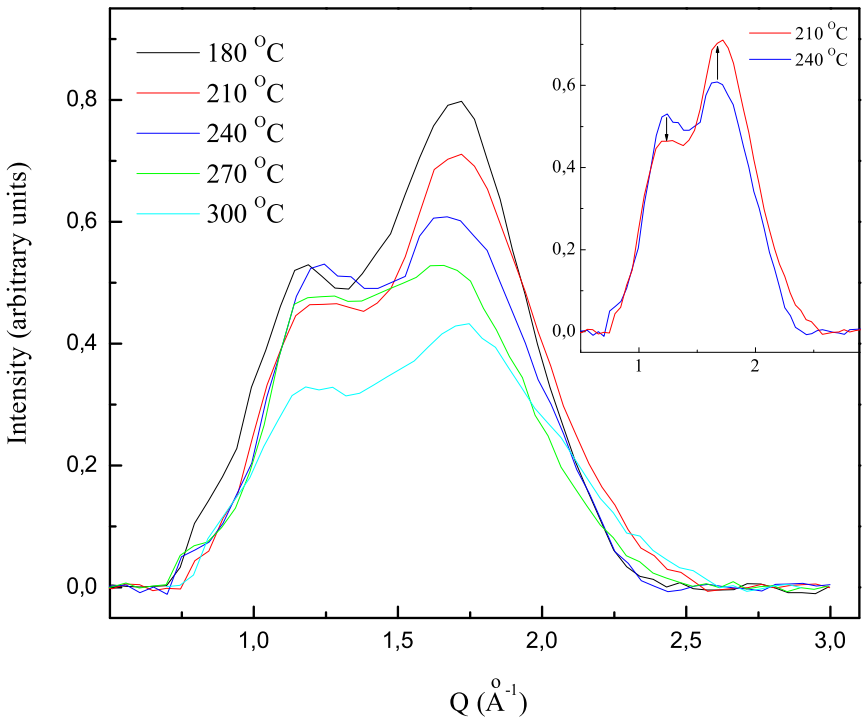

Figure 5.23: The first peaks of the structure factor of liquid sulfur reported in ref. [72] after substraction of a baseline. An inversion in the direction of the intensity increase of the first two peaks is observed between 210^{o}C and 240^{o}C (insert).

From figure 5.23 we observe the main changes between 210^{o}C and 240^{o}C. In between these two temperatures we observe in fact, an inversion in the direction of the intensity increase of the first and the second peak of the structure factor.

A transition around this temperature had been observed by means of electrical measurements by Vezzoli [3, 4, 154] in 1969. More or less at this temperature the polymer reach its maximum concentration, the changes in the liquid could be then related to the breakdown of the long polymeric chains formed above the λ-transition accompanied by the formation of different molecular species, that have been revealed in the high-temperature liquid by different techniques (see [21] for a detailed review). This

hypothesis is supported by the following experimental evidences:

After the jump associated to the λ-transition, the viscosity of liquid sulfur decreases continuously following the fragmentation of the long polymer chains.

At ambient pressure, sulfur evaporates at 445°C, above this temperature short fragments (S_4) and cyclic molecular species characterizes the sulfur vapor.

The heterogeneous character of liquid sulfur at these thermodynamic conditions makes its modeling difficult and, as a consequence, the interpretation of several experimental results. On the other side this heterogeneity explains the large number of quench recovery products that have been obtained from the different liquids at different thermodynamic conditions. For an accurate study of a liquid, other than the performance of *in situ* measurements, the chosen technique (when this is realizable) should be able to distinguish between the different local structures present in the liquid.

5.3.2 The pressure-induced polymerization in the liquid

In order to follow the changes induced in the liquid by compression, a parallel Raman-XRD study has been conducted on the liquid under pressure. If the temperature does not exceed 300°C, the liquid at ambient pressure is mostly composed by S_8 molecules and polymeric chains. Above 0.085 GPa, sulfur melts directly into a molecular-polymeric liquid [155]. Considering the sequence of transformations in the solid, and in particular, the orthorhombic-trigonal transition, pressure should induce the complete rings to chains transformation also in the liquid.

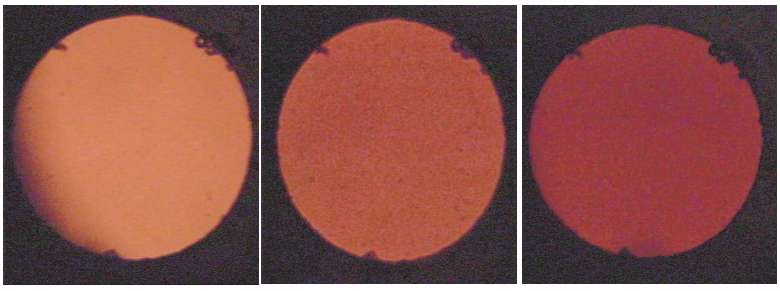

Figure 5.24: The color of liquid sulfur with increasing pressure. From the left to the right we observe the liquid at 0.4, 0.6 and 1 GPa (The temperature is around 250°C).

In figure 5.24 we have reported the photographs of the sample taken during the compression. Accordingly with the previous literature [156, 157], one of the reason because the color of liquid sulfur (between the λ-transition and 250°C) becomes increasingly red could be the polymer content.

The DAC has been also used in the collection of both diffraction and Raman data. The sulfur powder has been placed directly into a metallic gasket. Temperature has been measured using a thermocouple and pressure calibrated measuring the shift of the ruby fluorescence. To obtain a structure factor in a large Q-range with a good resolution on the first peaks, a set of measurements have been conducted at different energies (wavelength, λ, equal to 0.53394 Å, 0.3738 Å and 0.26473 Å). The data have then been combined together giving rise to the structure factors shown in figure 5.25.

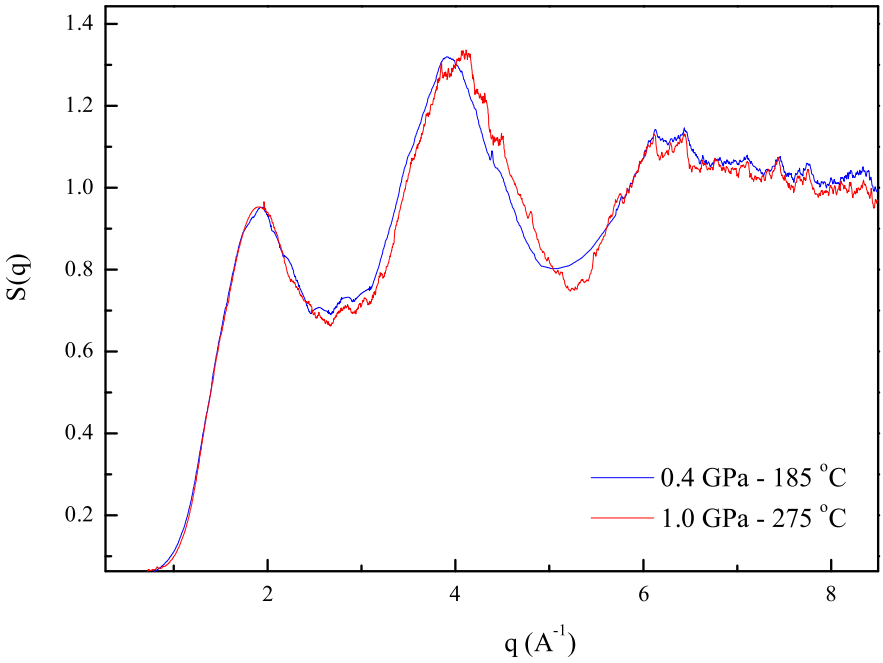

Figure 5.25: The two structure factors of liquid sulfur obtained by combining different patterns measured at different energies (wavelength, $\lambda = 0.53394$ Å, $\lambda = 0.3738$ Å and $\lambda = 0.26473$ Å).

Despite the structure factor seems to not change significantly in between 0.4 GPa and 1 GPa, the change is considerable if we compare them with the structure factor measured at ambient pressure. We have plotted in figure 5.26 the structure factor measured at ambient pressure and 275^{o}C reported in ref. [72] and the structure factor that we have measured at 1 GPa and 275^{o}C [6].

[6]The comparison has been done with the structure factor at 1 GPa because the temperature is almost the same.

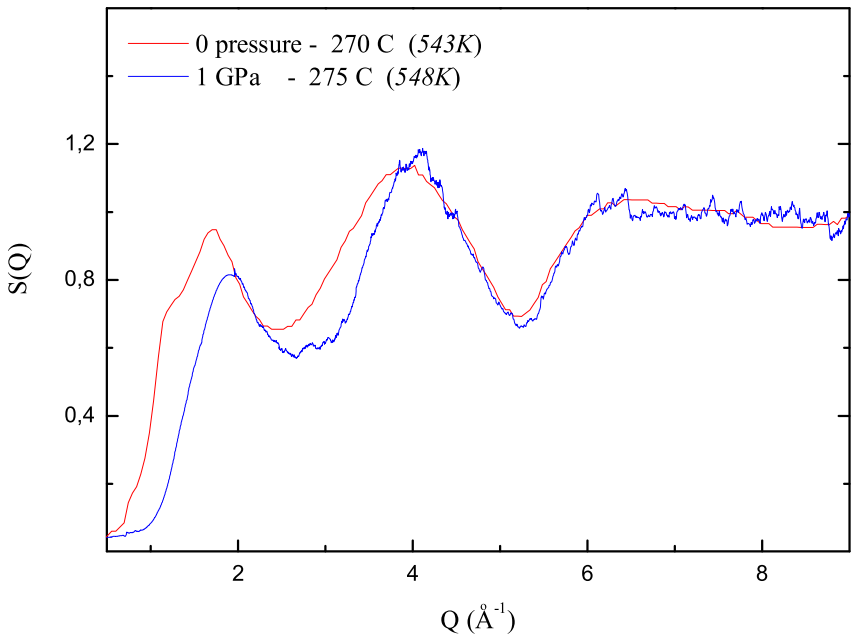

Figure 5.26: The structure factor of liquid sulfur at ambient pressure and 275^{o}C from ref. [72] (red line) and the structure factor that we have obtained at 1 GPa and 275^{o}C (blue line).

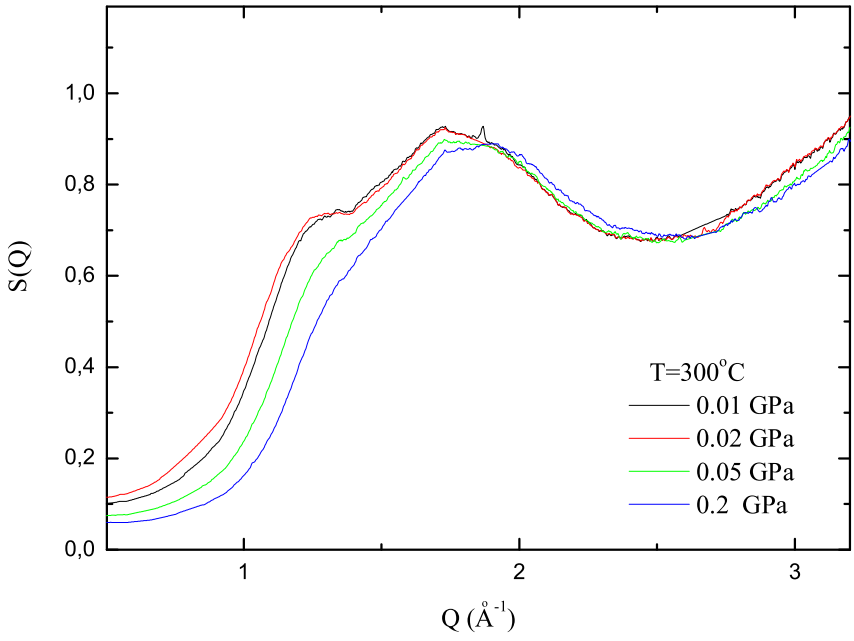

Figure 5.27: The structure factors of liquid sulfur obtained in the LVP at relatively low pressures and 300^{o}C.

As introduced above, the figure 5.26 evidences that the main changes are related to the first peaks of the structure factor, in the region that goes from 0 to 5 $Å^{-1}$. This changes are strictly related to the structural changes that takes place in the liquid.

What is the character of this transition?

In order to give an answer to this question we have measured in the LVP the evolution of structure factors going from 0.01 GPa to 0.2 GPa, trying to maintain the temperature constant at about 300^oC. The structure factors that we have extracted are shown in figure 5.27.

Actually, from this picture a continuously changing structure factor emerges. The changes in the structure factor could be related to the diminution of the molecular S_8 content due to the continuous transformation of S_8 rings to chains. However, this information is not sufficiently detailed in order to conclude that pressure induces the complete polymerization in the liquid as in the solid.

The complementary use of Raman spectroscopy, has been considered useful in order to define the nature of these changes. In particular, we have chosen Raman spectroscopy, because the Raman spectra allow distinction between the modes characteristic of the S_8 rings that are not observed in the polymeric chains. From the study of the polymerization in the solid, in fact, we know that the bending modes of the molecule located in the 150-250 cm^{-1} frequency range disappear in the polymer spectrum (see figure 5.2). We have therefore, considered the disappearance of the Raman lines in this frequency range as an indication of the full polymerization of the liquid.

The Raman setup is the same as described for the measurements on the solid. The experiment has been conducted in two steps. Firstly, we have measured several Raman spectra across the melting at 0.2-0.3 GPa. The evolution of the spectra is shown in figure 5.28.

Apart from a normal broadening of the spectra above the melting and the disappearance of the lattice modes, all the data, below and above the melting, are characterized by the lines related to the molecule bending and stretching. As a consequence we conclude that a fraction of S_8 molecules is present in the liquid at this pressure.

Once we have confirmed that at this pressure the liquid still contains S_8 molecular units, we have increased the pressure in order to observe the disappearance of the characteristic modes of the molecules. The correspondent spectra have been plotted in figure 5.29.

Actually, looking at the evolution of the Raman spectra with pressure (from the bottom to the top) the progressive disappearance of the bending modes in the region

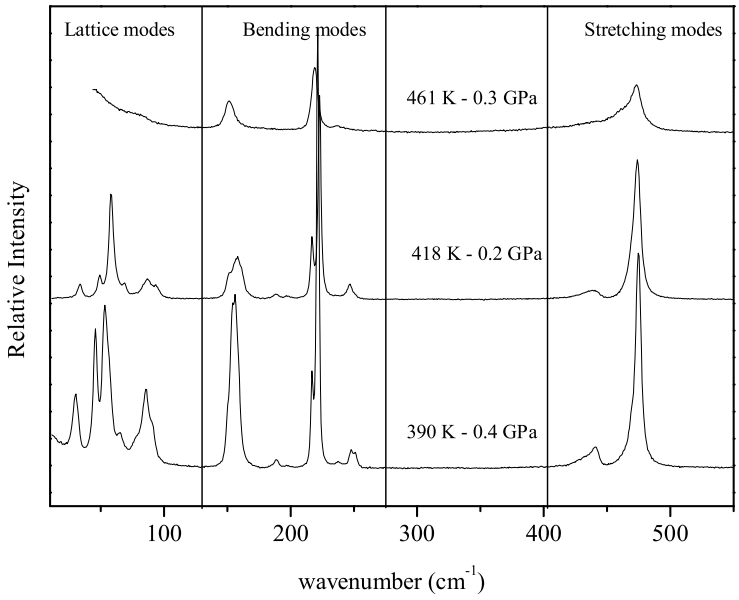

Figure 5.28: Raman spectra of liquid sulfur across the melting line. The bending and stretching modes characteristic of the S_8 molecule are still observable in the liquid spectrum at 461 K and 0.3 GPa.

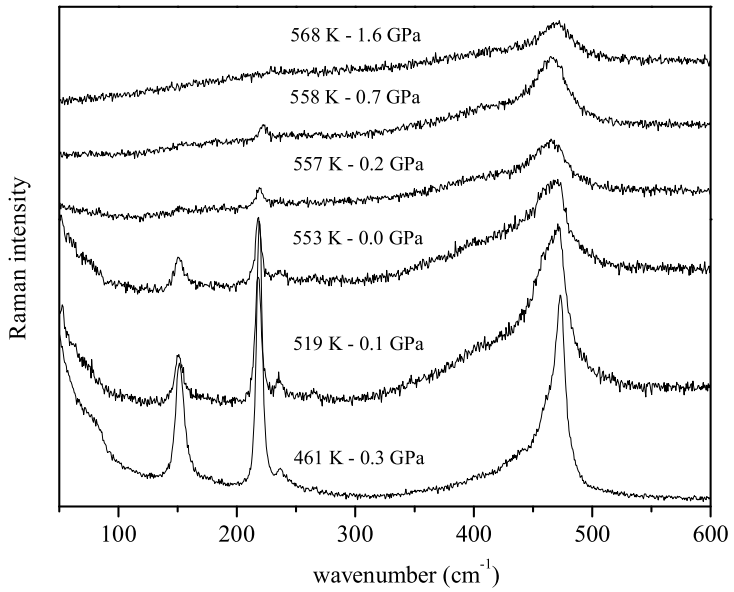

Figure 5.29: The evolution of the Raman spectra of liquid sulfur with increasing pressure. The diminution of the molecular fraction can be followed by the progressive disappearance of the bending modes in the region between 100 and 250 cm^{-1} characteristic of the molecule S_8.

between 100 and 250 cm^{-1} that are characteristic of the S_8 molecule indicates that there is a diminution of the S_8 concentration in the liquid. Unfortunately increasing pressure the intensity of the liquid spectra becomes more and more weak. Considering that the color with pressure becomes more and more red and the laser energy we have used for the experiment, we believe that at these thermodynamic conditions we are close to the optical absorption edge of the polymeric liquid.

The complementary use of x-ray diffraction and Raman spectroscopy allow us to conclude that pressure induces structural changes in liquid sulfur. These changes are related to the S_8-polymer equilibrium that moves to the purely polymeric liquid if the pressure is increased sufficiently. This polymeric liquid should be stable in wide range of pressure: comparing the available literature data in fact, it results that the structure factor of liquid sulfur at 1 GPa is similar to the one at 7.6 GPa measured by Katayama [158] (fig.5.30).

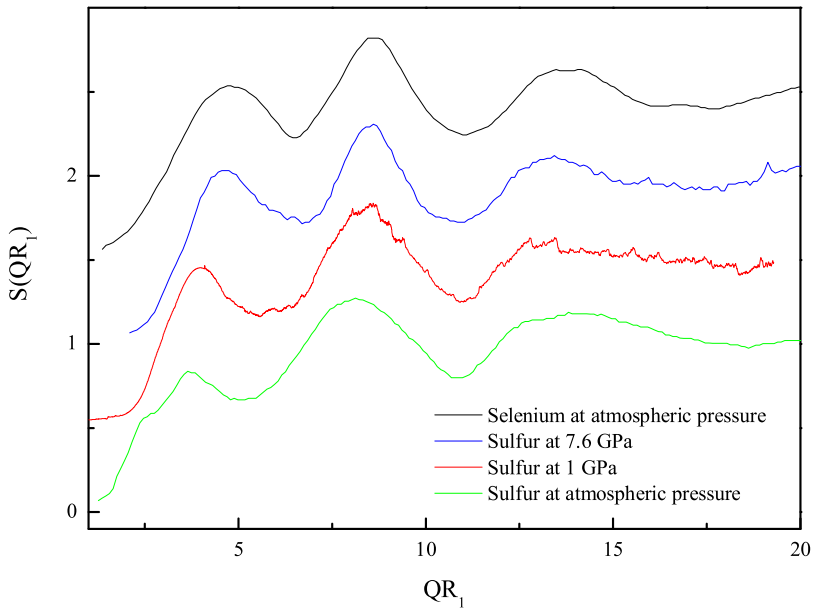

Figure 5.30: Comparison of the structure factor of liquid sulfur at atmospheric pressure (green line) [72], 1 GPa (red line) (our data), and 7.6 GPa (blue line) [158] with the structure factor of liquid selenium at atmospheric pressure (black line) [159]

The structure factor is not influenced by pressure: from the high Q data, we conclude that the short range order does not change under these pressures; in the low Q data

there is no indication for structural changes, the shift of the first peaks simply reflects the more efficient packing induced by pressure. In figure 5.30 we have also reported the structure factor of liquid selenium at ambient pressure [159]. The analogy with liquid selenium suggests that the high pressure behavior of an element is similar to the one of the successive elements in the same group of the periodic table at lower pressure. This is true in the liquid as in the solid [160].

5.4 The phase diagram

The natural conclusion of this work on the polymorphism of sulfur is the construction of its phase diagram. All the diffraction data collected with the LVP and the DAC are plotted in figure 5.31.

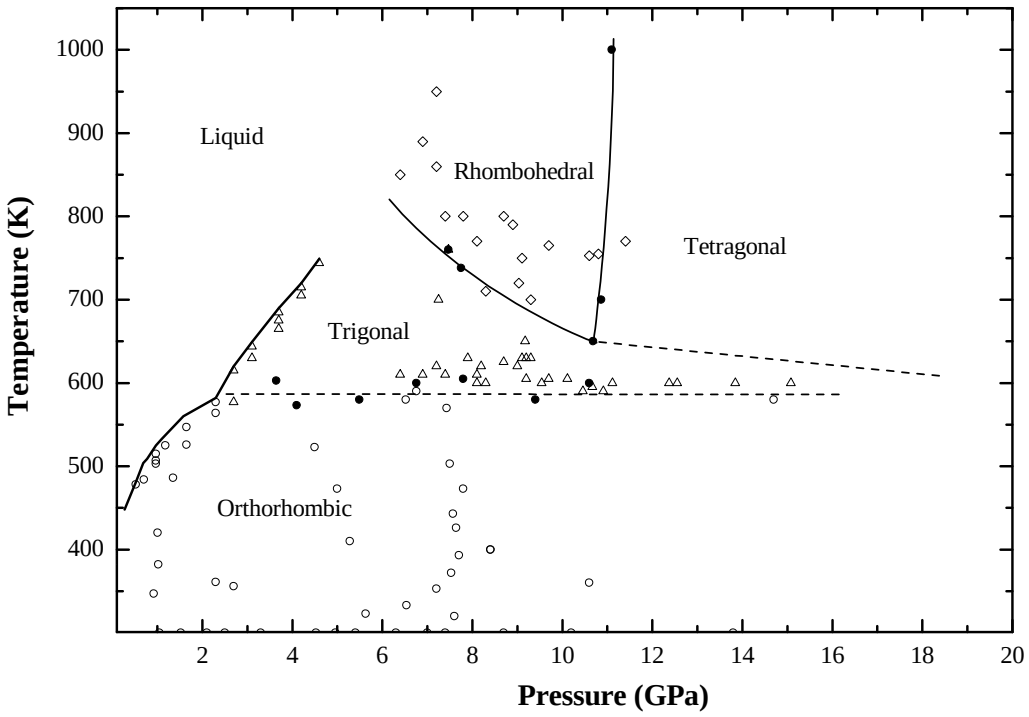

Figure 5.31: The phase diagram of sulfur.

This phase diagram allow us to reconcile the controversial results obtained by diffraction and Raman spectroscopy. The sequence of structural transformations observed by Raman spectroscopy at room temperature [82, 125, 129, 130] (S_8 - *p-S* - S_6 and/or *hplt*) corresponds, in fact, to the sequence observed by X-ray diffraction at high temperature and in the same pressure range [23, 144]. This indicates that, the photo-induced

phase transitions observed by Raman measurements, effectively correspond to existing structural transitions in the phase diagram and supports the hypothesis of a kinetic barrier associated with the breakdown of the S_8 rings that leads polymerization, kinetic barrier that can be overcome either by laser illumination or by temperature increase.

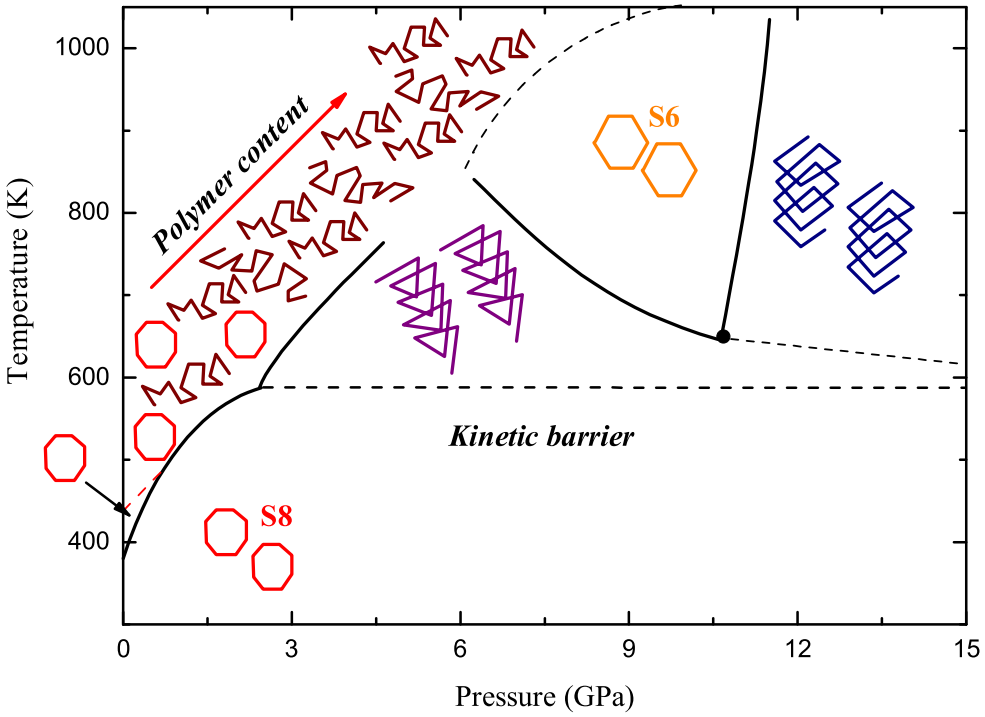

Figure 5.32: The structures in the phase diagram of sulfur.

The panorama of structures studied in solid and liquid sulfur has been illustrated in the phase diagram reported in figure 5.32. The polymorphism of solid sulfur reveals a rich sequence of allotropes resulting from the high tendency to the polymerization and the eventual re-annealing of molecular forms at high pressure and temperatures. From the knowledge of the solid behavior we have advanced hypothesis on the polymorphism in the liquid. The solid polymerization has in fact its own correspondent transition in the liquid domain, supporting the correlation between the solid and the liquid behavior.

Résumé du chapitre 6

La formation de chanes polymériques dans le soufre liquide au-dessus de la transition λ a été interprétée comme une réaction de polymérisation. Il convient de souligner qu'il ne s'agit pas d'une polymérisation classique déclenchée par un agent chimique et se terminant par la formation complète de la phase polymérique mais d'une polymérisation á l'équilibre ou la température gouverne la proportion des phases polymérique et moléculaire. Les modèles théoriques qui décrivent cette phase sont bases sur une hypothèse de chanes linéaires sans interaction. L'étude de la dynamique autour de la transition λ a été menée en vue d'examiner le bien fondé de ces hypothèses. La mesure de la vitesse du son et de son atténuation, á basse fréquence étaient les seules données disponible pour le soufre liquide. La comparaison des données d'atténuation avec les prévisions hydrodynamiques montre des contradictions au-dessus de la transition λ. Le soufre ne semble pas être viscoélastique en dépit d'une énorme viscosité statique.

Nous avons mesure la diffusion inélastique des rayons X par le soufre liquide á des températures de part et d'autre de la transition de polymérisation. Le facteur de structure dynamique obtenu, S(Q,ω) a été representé par un modele d'oscillateur harmonique amorti (DHO : Damped Harmonic Oscillator). Il nous permet de determiner les proprietes elastiques du soufre dans la gamme des hautes frequences (THz). A partir de la comparaison de nos résultats avec ceux des mesures ultrasoniques (MHz) et avec les prévisions thermodynamiques nous pensons que le soufre liquide, au-dessus de la transition , n'a pas atteint l'équilibre thermodynamique. Ceci suggère l'existence d'un mode de relaxation á plus basse fréquence. Un calcul base sur la théorie viscoélastique de Maxwell fait explique les données par l'existence de deux modes de fréquences différentes. Le plus rapide (THz) est commun a la molécule et au polymère tandis que le plus lent est propre a la phase polymère. Dans le cadre de ce modèle nous pouvons distinguer deux comportements différents pour des températures au-dessous et au dessus de la transition λ : i) un liquide moléculaire classique avec une transition vitreuse dans la gamme des GHz dont la dynamique est celle des molécules S_8; ii) Une solution de polymères intercon-

nectés dans un solvant moléculaire qui présente deux modes dynamiques distincts. L'un á haute fréquence correspond aux molécules S_8. L'autre, á basse fréquence correspond á des modes de reptation de fragments de chanes entre des interconnexions. Un modèle de chanes interconnectées permet de calculer des longueurs de segments ainsi que la relation entre longueur moyenne des chanes et viscosité.

Chapter 6

Liquid dynamics around the λ-transition

6.1 Introduction

In the previous chapter, we have presented the results obtained on liquid sulfur by XRD and Raman investigation; the information coming from these measurements clarify the structural changes of the liquid in a wide p,T domain. In the present chapter we report the Inelastic X-ray Scattering (IXS) measurements that have been conducted on liquid sulfur around the λ-transition. The scope of these measurements was to understand how the formation of polymeric chains influences the dynamical properties of the liquid. If on one side in fact, the static structure factor does not change abruptly at the polymerization temperature, on the other side, the viscosity jump observed at 159^{o}C suggests significative differences in the dynamics of the liquid below and above the λ-transition (figure 6.1).

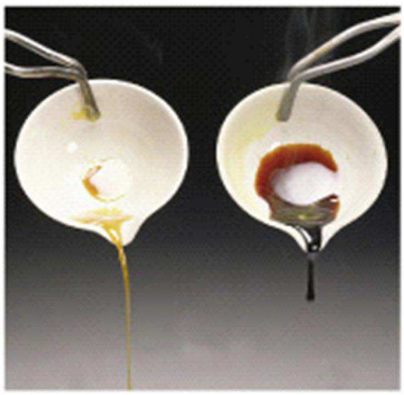

Figure 6.1: Picture that illustrates the changes in liquid sulfur below (left) and above (right) the λ-transition.

After an introduction to the available thermodynamic models on the polymerization of liquid sulfur, we will discuss our IXS data suggesting a model able to describe both our data and the different results available in the literature.

6.2 Equilibrium polymerization in liquid sulfur

Several theoretical models have been applied or developed to describe the evolution of liquid sulfur around the λ-transition. The most recent ones consider the polymerization in sulfur as a *living polymerization*, or more in general as an *equilibrium polymerization*. In general, polymerization is a chemical process that proceeds basically in three steps: *initiation, propagation and termination*. The initiation consists in the formation of a very reactive species, normally a radical, able to activate a chain monomer. During the propagation the activated chain monomer begins a chain reaction with other monomers, that step by step elongates the polymer. In the termination step, the active sites react with a terminator reagent stopping the propagation and then the polymerization process. The living polymerization can be viewed as a polymerization process that does not 'terminate'.

In the case of liquid sulfur, the polymerization process can be described through the following reactions:

$$S_8 \rightleftarrows \cdot S_8 \cdot \tag{6.1}$$

$$\cdot S_{n8} \cdot + S_8 \rightleftarrows \cdot S_{8(n+1)} \cdot \tag{6.2}$$

where the ring opening (eq. 6.1) and the formation of the diradical $\cdot S_8 \cdot$ corresponds to the initiation step, while the chain elongation (eq. 6.2) corresponds to the propagation of the reaction. Like a chemical reaction, each step is associated to a chemical equilibrium with its own equilibrium constant. Despite normally the initiation requires an external chemical initiator, in the case of sulfur this function is supplied by temperature. It has to be remarked that, the final stage of living polymerization is normally associated to an early and thermodynamically unstable state, that is not the case of sulfur. For that reason the case of sulfur has been classified as an *equilibrium polymerization* since the full attaintment of equilibrium is then achieved.

Several theoretical models have been reported in the literature to describe the λ-transition of sulfur as *equilibrium polymerization*. The first models, proposed by Tobolsky and Eisenberg [161], treat the polymerization of sulfur as a chemical equilibrium based on the initiation and propagation reactions described through eq. 6.1 and eq. 6.2. Being the equilibrium constant of a chemical reaction related to the entropy and the

enthalpy variations through the relation:

$$K = e^{\frac{T\Delta S - \Delta H}{RT}} \tag{6.3}$$

the equilibrium constants of the initiation and propagation reactions in liquid sulfur can be calculated from thermodynamic data on the enthalpy and entropy of the reaction. Writing eq. 6.1 and eq. 6.2 in terms of equilibrium constants and concentrations:

$$K_o = \frac{|\cdot S_8 \cdot|}{|S_8|} \tag{6.4}$$

$$K_p = \frac{|\cdot S_{8(n+1)} \cdot|}{|\cdot S_{n8} \cdot|\,|S_8|} \tag{6.5}$$

and considering the appropriate mass balances, several calculations can be carried on in order to obtain parameters like the polymer mass fraction, ϕ, or the heat capacity, c_p. The calculations based on this theory are relatively simple and work well for a qualitative description of the behavior of sulfur through the λ-transition [162]. However, this model neglects non-classical critical effects observed in correspondence to the λ-transition.

These effects, like the λ divergence observed in the heat capacity measurements, are better explained in terms of the non-mean-field theory proposed by Wheeler *et al.* [163]. These authors use the partition function of the non classical n-vector lattice model of magnetism in the mathematical limit n$\longrightarrow$0 in order to represent a system of S_8 rings in equilibrium with the polymer chains. In this lattice model each S_8 unit, either a ring or a monomer, occupies a lattice cell. The polymer chains are linear and each configuration has a statistical weight determined by the equilibrium constants, K_o and K_p, for the initiation and polymerization processes. Wheeler *et al.* [163] reproduce with a good qualitative agreement the critical effects observable in the experimental data.

In order to compare the quality of the results obtained with the models of Tobolsky *et al.* [161] and of Wheeler *et al.* [163], we report in figure 6.2 a plot of the measured heat capacity of sulfur [69, 164] together with both model predictions.

Despite that the model of Wheeler *et al.* [163] takes into account the critical phenomena appearing at the λ-transition, it fails in a quantitative description of the heat capacity over an the extended temperature description [162]. Viceversa, the mean field calculation gives a better quantitative description but is unable to describe the λ divergence at the polymerization temperature.

The failure of both models could be due to the common basic assumption that the polymer is formed only by linear chains [161, 163]. In fact, the formation of loops or branches between the polymeric chains is neglected by these models. Despite a simple

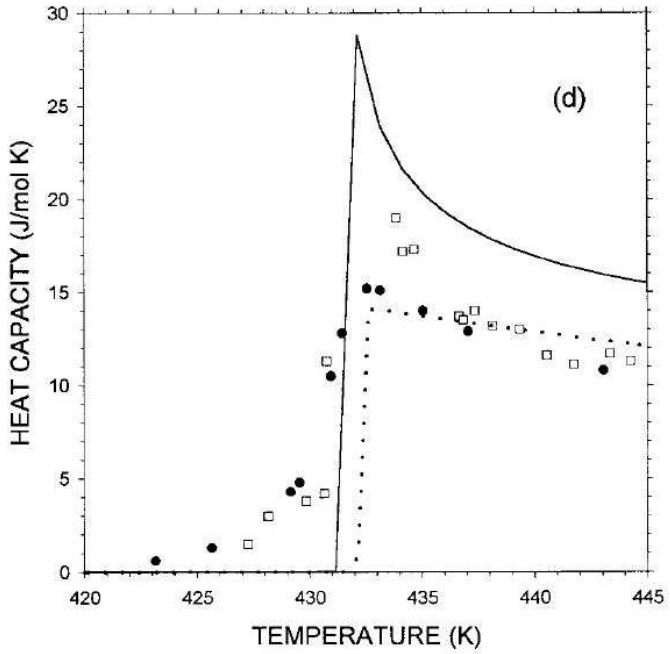

Figure 6.2: Equilibrium polymerization of sulfur: Comparison between experimental data of the heat capacity (symbols [69, 164]), the predictions of the mean field model ([161], dotted line) and the calculations of Wheeler *et al.* ([163], solid line) from ref. [162].

polymer morphology can represent a good starting point for theoretical calculations, more sophisticated models are needed to be developed.

A large number of experimental and theoretical works have been performed on liquid sulfur, but its complex behavior is still not fully understood. For that reason we have performed high frequency IXS measurements: a suitable information can in fact arise from the knowledge of the liquid dynamics below and above the λ-transition.

6.3 The study of the liquid dynamics

The study of the atomic dynamics of liquids can be accomplished in condition of thermodynamic equilibrium, or by perturbing the system with an external probe. In the first case we look at the damping of the spontaneous thermal fluctuations that arises in the system at thermodynamic equilibrium; in the second case, we look at the damping of the perturbation. The attaintment of a new equilibrium will take a certain time, the *relaxation time*, that depends on the facility of the molecules to move relatively to their

neighbors. These microscopic diffusion processes can be described macroscopically by the transport coefficients of the system. For that reason it is reasonable to think that the jump in the viscosity of liquid sulfur at the λ-transition could be understood by studying the atomic dynamic of the system.

Among the relaxation processes that can be active, or activated, in a liquid system, a crucial role is played by the structural relaxation. The structural relaxation is related to the cooperative processes through which the local structure rearranges reaching a new equilibrium position. The response of the system to an external perturbation obviously depends on the relative duration of the perturbation, ω^{-1}, as compared to the relaxation time, τ_α. We can distinguish two kind of responses:

if $\omega\tau_\alpha \ll 1$**:** the system has the time to rearrange toward a new equilibrium condition. This situation normally occurs in liquids;

if $\omega\tau_\alpha \gg 1$**:** the system does not have the time to rearrange, remaining "frozen" in the existing equilibrium state. This situation is characteristic of the glassy state.

The structural relaxation, or α-relaxation, is typical of all liquids; its characteristic relaxation time, τ_α, is temperature dependent and proportional to the shear viscosity, η_s:

$$\eta_s = G\tau_\alpha \tag{6.6}$$

where G is the bulk modulus of the liquid. As a consequence of that, in the range defined by the condition $\omega\tau_\alpha \simeq 1$, where the interaction between the structural relaxation and an acoustic wave of frequency $\nu = \omega/2\pi$ is maximal, the knowledge of the transport properties of the system can give us an idea on the acoustical window for the study of a structural relaxation.

In the conditions where the system can be considered in thermodynamical equilibrium, i.e. when $\omega\tau_\alpha \ll 1$, the dynamic behavior of the system is governed by the laws of *Simple Hydrodynamics* [165]. In the hydrodynamic description, the liquid is a continuum medium, and there exists a closed set of equations describing the space-time variations of the conserved variables: the particle number, the current and the energy densities. This description becomes more explicit when the appropriate thermodynamic and transport coefficients are specified. The transition to the glassy region, where $\omega\tau_\alpha \gg 1$, is described by the introduction of frequency dependence into the thermodynamic and transport coefficients. The regime where the physical properties of the system are frequency-dependent is referred to the *molecular Hydrodynamics* regime [165].

From the experimental point of view the low frequency techniques are the more appropriate to give information on the hydrodynamic regime. Obviously, it is clear that

the term "low" frequency strictly depends on the probed system. In the specific case of normal liquid systems, low frequency techniques can be used to study at frequencies up to the GHz range. On the other side, the the elastic properties of the system should be studied on the short time scale and should be probed with high frequency techniques like IXS. In every case, a complete picture of the atomic dynamic of a system can be drawn only by a complete q-ω study.

The central tool for the study of the dynamics of liquids is the time and space Fourier transform of the correlation function for the particle density fluctuations: the dynamic structure factor, S(q,ω). It is directly obtained with many experimental techniques, and contains the dynamical information for a statistical description of the atomic dynamics. The dynamic structure factor depends on both the energy E and the wavevector q, and can be expressed as:

$$S(q,E) = \frac{1}{2\pi N} \int dt\, e^{i\omega t} \sum_{m,n} \langle e^{iq\cdot r_m(t)} e^{iq\cdot r_n(0)} \rangle \tag{6.7}$$

with N the number of particles in the system whose positions at time t are $r_n(t)$ (n=1,...N). In the continuum limit, i.e. for $q \longrightarrow 0$, hydrodynamics provides an explicit expression of S(q,ω) [166]. The spectrum comprises three peaks, the Brillouin triplet, which are centered at E=0 and E=$\pm\hbar v_o$q, and correspond to the entropy fluctuations at constant pressure and to the pressure fluctuations at constant entropy respectively; v_o is the adiabatic sound velocity. The two peaks at E=$\pm\hbar v_o$q have a width proportional to the longitudinal viscosity and depend quadratically on q. The molecular hydrodynamic formalism [165], can be used to describe the dynamic structure factor at high frequencies: in these conditions the system usually undergoes a transition from a liquid-like regime to a solid-like one. This transition is marked by the modification of the speed of sound from the hydrodynamic value v_o to an higher value v_∞. The width of the Brillouin peaks also changes as the dissipation through structural rearrangements is frozen.

In the case of liquid sulfur, like for any other liquid, we expect to observe a structural relaxation at temperatures below the λ-transition, where the liquid is purely molecular; but at higher temperatures, where the physical properties are affected by the presence of the polymeric component, *how does the atomic dynamics of the system change?*

A set of high frequency IXS data, below and above the λ-transition, has been collected in order to clarify this issue. Obviously, in order to have a complete picture of the dynamics of the system, the high frequency data need to be compared with literature ones previously collected at low frequency. For that reason, before presenting our analysis, we briefly review the available acoustic literature on liquid sulfur.

6.4 Literature studies on liquid sulfur

Until recently, the information on the acoustical properties of liquid sulfur was limited to low frequency measurements of the sound velocity [167–169]. Recently, Kozhevnikov *et al.* [170,171], have reported a complete set of data of sound absorption and sound velocity of liquid sulfur in the 120-200^{o}C temperature range under saturated vapor pressure. The experiments were performed with a phase sensitive technique at frequencies comprised between 0.5 and 22 MHz.

Qualitatively, the results reported by Kozhevnikov *et al.* and the data reported in the earlier works on sound velocity are in agreement. Discrepancies between the different set of data are of the order of 2-3%. The comparison between the available literature data is shown in figure 6.3.

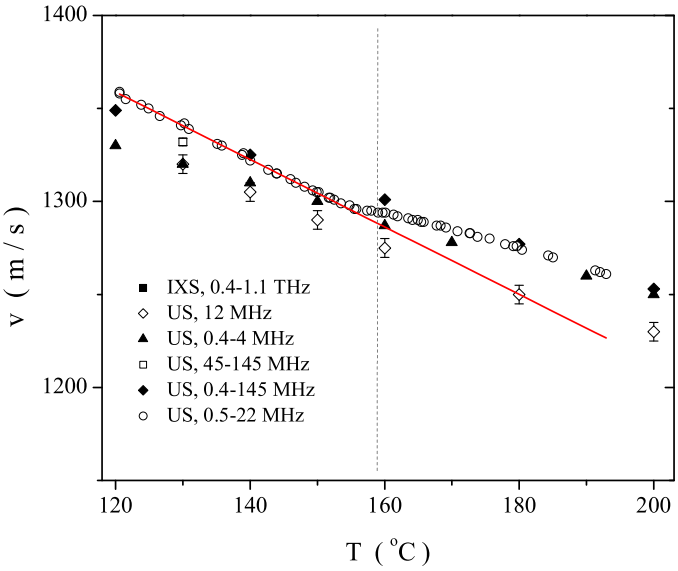

Figure 6.3: Comparison of the available literature data for the sound velocity of liquid sulfur below and above the lambda transition. The corresponding references are: 12 MHz - [167], 0.4-4 MHz - [168], 45-145 MHz - [169],0.4-145 MHz -(data from ref. [171]), 0.5-22 MHz - [171]. The red line represents the best fit results for the T dependence of the sound velocity in the domain of the molecular liquid.

As it is evident from figure 6.3, the sound velocity decreases monotonously as a function of temperature, experiencing a change of slope around the λ-transition temperature. In a first approximation Kozhevnikov *et al.* [170, 171] have considered these

data at thermodynamic equilibrium, i.e. correspondent to the zero-frequency velocity of sound of liquid sulfur, and have used them for evaluating the increase of the polymer fraction in the polymer solution above the λ-transition. The bulk modulus, B, of the polymeric solution can be expressed as:

$$B = \varphi_p B_p + \varphi_m B_m \tag{6.8}$$

where B_p and B_m, and φ_p and φ_m, are respectively the bulk moduli and the volume fractions of the polymeric and molecular components.

Since $v^2 = \frac{V}{M} B$, where M is the molecular weight and v is the sound velocity, v^2 can be expressed as:

$$v^2 = \phi_m v_m^2 + \phi_p v_p^2 \tag{6.9}$$

where ϕ_p and ϕ_m, and v_p and v_m, are respectively the mass fractions and the sound velocities of the polymeric and molecular components.

Considering the mass balance $\phi_p + \phi_m = 1$, the polymer extent, ϕ_p, can be expressed as:

$$\phi_p = \frac{(\Delta v / v_m + 1)^2 + 1}{(v_p / v_m)^2 - 1} \tag{6.10}$$

where the only unknown quantity is the ratio v_p/v_m; the values of v_m can be, in fact, easily extrapolated by fitting the slope of the sound velocity linear data below the polymerization temperature. Kozhevnikov *et al.* have extrapolated the ratio v_p/v_m by using the previous literature data on the polymer extent, and obtaining the values 1.12 and 1.08 using ref. [161] and ref. [153] respectively. With eq. 6.10 we obtain a measure of the difference in sound velocity between the molecular and the polymeric components.

The data on the sound absorption, α, as measured by Kozhevnikov *et al.* [170, 171], have been reported in figure 6.4.

In the limits of the experimental error, the sound absorption of liquid sulfur measured at different frequencies does not show any variation with temperature, even around the λ-transition temperature.

What are the implications of these data on the dynamical behavior of liquid sulfur?

The critical behavior of sulfur, and in particular the discontinuity in the heat capacity in correspondence to the λ-transition suggests that the polymerization of sulfur is a second order phase transition. In the scaling theory of the second order phase transitions, we should expect a minimum in the sound velocity data at zero-frequency: however, this minimum is not observed in the available low frequency data.

In addition to that, in the hypothesis that one has measured the equilibrium properties of liquid sulfur in the entire probed temperature range, and as a consequence

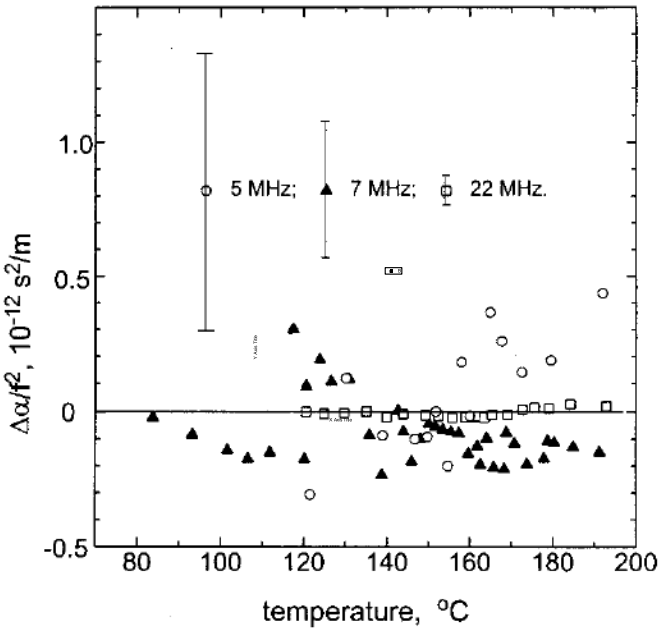

Figure 6.4: Variation of the sound absorption of liquid sulfur, normalized for the squared frequency, as a function of temperature. The data have been measured at 5, 7 and 22 MHz, the relative errors are shown at the top of the plot from ref. [171].

across the viscosity jump at the λ-transition, at that temperature we should expect a considerable increase of the sound absorption as measured at low frequencies. Based on simple hydrodynamics, in fact, the sound absorption, α, can be expressed as:

$$\alpha = [4/3\,\eta + \zeta + \kappa\,(1/c_p - 1/c_v)]\frac{\omega^2}{2\rho v^3} \tag{6.11}$$

where η and ζ are the shear and the bulk viscosities, κ is the thermal conductivity, c_p and c_v are the constant pressure and constant volume heat capacities, $\omega = 2\pi\nu$ and ρ is the density. This expected enhancement is not observed in the data reported by Kozhevnikov *et al.* [170, 171]. The authors of ref. [170] have interpreted this result as a possible effect of viscoelasticity in the polymeric solution above the λ-transition. For that reason, in a successive work Kozhevnikov *et al.* [171] have reported measurements of the longitudinal and transverse sound waves. The absence of any signal coming from transverse excitations has induced the authors to conclude that *"Sulfur is a viscous liquid, but not viscoelastic..."*. This surprising conclusion requires further investigations in order to be really validated.

In the light of these data and considering that the present knowledge on the dynamics of sulfur below and above the λ-transition is still poor, the addition of new high frequency data and their analysis in combination with the other acoustic data available in the literature could be useful to define a framework where all the available data can be interpreted with consistency.

6.5 Dynamic structure factor of liquid sulfur as measured by IXS

The dynamic structure factor S(q,ω) measurements on liquid sulfur have been conducted at the ID16 beamline at ESRF. The S(q,ω) spectra have been collected for different q-values and at various temperatures (130, 150, 160, 175, 200^{o}C) using the Si(11,11,11) reflection, with an incident energy of 21.748 keV. The intensity of the X-ray beam incident on the sample was 10^9 photons/s while the dimensions of the spot were 250 X 200 μm^2 (horizontal X vertical sizes). At each of the selected temperatures, the IXS spectra at different q points in the 1-15 nm^{-1} range have been measured.

The resolution has been determined measuring the elastic scattering from a 5 mm thick PMMA (plexiglass) sample at the maximum of its static structure factor S(q) (q $\simeq$ 10 nm^{-1}) and at low temperature ($\simeq$ 10 K). In these conditions, the inelastic component is negligible with respect to the elastic one. The PMMA thickness has been chosen in order to give a strong elastic scattering while keeping small the source size contribution to the energy resolution. The measured resolution has a FWHM of 1.5 meV with a detailed shape close to a Lorentzian. The total q resolution was set to 0.37 nm^{-1} FWHM. The sample container was a brass cell with nickelated internal surfaces and 30 μm mica windows.

Several IXS spectra measured at 423 K and at selected q values have been reported in figure 6.5. The q-dependence is similar at all the probed temperatures.

The inelastic signal is contained in the tails of the elastic scattering signal (convoluted with the resolution). The information on the Brillouin peak position and the linewidth has been obtained by fitting the row data using a DHO (Damped Harmonic Oscillator) model. The details of this model will explained in the next paragraph.

6.5.1 The DHO model

The dynamic structure factor, S(q,ω) can be expressed in the frequency domain:

$$S(q,\omega) = \frac{2v_o^2 q^2}{\omega} Im[\omega^2 - \omega_o^2(q) - i\omega m_q(\omega)]^{-1} \tag{6.12}$$

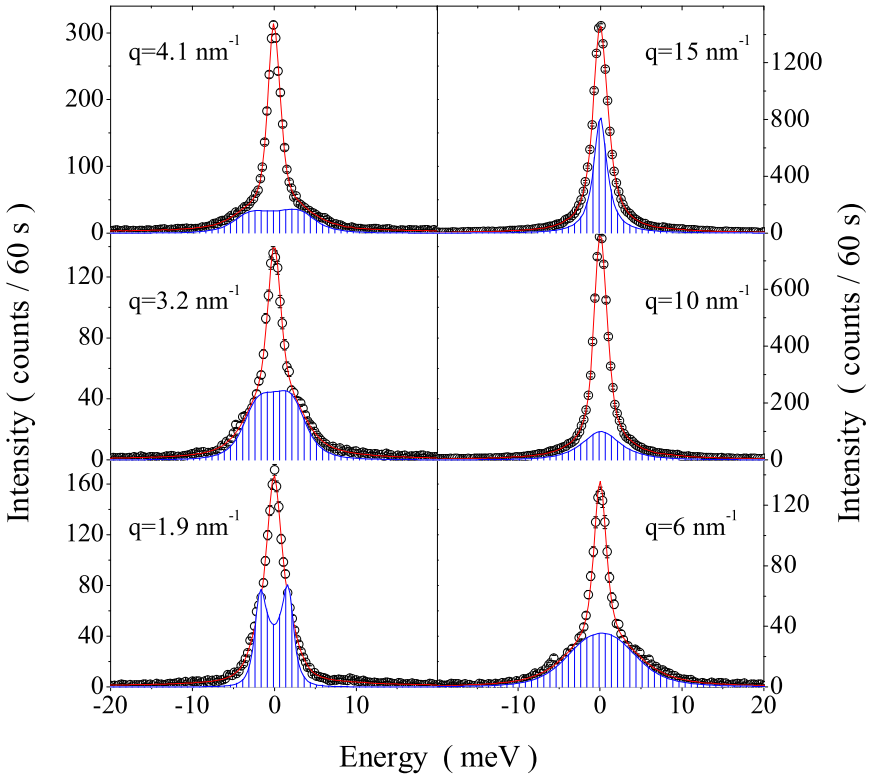

Figure 6.5: Experimental IXS spectra obtained at some selected q in the liquid phase at T=423 K. The row data (symbols) are reported together with the fitting obtained on the basis of a DHO model (red line). The inelastic contribution (convoluted to the resolution) has been also evidenced (filled area). The scattered intensities are here reported as counts per 60 s; the total integration time per point varies between 300 and 400 s.

where Im denotes the imaginary part; v_o is the adiabatic sound velocity, and for $\omega_o(q)$ is valid the relation:

$$\omega_o(q) = \frac{(qv_o)^2}{S(q)} \tag{6.13}$$

The function $m_q(\omega)$ is called memory function and takes into account the space-time variations of the thermodynamic derivatives and the transport coefficients of the system. The analytical form of the memory function is known [165, 166] for systems in the hydrodynamic regime. In other conditions, such as in the molecular dynamics regime, different models for the memory functions have to be introduced. For our analysis, the chosen model is the Damped Harmonic Oscillator model (DHO), and the correspondent

analytical form of the memory function is:

$$m_q(t)_{DHO} = 2\Gamma_l(q)\delta(t) + \frac{q^2}{\rho}\Delta^2(q) \tag{6.14}$$

where the first term takes in account for the atomic vibrations in the local environment (microscopic decay), and the second term describes the classical phenomenology of the dispersion and absorption of the sound waves, in other words, the transition of the sound velocity from its adiabatic equilibrium value, $v_o(q)$, to the high frequency value, $v_\infty(q)$. Indeed, the term $\Delta^2(q)$ can be expressed as:

$$\Delta^2(q) = \rho[v_\infty^2(q) - v_o^2(q)] \tag{6.15}$$

With this memory function (eq. 6.14), the dynamics structure factor is given by the sum of a $\delta(q)$ and a DHO term. The S(q,ω) reads:

$$\frac{S(q,\omega)}{S(q)} = 2\pi f_q\delta(q) + [1 - f_q]\frac{2\omega_\infty^2(q)\Gamma_l(q)}{[\omega^2 - \omega_\infty^2(q)]^2 + \Gamma_l(q)^2\omega^2} \tag{6.16}$$

where $\omega_\infty(q)$ is the Brillouin peak position, f_q=$1 - (\omega_o(q)/\omega_\infty(q)$ is known in the literature as the non ergodicity factor parameter [172] and $2\Gamma_l$(q) refers to the Brillouin peak width (FWHM).

The S(q,ω) spectra have been fitted to the convolution of the experimentally determined resolution with the structure factor of eq. 6.16 using standard χ^2 minimization.

In figure 6.5 we report the experimental spectral density at selected q values and for T=423 K, together with the relative best fit lineshape and the resolution convoluted, inelastic component. A fairly good agreement has been found between the experimental and the best fit lineshape, this will allow us to discuss the q dependence of the fitting parameters and to make a comparison between the behavior of the liquid below and above the polymerization temperature.

6.5.2 The q dependence of the inelastic spectral component

A curve representing the inelastic peak as a function of the exchanged momentum, ω_∞(q) is called dispersion curve. The dispersion curve of liquid sulfur for the two temperatures: 423 K and 473 K, is reported by symbols in figure 6.6. In the same figure, we have reported also the relative static structure factor (green lines). At all the probed temperatures we observe a positive linear dispersion in the low q region and a deviation from the linearity with a minimum value for ω_∞(q) in correspondence to the first peak of the static structure factor S(q). A linear dispersion at low q values is

commonly observed in liquid systems [165], it means that the liquid can be considered a continuum, i.e., the hydrodynamic relation:

$$\omega_\infty = v_\infty q \tag{6.17}$$

can be applied to derive v_∞.

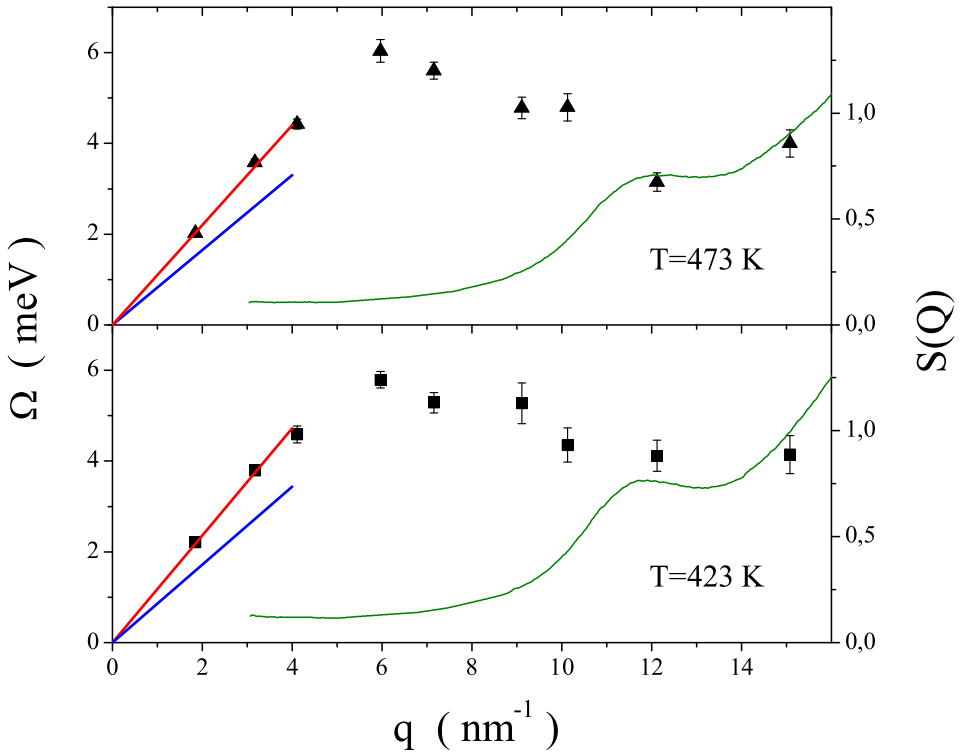

Figure 6.6: Dispersion curves of liquid sulfur at 423 K and 473 K. The energy position ω_∞(q) (symbols) has been plotted together with the static structure factor S(q) (green line). The red line are the best fit result in the region up to 4 nm^{-1} used for the evaluation of v_∞. The blue line corresponds to the hydrodynamic linear dispersion derived from the ultrasonic sound velocity.

The low q region can be linearly fitted to derive the high-frequency longitudinal sound velocity, v_∞. In figure 6.6 we report the line resulting from the fitting of the data in the q-region up to 4 nm^{-1}, v_∞ being the slope of this line [165]; we report also a line representing the hydrodynamic linear dispersion v_{us}q evaluated from ultrasonic measurements.

In figure 6.7 the temperature dependence of v_∞ obtained from our experimental data and the v_{us} values reported in the literature are compared.

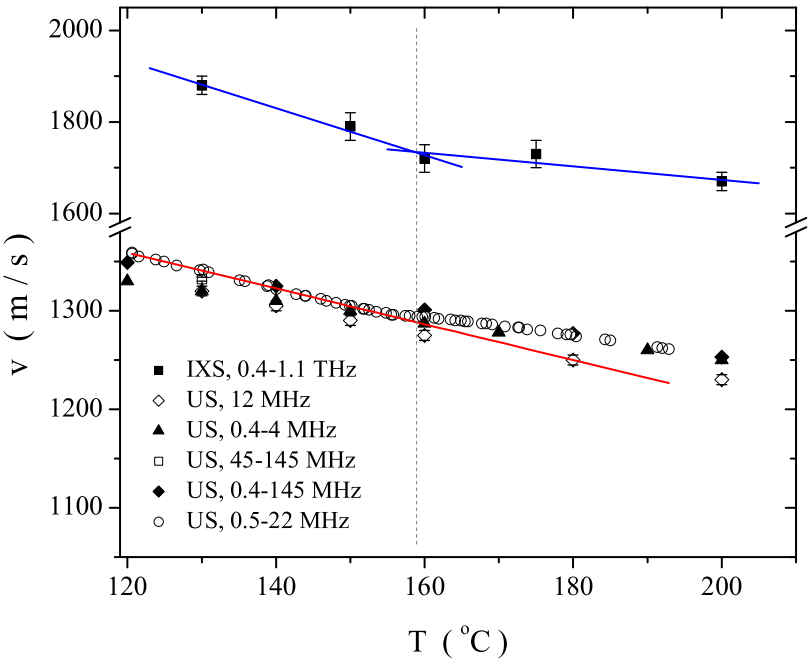

Figure 6.7: Sound velocity of liquid sulfur. The sound velocity derived from our IXS data has been plotted together with published ultrasonic data. The corresponding references are: 12 MHz - [167], 0.4-4 MHz - [168], 45-145 MHz - [169],0.4-145 MHz - [171], 0.5-22 MHz - [171]. The lines represents the best fit results for the T dependence of v_∞ before and after the λ-transition (blue lines) and of v_{us} in the domain of the molecular liquid (red line).

The sound velocities v_∞ obtained from the dispersion curves are about 36% higher than the ultrasonic sound velocity v_{us} reported in the literature at all the probed temperatures. This increase is commonly observed in liquid systems and suggests the presence of a structural relaxation at intermediate frequencies between the MHz and the THz frequency range. However this structural relaxation seems to be independent on the λ-transition, being the trends of v_∞(T) and v_{us}(T) parallel both below and above the polymerization temperature (figure 6.7).

Eq. 6.10 used by Kozhevnikov et al [170] to calculate the polymer extent Φ_p from the change of slope in the temperature dependence of the sound velocity, can be rewritten

as:

$$\Phi_p = \frac{(v_m + \Delta v)^2 - {v_m}^2}{{v_p}^2 - {v_m}^2} \tag{6.18}$$

where v_m and v_p are the sound velocity of the purely molecular and polymeric liquid, while $\Delta v = v - v_p$ represents the excess sound velocity with respect to the sound velocity of the pure polymeric liquid. Eq. 6.18 can be used to calculate the sound velocity of the polymeric component of the liquid above the λ-transition using literature data for Φ_p and using a linear extrapolation for the sound velocity v_m of the molecular liquid above the λ-transition (see fig.6.7). The v_p values calculated from eq. 6.18, using the Φ_p data reported by Koh *et al.* [153] (figure 5.22), are 20% larger than v_m in the limiting case.

In figure 6.8 we report the q dependence of the linewidth $2\Gamma_l$ (symbols) obtained from the best fit result at 423 K and 473 K. The static structure factor has been also reported (green line).

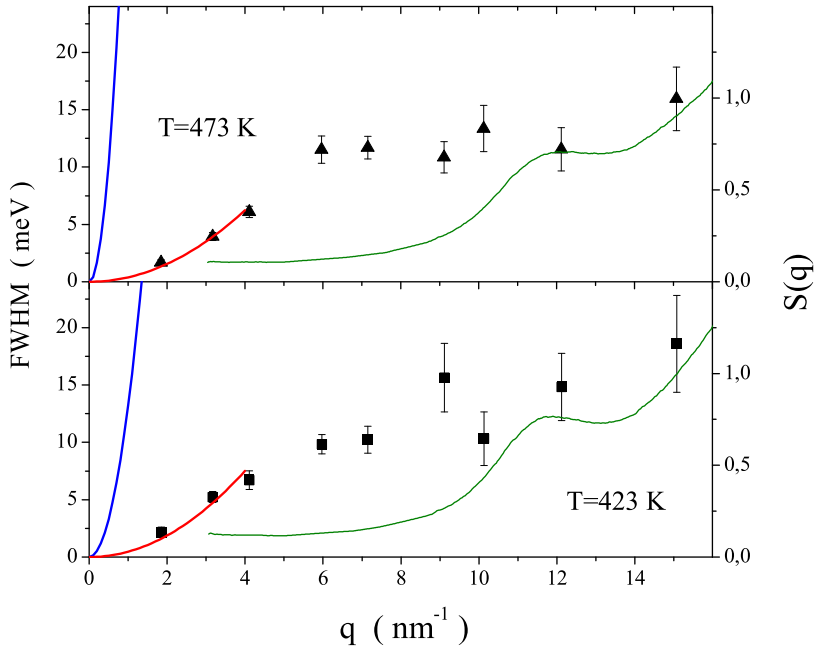

Figure 6.8: q dependence of 2Γ (FWHM) at 423 and 473 K. The red line represents the best fit obtained using a parabolic function; the blue line represents the hydrodynamic extrapolation.

The FWHM shows a q^2 dependence in the low q region up to $4nm^{-1}$. The red line in figure 6.8 represents the best fit result obtained using a quadratic ansatz. As for the positive linear dispersion of $\omega_\infty(q)$, this q^2 dependence of $2\Gamma_l$ is predicted by a sim-

ple hydrodynamics description, being $2\Gamma_l = \nu_l q^2$, where ν_l is the kinematic longitudinal viscosity. This prediction is also reported on fig.6.8 (blue line).

6.5.3 The non-ergodicity factor

The ratio of the elastic to the total spectral intensity f_q has been calculated and has been reported in figure 6.9, for what concerns the temperatures 423 K and 473 K. In the approximation that the constant pressure entropy fluctuations can be neglected, f_q can be considered a measurement of the non-ergodicity factor [166].

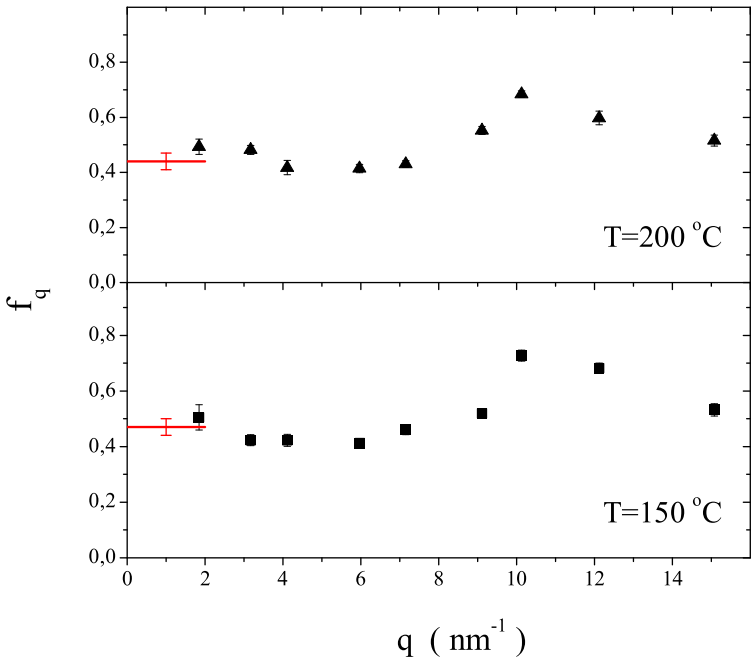

Figure 6.9: Non-ergodicity factor of liquid sulfur at 423 and 473 K. The f_q at q=0, as predicted for a viscoelastic liquid, has been indicated by the red segment.

The analysis of f_q at low q can be used to determine if liquid sulfur in the THz frequency range behaves as an elastic or viscoelastic liquid. Indeed, in the low q limit, when a liquid experiences a viscoelastic transition and thus changes its sound velocity from the adiabatic low frequency value v_o to the high frequency value v_∞, the non ergodicity factor is predicted to be:

$$f_q = 1 - \frac{{v_o}^2}{{v_\infty}^2} \tag{6.19}$$

Actually in figure 6.9 we have reported the guess value of f_q calculated using eq. 6.19 (assuming $v_{us} = v_o$) and the experimental v_∞, vs the fitting parameter f_q as obtained from the best fit results. Within the error bars, at low q our derived f_q is consistent with the calculated value. This consistency has been confirmed in the whole probed temperature range. The values derived from our IXS data at 2 nm^{-1} (black squares) and the ones calculated from eq. 6.19 using our v_∞ experimental data (red circles), are reported in figure 6.10 as a function of the temperature.

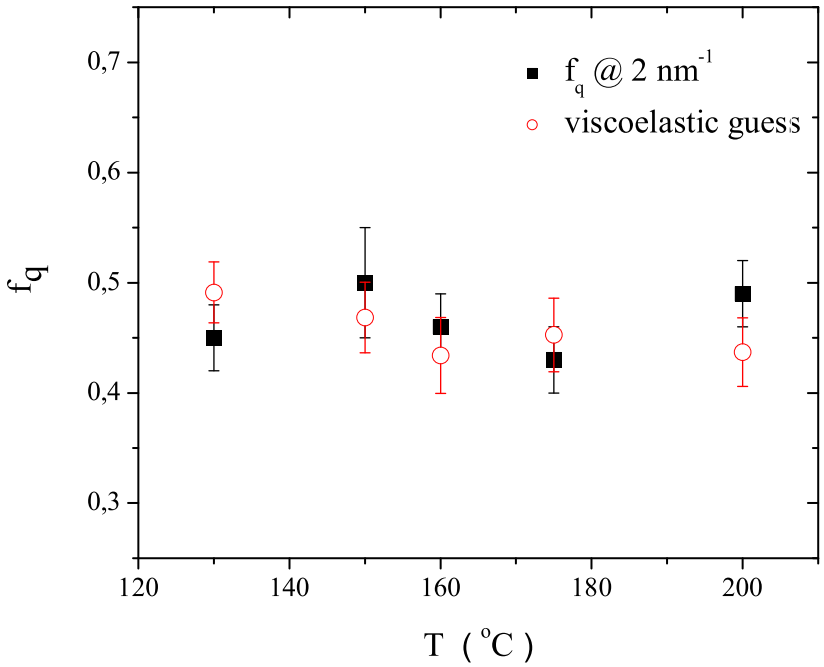

Figure 6.10: The non-ergodicity factor calculated for the data at q=2nm^{-1} and at all the probed temperatures (red circles) is compared to the corresponding viscoelastic guess.

The non-ergodicity factor measured at q = 2 nm^{-1} is in agreement with the viscoelastic prediction based on high and low frequency sound speed. From these data, we can conclude that liquid sulfur is characterized by a viscoelastic transition that takes place between the low frequency range probed in ultrasonic measurements (MHz) and the high frequency range probed by IXS (THz).

6.6 Dynamical properties of liquid sulfur

In the previous paragraph we have presented and discussed the q dependencies of the ω_∞, $2\Gamma_l$ parameters and the non-ergodicity factor f_q obtained from the best fit results based on a DHO model. From the dispersion curves, and the $2\Gamma_l$ and f_q vs q dependencies we have observed that the dynamical properties of liquid sulfur can be described within the framework of generalized hydrodynamics.

However, recent literature results on liquid sulfur have been interpreted differently [170, 171]. The principal problem is to explain the discrepancies between the low frequency sound absorption data and the hydrodynamics prediction.

In generalized hydrodynamics, $2\Gamma(\nu)/q^2$ is the frequency-dependent kinematic longitudinal viscosity. This quantity can be used for a direct comparison of our data, the low frequency literature data and the hydrodynamics prediction.

In our case, $2\Gamma(\nu)/q^2$ has been obtained directly using the fitting parameter Γ_l.

The corresponding, low frequency literature data are available as acoustical absorption $\alpha(\nu)$ data; in this case $2\Gamma(\nu)/q^2$ can be directly calculated from $\alpha(\nu)$, through the relation:

$$\frac{2\Gamma(\nu)}{q^2} = \frac{\alpha(\nu)v_o^3}{2\pi^2\nu^2} \tag{6.20}$$

Simple hydrodynamics can be applied to a liquid only in the hypothesis that the thermodynamic equilibrium has been reached. We suppose that this condition has been reached in the case of the molecular liquid at frequencies in the MHz range. In this case $2\Gamma(\nu)/q^2$ is equal to the kinematic longitudinal viscosity. Typically $\nu_l \propto \nu_s$, ν_l can then be calculated using the shear viscosity ν_s as an input and matching the literature acoustical data at temperatures below the λ-transition. In this way, we obtain a ratio ν_l/ν_s equal to 3.9±1.3. The result of this exercise is reported in figure 6.11 as a red line; in the same figure we report our $2\Gamma(\nu)/q^2$ data (black squares) and the $2\Gamma(\nu)/q^2$ values calculated from the acoustical absorption reported in previous ultrasonic studies [167–169, 171] using eq. 6.20 (open symbols).

All the reported ultrasonic data are frequency-independent at least in the 5.8-15 MHz range. Actually, observing the hydrodynamic prediction for the polymeric solution and the data obtained in the MHz range it is evident that the polymeric solution, in the MHz frequency range does not correspond to a hydrodynamic liquid in thermodynamic equilibrium. This feature, already pointed out by Pryor and Richardson [168] has been attributed by Kozhevnikov *et al.* [171] to the failure of the Navier-Stokes theory for polymers.

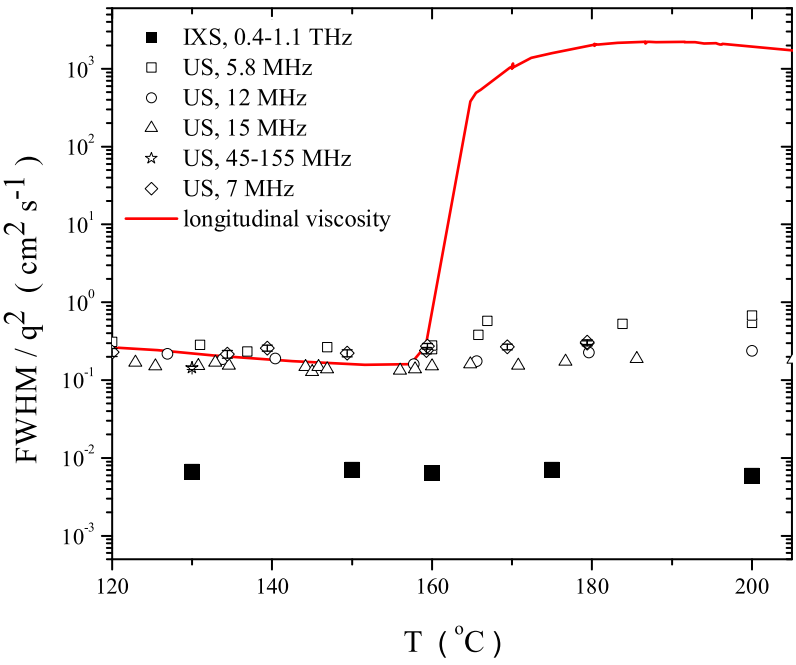

Figure 6.11: T dependence of $2\Gamma/q^2$. The black squares represents the IXS data, the open symbols are literature data. The acoustic data are from references [168–171]. The red line represents the hydrodynamic prediction.

In the light of all these results, our hypotheses is that the polymeric solution of sulfur above the λ-transition has not reached the thermodynamic equilibrium at MHz frequencies. This is because, most likely, the polymeric sulfur solution is characterized by an additional low frequency relaxation located at frequencies lower than the MHz probed by ultrasonic studies. The hydrodynamic predictions also confirm that liquid sulfur is viscoelastic, and that at the high frequencies probed by IXS we are exploring its elastic properties. In fact, if we use the ν_l/ν_s ratio derived before and literature data for the density, ρ [173], and the shear viscosity, $\eta_s = \rho\nu_s$ [22], in order to calculate the q-dependence of 2Γ by the simple hydrodynamic relation: $2\Gamma{=}\nu_l q^2$, the predicted slope is much higher than the observed one (figure 6.8).

In order to confirm the presence of a second relaxation process in the high temperature liquid, let us consider the Maxwell relation:

$$(v_\infty^2 - v_o^2)\tau = \nu_l \tag{6.21}$$

where τ is the structural relaxation time and v_o is the zero-frequency adiabatic sound velocity. This relation will allow us to test if the assumption v_{us}=v_o is valid or not, or, in other words if the relaxation mode that takes place between the ultrasonic and IXS frequencies is unique or not. Calculating τ for liquid sulfur below and above the λ-transition by using $\nu_l/\nu_s = 3.9$, our experimental data for v_∞, the literature data for the adiabatic sound velocity, the density and the shear viscosity [22, 173], we obtain the values 10 ps at 420 K and 10^5 ps at 450 K. This relaxation times corresponds to frequencies of 20 GHz at 420 K and 2 MHz at 450 K. Actually a relaxation process at 20 GHz is reasonable for the molecular liquid, for which we can then assume that $v_{us} = v_o$. A relaxation at 2 MHz for the polymeric liquid is instead in contradiction with the experimental observation. This result suggests that $v_{us} \neq v_o$ for the polymeric solution and than that an additional relaxation process takes place below the MHz frequency range.

If our hypotheses is correct: *where is the additional relaxation process of the polymeric solution located?*

An evaluation of the frequency at which this relaxation process takes place can be obtained by considering the behavior of a quenched polymeric solution of sulfur. The quenched product shows the typical behavior of a concentrated polymer solution: i) a glassy region where the shear modulus, G_N^o, is in the order of 10^9 Pa, ii) a glass-rubber transition that takes place at $T_g = 243$ K, iii) a rubbery plateau up to 260 K (where crystallization starts), characterized by a shear modulus, G_N^o, in the order of 10^5 Pa [174]. It is reasonable to suppose that this rubbery plateau is also present in the liquid above the λ-transition. In this case, two relaxation processes takes place in the polymeric solution: i) a high frequency one, located at frequencies between the MHz and the THz ranges, responsible in the polymeric liquid for the transition from v_{us} to v_∞; 2) a low frequency process, located at frequencies lower than the MHz and responsible for the transition v_o to v_{us}. The literature data on the bulk modulus, the viscosity [22,174] and the Maxwell relation (eq. 6.6) can give us information on the frequencies at which these relaxation takes place. Eq. 6.6 suggests that in the polymeric solution, the rubbery transition takes place below the kHz range, while the glassy transition is characterized by a relaxation time of 10 ps (around 20 GHz) like in the molecular liquid [175]. The locations of the relaxation processes for the molecular liquid and for the polymeric solution as obtained from the Maxwell relations (eq. 6.21 and eq. 6.6) are illustrated in figures 6.12 and 6.13 respectively.

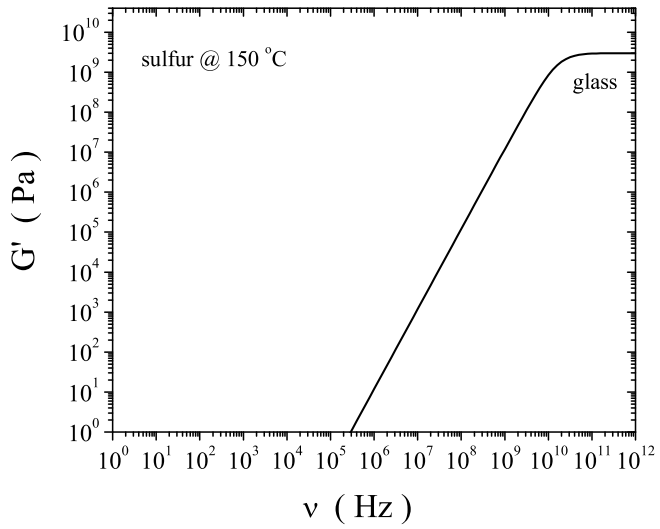

Figure 6.12: Frequency dependence of the shear modulus of molecular liquid sulfur. In correspondence to G_N^o=10^9 Pa we observe the glassy transition as a function of frequency.

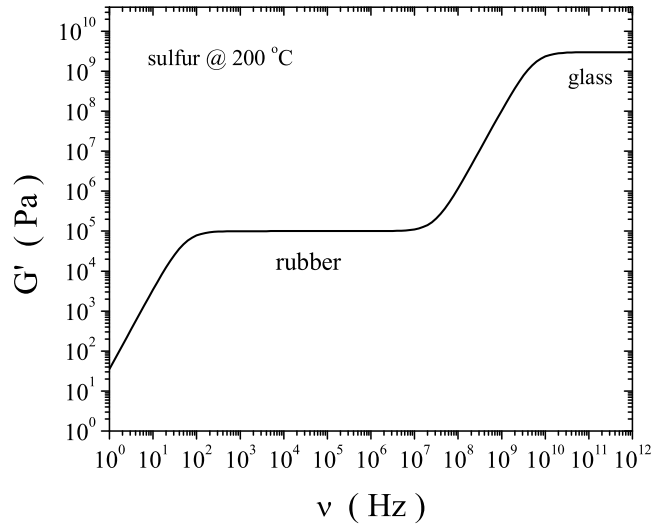

Figure 6.13: Frequency dependence of the shear modulus of the polymeric solution of sulfur. In correspondence to G_N^o=10^5 we observe the rubbery plateau due to the formation of an entangled network.

6.7 Viscoelasticity: Uncross-linked polymers

While different theories have been formulated on the viscoelastic behavior of polymer solutions, the existence of a rubbery plateau in the dynamics of liquid sulfur above the polymerization transition suggests the analogy with concentrated solutions of uncross-linked polymers of high molecular weight [176].

In a melt or a polymeric solution the viscosity increases modestly with the polymer molecular weight, M; roughly $\nu_s \propto M^1$. However there exists a critical value of M, above which the viscosity increases abruptly with $M^{3.4}$. This difference is due to the formation of entanglements between the polymeric chains, i.e. chains form temporary knots with each other hindering the normal chain motion. As a consequence of that, the viscosity of the fluid increases very rapidly.

From a dynamic point of view, polymers of high molecular weight are characterized by two sets of relaxation times with very different strengths. One of these relaxation times, the fast one, is commonly observed in polymers independently on the molecular weight; the slow one is instead characteristic only of polymers of high molecular weight and is accompanied by a plateau in the shear modulus. This plateau is normally called rubbery plateau. Again the rubbery plateau is related to the presence of an entanglements network in the liquid.

A model that well illustrates the nature of the motions in these polymeric systems has been formulated by Edwards *et al.* and successively treated by other authors (references in [176]). The basic idea of this model is to wrap the chains in a "tube" that represents the constraints from the other surrounding chains. The entanglement allows a "fast" dynamics only inside the tube, involving only movements of chain segments between two entanglement points. The "slow" dynamics in these systems corresponds to the time for the chain to completely slide out of its tube; in this time, the chain will lose completely the memory of its initial restraints.

The rubbery plateau can be used to determine the distance between entanglements, by using the relation:

$$G = \frac{\phi \rho RT}{M_e} \tag{6.22}$$

where ϕ is the polymer fraction, ρ is the polymer density, R is the gas constant and M_e is the molecular weight between entanglements. Using the polymer molecular weight, the number of atoms between two entanglements loci can easily be obtained.

M_e can be also used to define the critical weight above which we distinguish between the "low" and the "high" molecular weight of a polymer. The rubbery plateau is in fact

observed in polymers with a molecular weight higher than $2M_e$. This value defines the condition for a chain to form an entanglement.

Using the rubbery plateau, G_o^N, of quenched sulfur and eq. 6.22, we have evaluated $M_e \sim 2.4 \text{x} 10^3$ g/mol for the polymeric solution at 470 K. That means that there are ∼750 atoms between two entanglements sites. These values are commonly found in linear polymeric chains [176]. The average sulfur chain length has been calculated as a function of temperature by several authors [54]: already at beginning of the polymerization the theorical value is higher than this critical value, meaning that, above the λ-transition liquid sulfur presents entanglements between the chains.

Conclusions and future perspectives

Concluding remarks

Presented in this thesis is a detailed experimental study of the structural changes taking place in solid and liquid sulfur at high pressure and temperature and of the dynamical properties of the liquid around the λ-transition.

The main aims and objectives of this thesis project have been to study the solid sulfur polymorphism through the reconstruction of its phase diagram and the correlation of solid and liquid behavior. Our study has then been conducted with different experimental techniques, over a wide range of pressures and temperatures.

The experimental work has been logically organized in two research directions: one devoted to the solid and the other to the liquid study. The main results of this research work can be summarized in the following points:

- The *in situ* reconstruction of the phase diagram of sulfur up to 10 GPa and 1200 K, characterising:

  i) The structure and the stability domain of the rhombohedral S_6 phase;

  i) The stability domains of the orthorhombic and monoclinic molecular S_8 phases;

  ii) The stability domain of the trigonal polymeric phase;

  iii) The triple point between S_6, trigonal and the tetragonal phase;

  iv) The p,T trigonal-S_6 and tetragonal-S_6 transition lines;

  v) The melting curve to 5 GPa;

- The identification of the role of temperature in the polymerization of liquid sulfur through:

  i) The analysis of the evolution of the static structure factor;

  ii) The individuation of the dynamical processes taking place in liquid sulfur below and above the λ-transition;

- The clarification of the role of pressure in the polymerization of liquid sulfur.

The p,T study of sulfur stable phases has been performed by means of *in situ* measurements. The use of *in situ* techniques has facilitated the test of the stability of the different crystalline phases and has allowed us to individuate the quench recovery products in the old phase diagrams reported in literature. It is interesting to remark that, in the previous phase diagram of sulfur reported by Vezzoli *et al.* [177], twelve distinct phases had been proposed below 5 GPa, while in our mapping, in the same pressure range only three phases have been observed and characterized as stable crystalline phases of sulfur. This difference reflects the importance and the necessity of using *in situ* techniques for this kind of study.

A parallel use of diffraction and Raman spectroscopy has allowed us to confirm that the trigonal phase of sulfur observed by diffraction at high temperature corresponds to the polymeric, *p-S*, form of sulfur observed by Raman spectroscopy at room temperature. The existence of a relation between the Raman (room temperature) and the diffraction (high temperature) observations suggests the existence of a kinetic barrier associated to the $S_8 \rightarrow$ polymer transformation that, with different mechanisms, can be overcome by photo-induction or by heating. The role of the laser beam can be related to the opening of the S_8 molecule, thus emphasizing the necessity of a cis-trans conversion of the S_8 monomer fragment to proceed with the polymerization. The energy required for the ring opening depends on the applied pressure. In our diffraction data, the polymerization of sulfur is observed upon heating at 580 K independently of the applied pressure. The existence of a kinetic barrier and the role of the temperature to overcome it, is confirmed by the reversibility of the $S_8 \rightleftarrows$ trigonal transition at temperatures close to the melting. At lower temperatures the transition is reversible with some hysteresis, while at room temperature only a fraction of polymer is back-converted to S_8 molecules and the most part of the recovery product corresponds to fibrous sulfur.

The recent observation of the trigonal and tetragonal high pressure polymeric phases of sulfur, at high and room temperature, has promoted the idea that pressure induces polymerization of solid sulfur. The observation of the rhombohedral S_6 molecular phase at high pressure and high temperature, at pressures between these two polymeric forms, has revealed an alternating sequence of polymer-molecule transformation that refines this statement. The existence of rhombohedral S_6 at high pressure solves the most controversial question related to the differences between Raman and diffraction results. Rhombohedral S_6 represents also the first polymorph of sulfur that has been synthesized chemically at ambient pressure but that has its stability regime at high pressure and

temperature [144].

The structural sequence in the elements of a same group of the periodic table has been retrieved in the high pressure crystalline structures of sulfur and the allotropes of selenium. Indeed, S_8, S_6 molecules and polymeric structures with triangular and squared projection have been observed for both elements.

It is not necessary to draw solid transition lines in the liquid domain to conclude that a liquid is polymorphic in nature: the properties of the liquid change with pressure and temperature because of the changes of the local structures present in the liquid. The local structures in the liquid are related to the structures involved in solid-solid phase transitions. In order to test this liquid-solid correspondence in the case of sulfur, the liquid has been investigated as a function of pressure and temperature by means of diffraction, Raman spectroscopy and inelastic scattering at high frequencies.

As observed for the solid, the use of *in situ* diffraction has presented several advantages for the investigations of the liquid. The structural study of the liquid at temperatures above the λ-transition has put in evidence that the information on the structural changes that are taking place in the liquid are reflected in the first peaks of the structure factor. Through their analysis it has been possible to calculate the polymer fraction as a function of temperature in good agreement with previous literature data.

The role of the pressure in the equilibrium polymerization of sulfur has been investigated through the combination of X-ray diffraction and Raman spectroscopy. The combination of the results obtained using these two techniques has revealed to proved and to be a powerful method. Through the analysis of Raman spectra we have observed that the compression of liquid sulfur moves the $S_8 \rightleftarrows$ polymer equilibrium in the direction of polymerization; and with the comparison of the high pressure diffraction patterns of liquid sulfur with the one of selenium at atmospheric pressure we show that the systematic structural behavior in the elements of the same group of the periodic table can be retrieved in the liquid as in the solid state.

Inelastic X-ray scattering data have played an important role in the study of the dynamics of liquid sulfur around the λ-transition. These data analyzed in combination with the other acoustic data available from the literature, show that the λ-transition in sulfur can be seen as a transition between a simple liquid and a liquid which develops a rubber-like dynamics below the kHz frequency range. This dynamic behavior suggests the comparison of the polymeric solution of liquid sulfur to reference uncrosslinked solutions of high molecular weight polymers, highlighting the important role of entanglements between the polymeric chains. Another important point is that, only

measurements on the polymeric solution of sulfur performed at frequencies below the kHz frequency range can probe equilibrium properties. As a consequence, some relevant thermodynamic properties of the polymeric liquid are still unknown, and the ones reported in the literature, evaluated from low frequency data in the hypothesis of thermodynamic equilibrium, have to be revised. This is the case, for example, for the adiabatic sound velocity and the isothermal compressibility data [175].

Future perspectives

The study of the phase diagram of sulfur has offered the access to the stable crystalline phase of sulfur but has also evidenced the necessity to understand what is behind the high tendency to metastability in solid sulfur. In particular, with respect to that we remark the role of fibrous sulfur. It would be interesting to understand the mechanisms related to the formation of this sulfur form. This polymeric form can be obtained as recovery product by quenching the liquid or alternatively as a recovery of high pressure phases of sulfur (a fraction of S_8 could be present). In a such a way fibrous sulfur represents another link between solid and liquid sulfur.

The results obtained on liquid sulfur confirm the existence of a correlation between the solid and the liquid polymorphism. The polymerization process that interests the S_8 molecules is, in fact, at the basis of the solid and the liquid behavior. At the light of this correspondence, it would be interesting to test the effect of higher pressures on liquid sulfur. We reasonably suppose that the behavior of the liquid is similar to the behavior of the solid at high temperature: in this hypothesis, the alternating structure sequence between molecular and polymeric phases observed in the solid could be reflected in the pressure evolution of the local structures in the liquid. As a consequence, it would be interesting to explore the liquid region of the phase diagram above the S_6 rhombohedral phase. Indeed, despite there is no diffraction study in this liquid region reported in the literature, a transition associated to metallization at around 12 GPa and 1100 K has been observed by Brazhkin *et al.* [5] by means of resistivity measurements. We wonder whether if this transition is representative of the re-appearance of molecular sulfur liquid in the high pressure phase diagram.

The study of the sulfur dynamics has suggested that, above the λ-transition, liquid sulfur develops a rubber-like dynamics below the kHz frequency range. To definitively confirm this hypothesis, it would be interesting to measure the relaxation time of the rubbery transition.

Finally, more generally, it would be of great interest to study other simple systems such as H_2, O_2, Se, As in order to have a more general picture.

Bibliography

[1] Y. Katayama, T. Mizutani, W. Utsumi, o. Shimomura, M. Yamakata, and K. Funakoshi. A first-order liquid-liquid phase transition in phosphorus. *Nature*, 403:170–173, 2000.

[2] G. Monaco, S. Falconi, W. A. Crichton, and M. Mezouar. Nature of the first-order phase transition in fluid phosphorus at high temperature and pressure. *Physical Review Letters*, 90:255701, 2003.

[3] G. C. Vezzoli and L. W. Doremus. Variation in optical transmission and electrical resistance in a single sulfur liquid droplet during polymerization. *Applied Optics*, 16:433–435, 1977.

[4] G. C. Vezzoli, P. J. Kisatsky, L. W. Doremus, and P. J. Walsh. Optical and electrical effects during polymerization and depolymerization in liquid sulfur - indications for nonuniformity model for covalent liquids. *Applied Optics*, 15:327–339, 1976.

[5] V. V. Brazhkin, R. N. Voloshin, S. V. Popova, and A. G. Umnov. Nonmetal metal transition in sulfur melt under high-pressure. *Physics Letters A*, 154:413–415, 1991.

[6] Y. A. Chang, S. L. Chen, F. Zhang, X. Y. Yan, F. Y. Xie, R. Schmid-Fetzer, and W. A. Oates. Phase diagram calculation: past, present and future. *Progress In Materials Science*, 49:313–345, 2004.

[7] M. Emelianenko, Z. K. Liu, and Q. Du. A new algorithm for the automation of phase diagram calculation. *Computational Materials Science*, 35:61–74, 2006.

[8] S. A. Ostanin and V. Y. Trubitsin. Calculation of the phase diagram of Zr in a simple model. *Physica Status Solidi B-Basic Research*, 201:R9–R10, 1997.

[9] S. A. Ostanin and V. Y. Trubitsin. Calculation of the P-T phase diagram of hafnium. *Computational Materials Science*, 17:174–177, 2000.

[10] S. A. Ostanin and V. Yu Trubitsin. A simple model for caculating the P-T phase diagram of Ti. *Journal of Physiscs: Condensed Matter*, 9(36):L491–L496, 1997.

[11] J. C. Jamieson. Crystal structures at high pressures of metallic modifications of silicon and germanium. *Science*, 139:762, 1963.

[12] J. Z. Hu and I. L. Spain. Phases of silicon at high-pressure. *Solid State Communications*, 51:263–266, 1984.

[13] J. Z. Hu, L. D. Merkle, C. S. Menoni, and I. L. Spain. Crystal data for high-pressure phases of silicon. *Physical Review B*, 34:4679–4684, 1986.

[14] S. J. Duclos, Y. K. Vohra, and A. L. Ruoff. Experimental-study of the crystal stability and equation of state of Si to 248 GPa. *Physical Review B*, 41:12021–12028, 1990.

[15] S. J. Duclos, Y. K. Vohra, and A. L. Ruoff. Hcp-to-fcc transition in silicon at 78-GPa and studies to 100-GPa. *Physical Review Letters*, 58:775–777, 1987.

[16] M. Hanfland, U. Schwarz, K. Syassen, and K. Takemura. Crystal structure of the high-pressure phase silicon VI. *Physical Review Letters*, 82:1197–1200, 1999.

[17] P. F. McMillan. Condensed matter chemistry under 'extreme' high pressure-high temperature conditions. *High Pressure Research*, 24:67–86, 2004.

[18] N. Funamori and K. Tsuji. Structural transformation of liquid tellurium at high pressures and temperatures. *Physical Review B*, 65:014105, 2002.

[19] Y. Katayama and K. Tsuji. X-ray structural studies on elemental liquids under high pressures. *Journal of Physics: Condensed Matter*, 15:6085–6103, 2003.

[20] E. Rapoport. Model for melting-curve maxima at high pressure. *Journal of Chemical Physics*, 46:2891, 1967.

[21] R. Steudel. Liquid sulfur. *Topics In Current Chemistry*, 230:81–116, 2003.

[22] R. F. Bacon and R. Fanelli. The viscosity of sulfur. *Journal of the American Chemical Society*, 65:639–648, 1943.

[23] W. A. Crichton, G. B. M. Vaughan, and M. Mezouar. In situ structure solution of helical sulphur at 3 GPa and 400 degrees C. *Zeitschrift Fur Kristallographie*, 216:417–419, 2001.

[24] P. H. Poole, F. Sciortino, U. Essmann, and H. E. Stanley. Phase-behavior of metastable water. *Nature*, 360:324–328, 1992.

[25] W. A. Crichton, M. Mezouar, T. Grande, S. Stolen, and A. Grzechnik. Breakdown of intermediate-range order in liquid $GeSe_2$ at high pressure. *Nature*, 414:622–625, 2001.

[26] Y. Katayama, K. Tsuji, O. Shimomura, T. Kikegawa, M. Mezouar, D. Martinez-garcia, J. M. Besson, D. Hausermann, and M. Hanfland. Density measurements of liquid under high pressure and high temperature. *Journal of Synchrotron Radiation*, 5:1023–1025, 1998.

[27] J. H. Eggert, G. Weck, P. Loubeyre, and M. Mezouar. Quantitative structure factor and density measurements of high-pressure fluids in dacs by x-ray diffraction: Argon and water. *Physical Review B*, 65:174105, 2002.

[28] W. H. Bragg. On the structure of orthorhombic sulfur. *Proceedings Royal Society of London*, 89A:575, 1914.

[29] S. J. Rettig and J. Trotter. Refinement of the structure of orthorhombic sulfur, alpha-s_8. *Acta Crystallographica Section C-Crystal Structure Communications*, 43:2260–2262, 1987.

[30] I. E. Paukov, E. Y. Tonkov, and D. S. Mirinski. Phase diagram of sulphur at high pressure. *Doklady Akademii Nauk Sssr*, 164:588, 1965.

[31] C. Susse, R. Epain, and B. Vodar. *Compte Rendu Physique*, 258:45138, 1964.

[32] T. Baak. Sulfur - a new high pressure form. *Science*, 148:1220, 1965.

[33] B. C. Deaton and F. A. Blum. Properties of Group VI B Elements Under Pressure. I. Melting Curves of S, Se, and Te. *Physical Review*, 137:A1131–A1138, 1965.

[34] K. B. Ward and B. C. Deaton. Properties of Group VIB Elements Under Pressure. III Phase Diagram Studies of Various Forms of Sulfur. *Physical Review*, 153:947–951, 1967.

[35] G. C. Vezzoli, F. Dachille, and R. Roy. Melting curve of sulfur to 31 kbars. *Inorganic Chemistry*, 8:2658, 1969.

[36] S. Block and G. J. Piermarini. The melting curve of sulfur to 300°C and 12 kbar. *High Temperatures-High pressures*, 5:567, 1973.

[37] G. C. Vezzoli, F. Dachille, and R. Roy. Sulfur melting and polymorphism under pressure - outlines of fields for 12 crystalline phases. *Science*, 166:218, 1969.

[38] P. W. Bridgman. Polymorphism, Principally of the Elements, up to 50,000 kg/cm^2. *Physical Review*, 48:893–906, 1935.

[39] R. E. Harris, R. J. Vaisnys, H. Stromberg, and G. Jura. *Progress in Very High Pressure Research*. John Wiley & Sons, New York, 1961.

[40] S. Geller. Pressure-Induced Phases of Sulfur. *Science*, 152:644–646, 1966.

[41] S. R. Das. *Indian Journal of Physics*, 12:163, 1938.

[42] S. R. Das. *Indian Journal of Physics*, 13:91, 1939.

[43] C. B. Sclar, L. C. Carrison, W. B. Gager, and O. M. Stewart. Synthesis and stability of a high-pressure polymorph of sulfur. *Journal of Physics And Chemistry of Solids*, 27:1339, 1966.

[44] J. Donohue. *The Structure of the Elements*. Wiley Interscience, New York, 1974.

[45] H. Fujihisa, Y. Akahama, H. Kawamura, H. Yamawaki, M. Sakashita, T. Yamada, K. Honda, and T. Le Bihan. Spiral chain structure of high pressure selenium-II ' and sulfur-II from powder x-ray diffraction. *Physical Review B*, 70:134106, 2004.

[46] O. Degtyareva, E. Gregoryanz, M. Somayazulu, P. Dera, H. K. Mao, and R. J. Hemley. Novel chain structures in group VI elements. *Nature Materials*, 4:152–155, 2005.

[47] O. Degtyareva, E. Gregoryanz, H. K. Mao, and R. J. Hemley. Crystal structure of sulfur and selenium at pressures up to 160 GPa. *High Pressure Research*, 25:17–33, 2005.

[48] C. Hejny, L. F. Lundegaard, S. Falconi, M. I. McMahon, and M. Hanfland. Incommensurate sulfur above 100 GPa. *Physical Review B*, 71:020101, 2005.

[49] H. Luo, R. G. Greene, and A. L. Ruoff. Beta-po phase of sulfur at 162 GPa - x-ray-diffraction study to 212 GPa. *Physical Review Letters*, 71:2943–2946, 1993.

[50] Y. Akahama, M. Kobayashi, and H. Kawamura. Pressure-induced structural phase-transition in sulfur at 83-GPa. *Physical Review B*, 48:6862–6864, 1993.

[51] V. V. Struzhkin, R. J. Hemley, H. K. Mao, and Y. A. Timofeev. Superconductivity at 10-17 K in compressed sulphur. *Nature*, 390:382–384, 1997.

[52] H. Luo and A. L. Ruoff. X-ray diffraction study of sulfur to 32 GPa - amorphization at 25 GPa. *Physical Review B*, 48:569–572, 1993.

[53] R. Steudel and B. Eckert. Solid sulfur allotropes. *Topics In Current Chemistry*, 230:1–79, 2003.

[54] B. Meyer. *Elemental Sulfur: Chemistry and Physics*. Interscience, New York, 1965.

[55] L. K. Templeton, D. H. Templeton, and A. Zalkin. Crystal-structure of monoclinic sulfur. *Inorganic Chemistry*, 15:1999–2001, 1976.

[56] E. C. C. Engel. Sur deux nouveau etat du soufre. *Comptes Rendus de l'Academie des sciences*, 112:866.

[57] J. Donohue, E. Goldish, and A. Caron. Crystal and molecular structure of S_6. *Journal of The American Chemical Society*, 83:3748, 1961.

[58] J. Steidel, R. Steudel, and J. Pickardt. Sulfur compounds. 59. Redetermination of crystal and molecular structure of cyclohexasulfur, S_6. *Zeitschrift Fur Naturforschung Section B - Journal of Chemical Sciences*, 33:1554–1555, 1978.

[59] P. Cherin and P. Unger. Crystal structure of trigonal selenium. *Inorganic Chemistry*, 6:1589, 1967.

[60] M. D. Lind and S. Geller. Structure of pressure-induced fibrous sulfur. *Journal of Chemical Physics*, 51:348, 1969.

[61] M. L. Huggins. Comparison of the structures of stretched linear polymers. *Journal of Chemical Physics*, 13:37–42, 1945.

[62] J. A. Prins, J. Schenk, and P. A. M. Hospel. The x-ray diagram of fibrous sulfur. *Physica*, 22:770–772, 1956.

[63] J. A. Prins, J. Schenk, and L. H. J. Wachters. The structure of fibrous sulfur. *Physica*, 23:746–752, 1957.

[64] J. A. Prins and F. Tuinstra. Some new data on structure of fibrous sulfur. *Physica*, 29:328, 1963.

[65] J. A. Prins and F. Tuinstra. Note on structure of fibrous sulfur. *Physica*, 29:884, 1963.

[66] F. Tuinstra. Structure of fibrous sulphur. *Acta Crystallographica*, 20:341, 1966.

[67] S. Geller and M. D. Lind. Indexing of ψ-sulfur fiber pattern. *Acta Crystallographica Section B-structural Crystallography And Crystal Chemistry B*, 25:2166, 1969.

[68] J. Donohue and S. H. Goodman. On structure of fibrous sulfur. *Acta Crystallographica Section B-structural Crystallography And Crystal Chemistry B*, 25:2168, 1969.

[69] F. Feher, G. P. Gorler, and H. D. Lutz. Chemistry of sulfur. 108. Heats of Fusion and Specific Heat of liquid sulfur - influences of impurities. *Zeitschrift Fur Anorganische Und Allgemeine Chemie*, 382:135, 1971.

[70] E. H. Baker and T. G. Davey. Conductivity measurements on liquid sulfur. *Journal of Materials Science*, 13:1951–1956, 1978.

[71] C. W. Tompson and N. S. Gingrich. Atomic distributions in liquid, plastic, and crystalline sulfur. *Journal of Chemical Physics*, 31:1598–1604, 1959.

[72] K. S. Vahvaselka and J. M. Mangs. X-ray-diffraction study of liquid sulfur. *Physica Scripta*, 38:737–741, 1988.

[73] C. Biermann, R. Winter, C. Benmore, and P. A. Egelstaff. Structural and dynamic properties of liquid sulfur around the lambda-transition. *Journal of Non Crystalline Solids*, 234:309–313, 1998.

[74] R. Bellissent, L. Descotes, F. Boue, and P. Pfeuty. Liquid sulfur local order evidence of a polymerization transition. *Physical Review B*, 41:2135–2138, 1990.

[75] R. Bellissent, L. Descotes, and P. Pfeuty. Polymerization in liquid sulfur. *Journal of Physics - Condensed Matter*, 6:211–216, 1994.

[76] R. Winter, C. Szornel, W. C. Pilgrim, W. S. Howells, P. A. Egelstaff, and T. Bodensteiner. The structural properties of liquid sulfur. *Journal of Physics Condensed Matter*, 2:8427–8437, 1990.

[77] L. Descotes. *Etude par diffusion de neutrons de l'ordre local du soufre liquide autour de la transition de polymerisation.* Universite' Paris XI, Orsay, 1990.

[78] R. O. Jones and P. Ballone. Density functional and Monte Carlo studies of sulfur. I. Structure and bonding in S-n rings and chains (n=2-18). *Journal of Chemical Physics*, 121:7535–7535, 2004.

[79] L. Descotes and C. Bichara. The structure of liquid sulfur - a tight-binding Monte-Carlo simulation. *Journal of Non Crystalline Solids*, 193:627–631, 1995.

[80] F. H. Stillinger, T. A. Weber, and R. A. Laviolette. Chemical-reactions in liquids - molecular-dynamics simulation for sulfur. *Journal of Chemical Physics*, 85:6460–6469, 1986.

[81] M. Popescu. Atomic-scale structure of amorphous and liquid sulfur. *Journal of Non Crystalline Solids*, 97:187–190, 1987.

[82] B. Eckert, R. Schumacher, H. J. Jodl, and P. Foggi. Pressure and photoinduced phase transitions in sulphur investigated by Raman spectroscopy. *High Pressure Research*, 17:113–146, 2000.

[83] A. G. Kalampounias, K. S. Andrikopoulos, and S. N. Yannopoulos. Probing the sulfur polymerization transition *in situ* with Raman spectroscopy. *Journal of Chemical Physics*, 118:8460–8467, 2003.

[84] A. G. Kalampounias, D. T. Kastrissios, and S. N. Yannopoulos. Structure and vibrational modes of sulfur around the lambda-transition and the glass transition. *Journal of Non Crystalline Solids*, 326:115–119, 2003.

[85] R. Steudel. Sulfur-Compounds .84. The effect of S-6 and S-7 on the Polymerization of Liquid Sulfur. *Phosphorus Sulfur And Silicon And The Related Elements*, 16:251–255, 1983.

[86] Y. B. Wang, T. Uchida, F. Westferro, M. L. Rivers, N. Nishiyama, J. Gebhardt, C. E. Lesher, and S. R. Sutton. High-pressure x-ray tomography microscope: Synchrotron computed microtomography at high pressure and temperature. *Review of Scientific Instruments*, 76:073709, 2005.

[87] *http://www.hppi.troitsk.ru/products/Toroid2/Toroid1.htm.*

[88] J. M. Besson, R. J. Nelmes, G. Hamel, J. S. Loveday, G. Weill, and S. Hull. Neutron powder diffraction above 10-GPa. *Physica B*, 180:907–910, 1992.

[89] C. E. Weir, E. R. Lippincott, A. Van Valkenburg, and E. N. Bunting. Infrared Studies in the 1- to 15-Micron Region to 30,000 Atmospheres. *Journal of Research of the National Bureau of Standards*, 63:55–62, 1958.

[90] *http://www.ph.ed.ac.uk.*

[91] *http://www-pat.llnl.gov/Research/hipressphys.*

[92] J. P. Pinceaux R. Letoullec and P. Loubeyre. The membrane dac: a new device for generating continuous pressure and temperature variation. *High Pressure Research*, 1:77–90, 1988.

[93] M. J. Moore, D. B. Sorensen, and R. C. Devries. A simple heating device for diamond anvil high pressure cells. *Review of Scientific Instruments*, 41:1665, 1970.

[94] R. A. Forman, S. Block, J. D. Barnett, and G. J. Piermarini. Pressure measurement made by utilization of ruby sharp-line luminescence. *Science*, 176:284, 1972.

[95] G. J. Piermarini, S. Block, J. D. Barnett, and R. A. Forman. Calibration of pressure-dependence of R1 ruby fluorescence line to 195 kbar. *Journal of Applied Physics*, 46:2774–2780, 1975.

[96] O. Grasset. Calibration of the R ruby fluorescence lines in the pressure range [0-1 GPa] and the temperature range [250-300K]. *High Pressure Research*, 21:139–157, 2001.

[97] S. Rekhi, L. S. Dubrovinsky, and S. K. Saxena. Temperature-induced ruby fluorescence shifts up to a pressure of 15 GPa in an externally heated dac. *High Temperatures-High Pressures*, 31:299–305, 1999.

[98] D. D. Ragan, R. Gustavsen, and D. Schiferl. Calibration of the ruby R(1) and R(2) fluorescence shifts as a function of temperature from 0 to 600-K. *Journal of Applied Physics*, 72:5539–5544, 1992.

[99] H. K. Mao, P. M. Bell, J. W. Shaner, and D. J. Steinberg. Specific volume measurements of Cu, Mo, Pd, and Ag and calibration of ruby R1 fluorescence pressure gauge from 0.06 to 1 Mbar. *Journal of Applied Physics*, 49:3276–3283, 1978.

[100] J. D. Barnett, S. Block, and G. J. Piermarini. Optical fluorescence system for quantitative pressure measurement in diamond-anvil cell. *Review of Scientific Instruments*, 44:1–9, 1973.

[101] J. M. Besson and R. J. Nelmes. New developments in neutron-scattering methods under high-pressure with the Paris-Edinburgh cells. *Physica B*, 213:31–36, 1995.

[102] M. Mezouar, T. Le Bihan, H. Libotte, Y. Le Godec, and D. Hausermann. Paris-Edinburgh large-volume cell coupled with a fast imaging-plate system for structural investigation at high pressure and high temperature. *Journal of Synchrotron Radiation*, 6:1115–1119, 1999.

[103] M. B. Myers, F. Dachille, and R. Roy. Pressure multiplication effect in opposed-anvil configurations. *Review of Scientific Instruments*, 34:401, 1963.

[104] W. A. Crichton and M. Mezouar. Noninvasive pressure and temperature estimation in large-volume apparatus by equation-of-state cross-calibration. *High Temperatures-High Pressures*, 34:235–242, 2002.

[105] D. L. Decker. High-pressure equation of state for NaCl, KCl, and CsCl. *Journal of Applied Physics*, 42:3239, 1971.

[106] F. Birch. Equation of state and thermodynamic parameters of NaCl to 300-kbar in the high-temperature domain. *Journal of Geophysical Research-Solid Earth And Planets*, 91:4949–4954, 1986.

[107] D. L. Heinz and R. Jeanloz. The equation of state of the gold calibration standard. *Journal of Applied Physics*, 55:885–893, 1984.

[108] Y. Le Godec, D. Martinez-garcia, M. Mezouar, G. Syfosse, J. P. Itie, and J. M. Besson. Thermoelastic behaviour of hexagonal graphite-like boron nitride. *High Pressure Research*, 17:35–46, 2000.

[109] M. Altarelli and A. Salam. The quest for brilliance: light sources from the third to the fourth generation. *Europhysics News*, 35:2, 2004.

[110] *http://www.esrf.fr*.

[111] B. D. Cullity. *Elements of X-ray diffraction.* Addison-wesley editions, 1978.

[112] M. Mezouar, W. A. Crichton, S. Bauchau, F. Thurel, H. Witsch, F. Torrecillas, G. Blattmann, P. Marion, Y. Dabin, J. Chavanne, O. Hignette, C. Morawe, and C. Borel. Development of a new state-of-the-art beamline optimized for monochromatic single-crystal and powder X-ray diffraction under extreme conditions at the esrf. *Journal Of Synchrotron Radiation*, 12:659–664, 2005.

[113] L. Zhang, W. K. Lee, M. Wulff, and L. Eybert. The performance of a cryogenically cooled monochromator for an in-vacuum undulator beamline. *Journal of Synchrotron Radiation*, 10:313, 2003.

[114] O. Hignette, P. Cloetens, W. K. Lee, W. Ludwig, and G. Rostaing. Hard X-ray microscopy with reflecting mirrors status and perspectives of the ESRF technology. *Journal De Physique Iv*, 104:231–234, 2003.

[115] E. Burkel. *Inelastic Scattering of X-Rays with Very High Energy Resolution.* Springer-Verlag, 1991.

[116] L. Van Hove. Correlations in Space and Time and Born Approximation Scattering in Systems of Interacting Particles. *Physical Review*, 95:249–262, 1954.

[117] H. Zachariasen. *Theory of X-Ray Diffraction in Crystals.* Dover, New York, 1944.

[118] H. Ibach. Thermal expansion of silicon and zinc oxide (I). *Physica Status Solidi*, 31:625, 1969.

[119] R. Verbeni, F. Sette, M. H. Krisch, U. Bergmann, B. Gorges, C. Halcoussis, K. Martel, C. Masciovecchio, J. F. Ribois, and G. Ruocco. X-ray monochromator with $2x10^{-8}$ energy resolution. *Journal Of Synchrotron Radiation*, 3:62–64, 1996.

[120] C. Masciovecchio, U. Bergmann, M. Krisch, , G. Ruocco, F. Sette, and R. Verbeni. A perfect crystal X-ray analyser with 1.5 meV energy resolution. *Nuclear Instruments and Methods in Physics Research Sec.B-Beam Interactions with Materials and Atoms*, 117:339–340, 1996.

[121] C. Masciovecchio, U. Bergmann, M. Krisch, G. Ruocco, F. Sette, and R. Verbeni. A perfect crystal X-ray analyser with meV energy. *Nuclear Instruments and Methods in Physics Research Sec.B-Beam Interactions with Materials and Atoms*, 111:181–186, 1996.

[122] J.J. Laserna. *Modern techniques in Raman Spectroscopy.* John Wiley & Sons, New York, 1944.

[123] L. Pauling. On the stability of the S_8 molecule and the structure of fibrous sulfur. *Proceedings of The National Academy of Sciences of The United States of America*, 35:495–499, 1949.

[124] A. Yoshioka and K. Nagata. Raman spectrum of sulfur under high pressure. *Journal of Physics And Chemistry of Solids*, 56:581–584, 1995.

[125] W. Hafner, J. Kritzenberger, H. Olijnyk, and A. Wokaun. Phase transitions in crystalline sulfur at P> 8GPa, observed by raman spectroscopy in a dac.

[126] B. Eckert and R. Steudel. Molecular spectra of sulfur molecules and solid sulfur allotropes. *Topics In Current Chemistry*, 231:31–98, 2003.

[127] B. Lorenz and I. Orgzall. Optical absorption studies of sulfur at pressures up to 20 GPa. *AIP Conference Proceedings*, 309:259–262, 1994.

[128] I. Orgzall and B. Lorenz. On the formation of photo-induced high pressure phases in sulfur below 10 GPa. *High Pressure Research*, 13:215–224, 1995.

[129] P. Wolf, B. J. Baer, M. Nicol, and H. Cynn. *Molecular systems under High Pressure, 263.* R. Pucci and G. Picciotto, Elsevier, Amsterdam, 1991.

[130] K. Nagata, T. Nishio, H. Taguchi, and Y. Miyamoto. Raman spectroscopic and X-ray diffraction study of sulfur under high pressure. *Japanese Journal of applied physics*, 31:1078–1084, 1992.

[131] B. Eckert, H. J. Jodl, H. O. Albert, and P. Foggi. *Frontiers of High Pressure Research, 143.* H. D. Hochheimer and R. D. Etters editions, 1991.

[132] P. Rossmanith, W. Hafner, A. Wokaun, and H. Olijnyk. Phase transitions of sulfur at high pressure: influence of temperature and pressure environment. *High Pressure Research*, 11:183–194, 1993.

[133] N. L. Ross. Fourier transform Raman spectroscopy at high pressures - preliminary results of sulfur to 56 kbar. *Spectrochimica Acta Part A-Molecular And Biomolecular Spectroscopy*, 49:681–684, 1993.

[134] M. J. Peanasky, C. W. Jurgensen, and H. G. Drickamer. The effect of pressure on the optical absorption edge of sulfur to 300 kbar. *Journal of Chemical Physics*, 81:6407–6408, 1984.

[135] K. Kusaba and T. Kikegawa. *Photon Factory Activity Report*, 18B, 2000.

[136] N. Sakurai, H. Hirano, A. Onodera, Y. Akahama, and H. Kawamura. *Spring-8 User Experiment Report*, 55:–, 1998.

[137] Y. Sakaguchi and K. Tamura. Photoinduced polymerization and relaxation in liquid sulfur. *Journal of Physics Condensed Matter*, 7:4787–4801, 1995.

[138] V.M. Goldschmidt. *Atlas Der Krystallformen.* Heidelberg, Winter, 1913.

[139] E. Y. Tonkov. High pressure phase transformations. *Gordon and Breach, Philadelphia*, 2:647–649, 1992.

[140] E. Y. Tonkov. High pressure phase transformations. *Gordon and Breach, Philadelphia*, 3:166–167, 1996.

[141] B. Meyer. Solid allotropes of sulfur. *Chemical Reviews*, 64:429, 1964.

[142] R. Zallen. Pressure Raman effects and vibrational scaling laws in molecular crystals - S_8 and As_2S_3. *Physical Review B*, 9:4485–4496, 1974.

[143] L. Wang. *High pressure research in Mineral Physics, 299-304.* Manghnani, 1987.

[144] L. Crapanzano, W. A. Crichton, G. Monaco, R. Bellissent, and M. Mezouar. Alternating sequence of ring and chain structures in sulphur at high pressure and temperature. *Nature Materials*, 4:550–552, 2005.

[145] R. Steudel, Y. Steudel, and M. W. Wong. Speciation and thermodynamics of sulfur vapor. *Topics In Current Chemistry*, 230:117–134, 2003.

[146] M. W. Wong, Y. Steudel, and R. Steudel. Novel isomers of hexasulfur: Prediction of a stable prism isomer and implications for the thermal reactivity of elemental sulfur. *Journal of Chemical Physics*, 121:5899–5907, 2004.

[147] K. Raghavachari, C. M. Rohlfing, and J. S. Binkley. Structures and stabilities of sulfur clusters. *Journal of Chemical Physics*, 93:5862–5874, 1990.

[148] R. Winter, P. A. Egelstaff, W. C. Pilgrim, and W. S. Howells. The structural-properties of liquid, solid and amorphous sulfur. *Journal of Physics: Condensed Matter*, 2:SA215–SA218, 1990.

[149] A. T. Ward and M. B. Myers. An investigation of polymerization of liquid sulfur, sulfur-selenium and sulfur-arsenic mixtures using Raman spectroscopy and scanning differential calorimetry. *Journal of Physical Chemistry*, 73:1374, 1969.

[150] K. Hattori and H. Kawamura. Raman study of liquid sulfur. *Journal of Non Crystalline Solids*, 59(6):1063–1066, 1983.

[151] V. V. Brazhkin, S. V. Popova, and R. N. Voloshin. Pressure-temperature phase diagram of molten elements: selenium, sulfur and iodine. *Physica B: Condensed Matter*, 265:64–71, 1999.

[152] F. J. Touro and T. K. Wiewioro. Viscosity chain length relationship in molten sulfur systems. *Journal of Physical Chemistry*, 70:239, 1966.

[153] J. C. Koh and W. Klement. Polymer content of sulfur quenched rapidly from melt. *Journal of Physical Chemistry*, 74:4280, 1970.

[154] G. C. Vezzoli. Electrical resistance of liquid sulfur to 420 degrees C and of liquid selenium to 700 degrees C. *Journal of The American Chemical Society*, 55:65, 1972.

[155] *Private communications with G. C. Vezzoli.*

[156] B. Meyer, T. V. Oommen, and D. Jensen. Color of liquid sulfur. *Journal of Physical Chemistry*, 75:912, 1971.

[157] B. Meyer, T. Stroyerh, D. Jensen, and T. V. Oommen. Color of liquid sulfur. *Journal of The American Chemical Society*, 93:1034, 1971.

[158] Y. Katayama and K. Tsuji. X-ray structural studies on elemental liquids under high pressures. *Journal of Physics Condensed Matter*, 15:6085–6103, 2003.

[159] Y. Waseda. *The Structure of Non Crystalline Materials.* McGraw-Hill, New York, 1980.

[160] R. Bellissent and G. Tourand. Short-range order in amorphous and liquid se1-xtex systems. *Journal Of Non-crystalline Solids 35-6*, 35-6:1221–1226, 1980.

[161] A. V. Tobolsky and A. Eisenberg. Equilibrium polymerization of sulfur. *Journal Of The American Chemical Society*, 81:780–782, 1959.

[162] S. Greer. Physical Chemistry of Equilibrium Polymerization. *Journal Of Physical Chemistry B*, 102:5413–5422, 1988.

[163] J. C. Wheeler, S. J. Kennedy, and P. Pfeuty. Equilibrium polymerization as a critical phenomenon. *Physical Review Letters*, 45:1748–1754, 1980.

[164] E. D. West. The Heat Capacity of sulfur from 25-degrees to 450-degrees, the Heats and Temperatures of Transition and Fusion. *Journal Of The American Chemical Society*, 81:29, 1959.

[165] J.P. Boon and S. Yip. *Molecular Hydrodynamics*. Dover Publications Inc., New York, 1980.

[166] G. Monaco, A. Cunsolo, G. Ruocco, and F. Sette. Viscoelastic behavior of water in the terahertz frequency range: An inelastic x-ray scattering study. *Physical Review E*, 60:5505–5520, 1999.

[167] O. J. Kleppa. Ultrasonic velocity of sound at 12-mc in liquid sulfur. *Journal Of Chemical Physics*, 18:1303–1303, 1950.

[168] A. W. Pryor and E. G. Richardson. Velocity and absorption of ultrasonics in liquid sulfur. *Journal Of Physical Chemistry*, 59:14–16, 1955.

[169] J. L. Hunter and T. L. Francavilla. *Journal Of American Acoustical Society*, 35:1834, 1963.

[170] V. F. Kozhevnikov, J. M. Viner, and P. C. Taylor. Power law in properties of sulfur near the polymerization transition. *Physical Review B*, 64:214109, 2001.

[171] V. F. Kozhevnikov, W. B. Payne, J. K. Olson, C. L. McDonald, and C. E. Inglefield. Physical properties of sulfur near the polymerization transition. *Journal Of Chemical Physics*, 121:7379–7386, 2004.

[172] W. Gotze in. *Liquids, Freezing and Glass Transition, 289-503*. J. P. Hansen, D. Levesque and J. Zinn-Justin, Amsterdam, 1991.

[173] V. F. Zheen and S. Greer. The density of liquid sulfur. *Journal Of Chemical Physics*, 96:2175, 1992.

[174] A. V. Tobolsky, W. MacKnight, R.B. Beevers, and V. D. Gupta. The glass transition temperature of polymeric sulphur. *Polymer*, 4:423, 1963.

[175] G. Monaco, L. Crapanzano, R. Bellissent, and et al. Rubberlike dynamics in sulphur above the lambda-transition temperature. *Physical Review Letters*, 95:255502, 2005.

[176] J. D. Ferry. *Viscoelastic properties of polymers*. John Wiley & Sons, New York, 1980.

[177] G. C. Vezzoli, F. Dachille, and R. Roy. Sulfur melting and polymorphism under pressure - outlines of fields for 12 crystalline phases. *Science*, 166:218, 1969.